2 Design and Pre-Flight Calibration

2.1 Overview

2.1.1 INTRODUCTION

The essential approach of the MSSTA in all its incarnations has been to obtain simultaneous images of the solar disk in as many different UV bandpasses as possible, sometimes at the expense of producing a single image with extremely high spatial resolution, signal-to-noise, or accurate calibration. The current generation of EUV observatories, including EIT and TRACE, have improved on the MSSTA's performance in a number of areas: they deliver high-resolution, high-cadence images, and have enabled exciting studies of coronal dynamics and energy flows [e.g. (De Pontieu, Berger et al. 1999), (Schrijver, Aschwanden et al. 2002)]. But they are limited to three or fewer coronal bandpasses, and (in the case of TRACE) cannot take simultaneous images at different wavelengths or see the full disk at once. The truly multi-spectral philosophy of the MSSTA means that it is uniquely capable of diagnosing the state of the corona over a broad temperature range and at numerous locations on the disk at one instant of time.

As discussed in the previous chapter, taking advantage of this capability to generate spatially-resolved coronal DEMs imposes two requirements:

- Bandpass selection: the payload must produce images in enough different EUV bandpasses to constrain the DEM over a broad temperature range. Ideally, the bandpasses should produce temperature kernels that are narrow and well-spaced in temperature; however, double-peaked or redundant temperature kernels provide useful consistency checks and are helpful in dealing with noise.

- Calibration: The instruments must be accurately calibrated, as the inversion problem is extremely sensitive to error.

These considerations were central to the planning of the MSSTA III.

In this chapter, I will discuss the design of the payload, focusing on the selection of telescope bandpasses for optimal coverage of coronal temperatures. I will then give a detailed step-by-step account of the calibration of the MSSTA telescope mirrors, filters and film. Understanding the calibration, and knowing to what extent and in what ways its accuracy may be limited, is essential to interpreting MSSTA data. Finally, I will present the temperature kernels of the MSSTA telescopes, along with an assessment of the uncertainty associated with each.

2.1.2   DESIGN OF THE MSSTA III

The MSSTA payload is, by design, modular and reconfigurable. The truss is essentially an open support structure with enough mounting surfaces to attach 20 or more instruments. Indeed, the MSSTA II attempted to make full use of the truss's flexibility by incorporating 19 different telescopes (Figure 4). Unfortunately, only 5 of these telescopes produced high-quality images. A discussion of the failure of the other instruments can be found in (Martínez-Galarce), but the complexity of the payload clearly made it difficult to ensure that each instrument would function properly. In particular, the small Herschelian telescopes (those with apertures of 25-30 mm) generally shared cameras and filters with each other, greatly increasing the difficulty of payload integration while offering limited scientific return. Early in the design of the MSSTA III, we decided to limit the instrument suite to 11 telescopes, all with apertures of 60 mm or larger.[1]

Originally, two of these telescopes were to feed grating spectrographs to probe the 170-180 Å region and the 2800 Å Mg II complex with high spectral resolution. The EUV spectrograph design used a Herschelian primary and a multilayer-coated grating in a Wadsworth configuration, and would have been the first instrument of its kind used for solar research (Boerner, Walker et

---

[1] A single small Herschelian from the MSSTA II payload, centered at 94 Å, was added to the MSSTA III during final integration; this is briefly discussed in section 3.1.1.

al. 1999). However, time pressure and manpower shortages led us to scrap both spectrographs, and to replace them with more straightforward imaging telescopes. This was a disappointing compromise; imaging spectroscopy of the solar atmosphere is badly needed, and the MSSTA has potential as a platform for testing such instruments. Nevertheless, the decision to fly 11 telescopes of moderate aperture, and to avoid the inclusion of smaller telescopes or more complicated spectrographs, resulted in a payload that was well-focused on addressing the questions raised in Chapter 1.
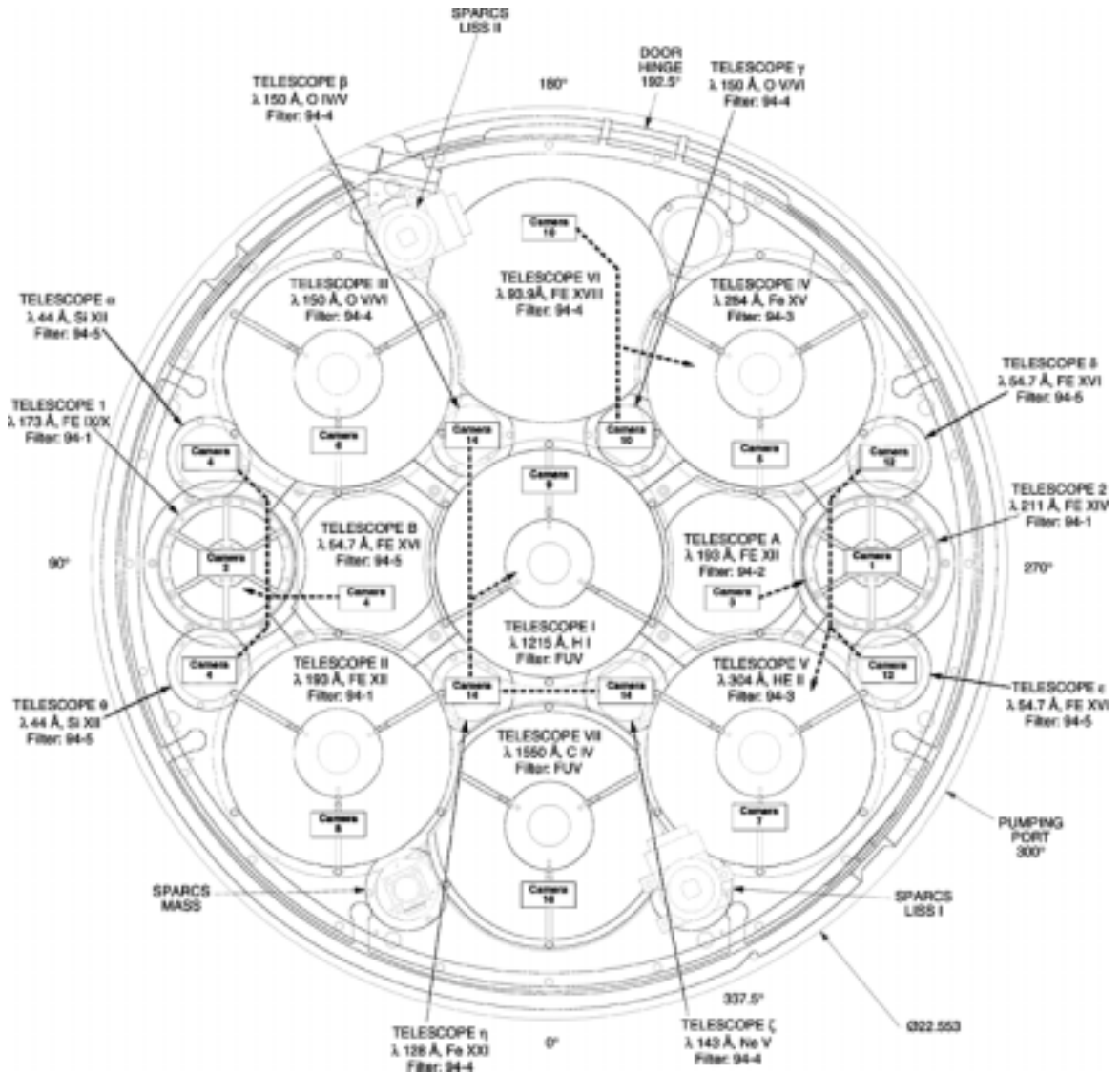
Figure 4. Front aperture view of the MSSTA II, showing the placement of the 19 telescopes it pointed at the sun during its flight in 1994. For the MSSTA III, all of the small (aperture < 60mm) telescopes were abandoned in order to focus on the 11 large telescopes. Drawing taken from (Hoover, Walker et al. 1992).

31

Bandpass Selection

The only remaining question was what bandpasses should be used for the 11 telescopes. Two slots were reserved for the 127 mm-aperture FUV telescopes that had flown on both previous MSSTA missions (centered at 1216 Å H Ly α and 1550 Å C IV). These instruments had delivered excellent data on both flights. The 1216 Å image had proven particularly valuable in the analysis of x-ray bright points identified from the MSSTA I data [(Kankelborg, Walker et al. 1996), (Kankelborg, Walker et al. 1997)], and there is no other source of well-filtered Lyman α spectroheliographs. Of course, the FUV telescopes pose a number of challenges; they are not directly useful in DEM analysis, as the solar FUV radiation violates many of the underlying assumptions developed in Chapter 1; and they require entirely separate calibration and alignment techniques from the EUV telescopes, as described later in section 2.6. In fact, neither FUV instrument was fully calibrated; nevertheless, they were seen as indispensable to the mission.

While FUV optics are robust, so that the age of the 1550 Å and 1216 Å telescopes was not a source of concern, advances in multilayer technology and the frailty of thin-film filters made it inadvisable to re-fly any of the EUV telescopes from previous MSSTA missions. Thus we had to choose 9 EUV bandpasses, and design multilayer telescopes for each, in order to maximize our ability to diagnose the state of the coronal plasma.

A similar exercise was carried out for the design of the MSSTA II (Plummer, DeForest et al. 1994), relying heavily on the investigators' experience and knowledge of the solar EUV spectrum. While we had less experience to call on in choosing instruments for the MSSTA III, we did have access to the CHIANTI database, which can be used to generate temperature kernels from an assumed instrument bandpass given any of a variety of assumptions. A suite of IDL procedures was written to implement a "brute force" approach to bandpass selection. First, a set of idealized bandpass candidates was generated. These took the form of Gaussians centered at all wavelengths from 50 – 300 Å, in 1 Å steps. The amplitude (peak reflectivity) of the Gaussian and FWHM were made to be functions of wavelength, based on a few rules of thumb about multilayer performance:

- Multilayer reflectivity peaks at around 60% for 131 Å (an important wavelength in EUV lithography), declining sharply on the high-energy side. We modeled this by setting peak

reflectivity for a bandpass centered at λ to $R_{max}(\lambda) = 0.6 \times (131 \text{ Å} / \lambda)^k$, where $k = 1$ for $\lambda \geq$ 131 Å and $k = -2$ for $\lambda < 131$ Å.

- The FWHM of a multilayer bandpass is ~7 Å at 171 Å; it gets much narrower at short wavelengths, as the energetic photons penetrate deep into the multilayer stack. We modeled this by setting the bandpass FWHM = $\lambda/25$.

These assumptions gave reasonable approximations to the expected parameters of the multilayers.

Then, a temperature kernel for each of the bandpass candidates was generated, and the set of temperature kernel candidates was examined. We looked for kernels that featured strong, narrow peaks in temperature (indicating telescopes that produced unambiguous, almost isothermal images); we also required that the instrument's response at its peak be strong enough to ensure a usable image from at least a solar active region. While there was no shortage of candidate lines offering strong peaks in the $\text{Log}(T) = 6.0 - 6.2$ range, we struggled to find wavelengths that could probe the UTR at temperatures from $5.5 - 6.0$ without contamination (and with sufficient sensitivity to guarantee results, given that the UTR emission is not as strongly enhanced in active regions as coronal emission).

The final selection was, inevitably, somewhat subjective. We left out some very strong coronal lines in hopes of broadening the temperature coverage of the payload into the UTR. Some secondary issues also factored into the bandpass selection – for example, the Mg X line at 58 Å was chosen for study even though it essentially duplicated the temperature response of Fe X 180 Å. It was decided that such redundancy offered a valuable cross-check, and could be useful in assessing the validity of assumptions about relative abundances. Also, the relatively short wavelength represented a challenge to the ability of multilayers to operate in the x-ray regime, offering an excellent opportunity to demonstrate the advantages of new multilayer deposition techniques.

The nine candidate bandpasses chosen for flight are plotted against a synthetic active region spectrum from CHIANTI in Figure 5. In Figure 6, the temperature kernels of these bandpasses are displayed. The actual temperature kernels for the EUV instruments based on these bandpasses are derived and plotted in section 2.6.1.
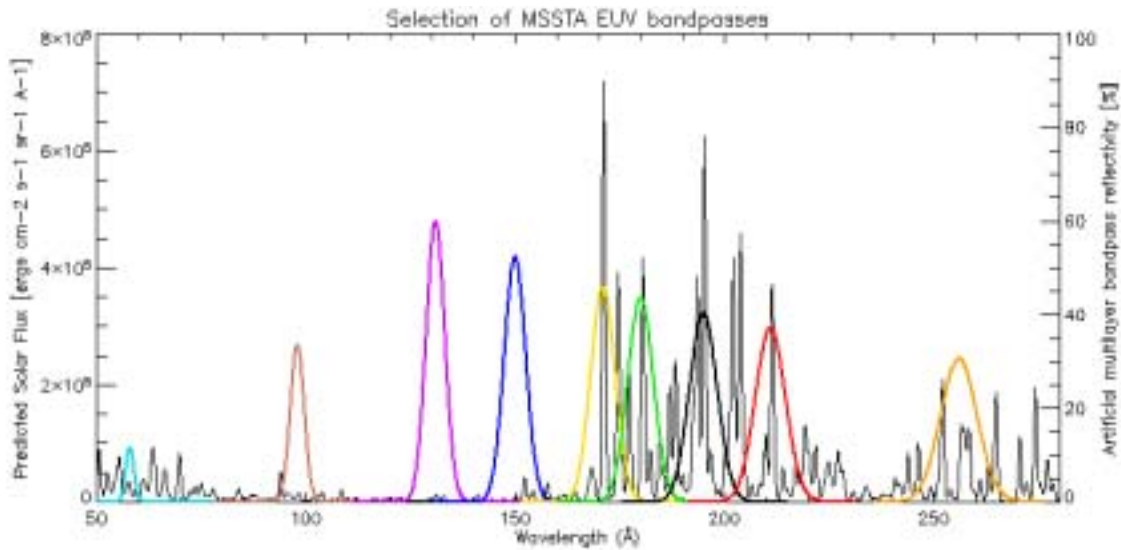
Figure 5. Synthetic spectrum of a solar active region generated with CHIANTI; plotted in red are the idealized Gaussian bandpasses used to select the 9 EUV telescopes of the MSSTA III.
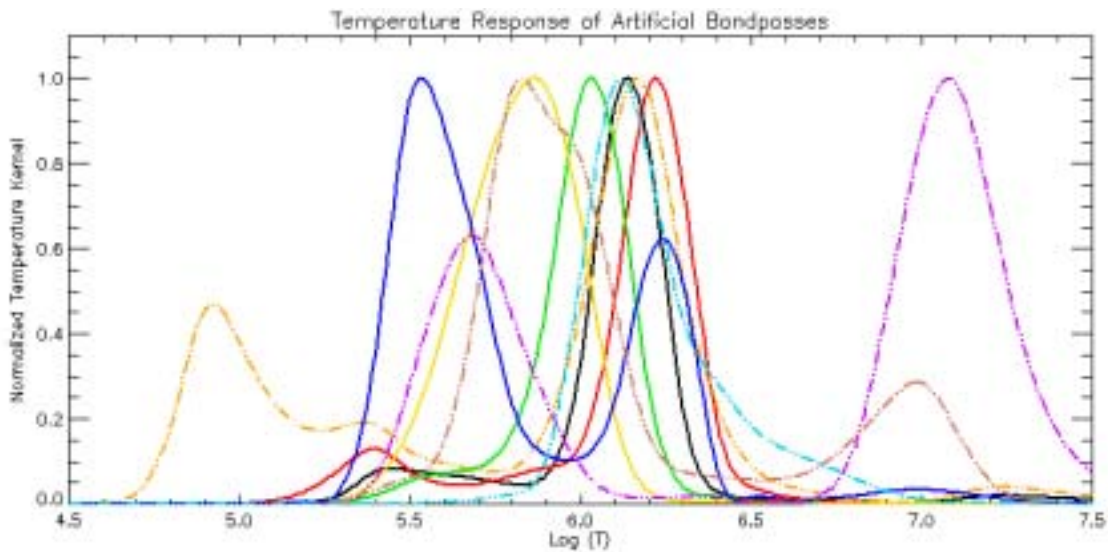
Figure 6. Approximate relative temperature kernels of the MSSTA III EUV telescopes, generated using artificial Gaussian bandpasses. These curves are useful only as a quick look at the bandpass; actual temperature kernels based on measurements of the flight instruments are presented in section 2.6.1.

The technique of discretizing the temperature kernels into an instrument response matrix and analyzing the singular value decomposition of that matrix was not employed, but probably would have been helpful. As discussed in section 4.1.2, the SVD is an excellent way to discover how much information can be extracted from a set of observations based on knowledge of the

instrument used to obtain those observations. It can also provide insight into, for example, what temperatures are well-constrained by a particular set of candidate instruments. The diagnostic ability of the MSSTA instrument package, and some supplements and alternatives, are discussed quantitatively in section 4.2.3.

Instrument Assignment

The front aperture of the MSSTA has slots for 7 telescopes of 127 mm aperture, two of ~100 mm aperture, and two more of 63.5 mm. The truss is configured to use single-reflection Herschelian telescopes, with primary mirrors mounted on the rear bulkhead and back-facing cameras in the middle of the payload, for the 100 mm and one of the 127 mm slots; the other instruments are all two-reflection Ritchey-Chrétien telescopes in self-contained tubes. We divided up the 9 chosen EUV bandpasses among these optical configurations as follows:

- The FUV telescopes are already assembled using 127 mm Ritchey-Chrétien layouts. The 150 Å instrument uses the standard 1000 mm-long, f/28 optics set employed by most of the large Ritchey-Chrétien, while the 1216 Å instrument is built in a slightly shorter, faster tube (800 mm, f/20) designed to mount in the center slot on the payload.

- Solar emission at our short wavelength lines (58 Å, 98 Å, and 131 Å) is fairly weak, and the multilayers are relatively inefficient below 100 Å. Therefore, these three lines were assigned to the Herschelian systems, which offer much faster focal ratios (f/8 – f/15, rather than f/28 or more) than the Ritchey-Chrétiens, along with relatively high efficiency (because they use only a single reflection). The 131 Å bandpass was designated as the highest priority of these 3, and was therefore assigned to the lone 127 mm Herschelian, leaving the 58 Å and 98 Å telescopes on the two 100 mm Herschelians.

- High-resolution images in the 171 Å bandpass were not seen as a high priority, as they are widely available from EIT and TRACE. Rather, the MSSTA 171 Å telescope was primarily chosen to make cross-calibration with those instruments possible. Therefore, it was assigned

to one of the small 63.5 mm f/31 Ritchey-Chrétien telescopes. The 180 Å bandpass was chosen to complement the 171 Å, and was assigned to the other small Ritchey-Chrétien.

- The remaining bandpasses (150 Å, 195 Å, 211 Å and 256 Å) were assigned to 127 mm f/28 Ritchey-Chrétien telescopes. These were generally the highest priority instruments on the MSSTA, as they offer the best combination of photographic speed and resolution capability.[2]

A summary of the 11 telescopes selected and flown on the MSSTA III is presented in Table 1.

All the EUV optics were fabricated from Zerodur, figured and flow-polished by Phil Baker of Baker consulting in 2000-2001. They were cleaned and the multilayer coatings deposited by Troy Barbee of Lawrence Livermore National Laboratory. Appropriate thin-film filters and photographic film for each telescope were selected after the multilayers had been deposited. The calibration and assembly of the instruments, and their final temperature kernels, are described in the following sections.

---

[2] In fact, the 256 Å telescope was not originally chosen, and was not considered a high priority; rather, it was added to the payload to replace the Mg II spectrograph instrument.

Central Wavelength (Ångstroms)	Target Ion	Telescope Design		Goals
		Aperture (mm)	F/Ratio	
58	Mg X	Herschelian		Short wavelength;
		100	15	Coronal (1 MK) material
98	Ne VIII	Herschelian		Transition region
		100	15	(0.7 MK) material
131	Fe VIII	Herschelian		Transition region
		127	8	(and flares, if lucky)
150	O VI	Ritchey-Chrétien		Transition region
		127	28	and coronal material
171	Fe IX	Ritchey-Chrétien		Coronal (1 MK)
		65	31	TRACE/EIT cross-cal
180	Fe X	Ritchey-Chrétien		Coronal (1.1 MK)
		65	31	
195	Fe XII	Ritchey-Chrétien		Coronal (1.5 MK)
		127	28	TRACE/EIT cross-cal
211	Fe XIV	Ritchey-Chrétien		Coronal (2 MK)
		127	28	
256	He II	Ritchey-Chrétien		Chromospheric/LTR
		127	28	EIT 304 comparison
1216	H I	Ritchey-Chrétien		Chromospheric/LTR
		127	16	TRACE cross-cal
1550	C IV / Cont	Ritchey-Chrétien		Chromosphere/TR
		127	28	TRACE cross-cal

**Table 1**. The instruments of the MSSTA III.

2.2 Mirrors

2.2.1 INTRODUCTION

The innovation that made the MSSTA and other solar observatories like it possible was the development of multilayer structures capable of reflecting EUV light with high efficiency at near-normal incidence[(Barbee and Keith 1978), (Spiller 1972)]. A multilayer is a regularly-spaced stack of alternating materials that acts as an artificial Bragg crystal, reflecting energetic photons at an angle determined by the layer spacing,

$$n\lambda = 2d\sin(\theta),$$

as illustrated in Figure 7. Multilayers can be deposited on curved substrates, such as the hyperboloidal mirrors of a Ritchey-Chrétien telescope, resulting in narrowband reflectors with an efficiency of better than 50% and a resolution ($\lambda/\Delta\lambda$) of 30 or more at wavelengths of around 150 Å.

In 1987, Walker et al. obtained the first high-resolution image of the solar atmosphere using multilayer-coated normal incidence optics (Walker, Lindblom et al. 1988). The multilayers were made by Troy Barbee of Lawrence Livermore National Laboratory, who also produced the multilayers for the MSSTA missions. Since then, this technique has become the standard for observations of the solar transition region and corona. The TRACE satellite (Handy, Acton et al. 1999), launched in 1998, represents the current state of the art. It is capable of obtaining high-resolution (1 arc-second) images of the corona in three EUV wavebands using multilayer mirrors made by Troy Barbee. TRACE observations (particularly high-cadence movies of active-region dynamics) have greatly enhanced our understanding of the solar atmosphere.
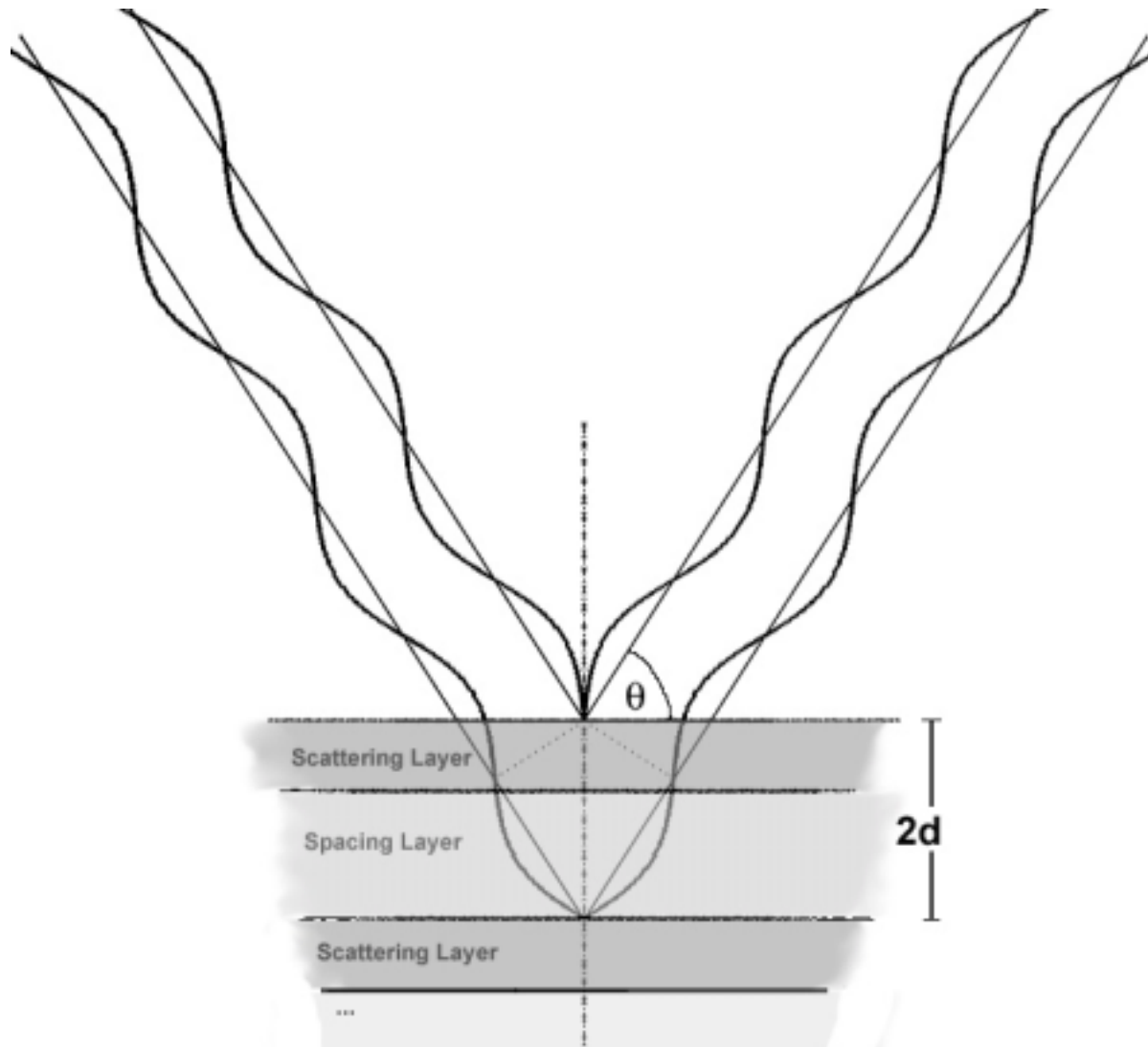
Figure 7. High-energy photons are reflected by a multilayer stack of layer spacing 2d if their wavelength and angle of incidence satisfy the Bragg condition (resulting in constructive interference of the reflections from different layers).

Making a multilayer structure with layers as small as the wavelength of EUV or soft x-ray light is extremely challenging, and places strict demands on the smoothness of the substrate and the control of the deposition process. Scattering by irregularities in the layer interfaces becomes increasingly problematic as the layers grow thinner, and at present limits the utility of multilayers for normal-incidence reflection to wavelengths longer than ~40 Å. On the long-wavelength side, the short penetration depth of less-energetic EUV photons makes multilayers relatively inefficient for wavelengths longer than about 300 Å (such photons are almost all scattered or absorbed by

the top few layers in the stack; the more layers sampled by the incident beam, the narrower the bandwidth and the higher the reflection efficiency).

The MSSTA III used multilayer-coated mirrors centered on solar emission lines ranging from 57.9 Å to 256 Å. The multilayers consist of 25-100 bilayer pairs Mo_2C and Si or W/C multilayers, and were fabricated by Troy Barbee. Improvements in multilayer fabrication – new materials, smoother substrates, more precise control of the deposition process – have lead to corresponding improvements in mirror performance. New multilayers offer higher reflectivity, narrower bandwidths, and better stability than those produced just a few years ago. At the time of their launch, the multilayers on the MSSTA III telescopes were the most advanced suite of EUV imaging optics yet used for solar observations. In this section, I will discuss the calibration of the MSSTA mirrors.

2.2.2   CALIBRATION OF THE MSSTA III MULTILAYER MIRRORS

The early successes of EUV-reflective multilayers, including those used on the first MSSTA flight, have opened up a broad and exciting field of research. Multilayers are being developed for applications ranging from lithography for microfabrication to high-energy laser optics to high-resolution microscopy. The drive to improve multilayer technology has lead to the creation of facilities optimized for testing and characterization of multilayers. Beamline 6.3.2 at the Advanced Light Source synchrotron of Lawrence Berkeley National Laboratory (http://www-cxro.lbl.gov/als6.3.2/; (Underwood, Gullikson et al. 1996))is one such facility. On line since 1995, beamline 6.3.2 is ideally suited to measuring reflectivity of multilayer optics like the MSSTA telescope mirrors. Figure 8 shows the layout of the beamline.
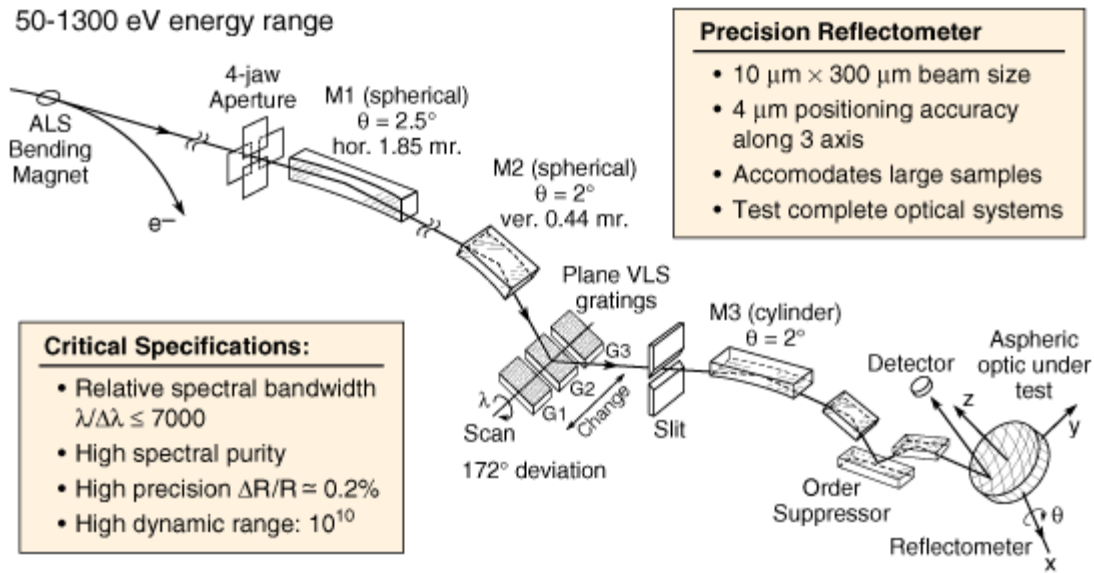
Figure 8. Beamline 6.3.2 (taken from (Gullikson, Mrowka et al. 2001)). Key features include the tunable three-reflection order suppressor, which can limit higher-order contamination to 0.25% by selection of appropriate materials and grazing angles; the selectable variable line spacing gratings, which enable the monochromator to cover the wavelength range from ~10 – 250 Å; and the reflectometer end station, which allows for easy and precise positioning of the optic and the detector.

We obtained 10 shifts of beam time over a four-day period in December 2001, and in this time were able to measure the primary mirrors of all 9 EUV telescopes, and several of the telescope secondary mirrors as well. Thanks to the excellent spectral purity, brightness and mechanical design of beamline 6.3.2, the data we obtained have a higher signal-to-noise ratio and lower systematic errors than those gathered in previous MSSTA calibration experiments at other synchrotrons, experiments that generally took several weeks to complete.

The procedure used in the calibration measurements is summarized below, with particular attention to issues that may impact the accuracy of the final reflectivity values.

The optic to be tested was mounted in the reflectometer vacuum chamber. The mounting stage allows three-axis positioning of the optic, and two-axis rotation (to vary angle of incidence with the test beam, and azimuthal position of the beam on the optic). We designed an adapter plate that would allow the on-axis Ritchey-Chrétien mirrors to be mounted in their cells with their centers on the rotation axis of the stage. Thus, azimuthal rotation of the optic allowed us to sample different points on the mirror surface without having to realign the beam and detector.

Each time the optic was changed, several steps were taken to ensure accurate wavelength calibration of the monochromator. First, a silicon prefilter was placed in front of the detector, and the monochromator scanned over 123.8 – 124.8 Å. The resulting transmission scan showed the L-absorption edge of the Si; if the wavelength scale of the edge appeared substantially different from its known value, an offset was entered into the monochromator motors. This process could be iterated to increase the calibration accuracy; in general, once calibrated the monochromator wavelength remained accurate to better than 0.01 Å. Then, if the Si prefilter was not appropriate for the wavelength being tested, it was exchanged for another prefilter (Al, Be, B, or C), and the order suppressor was adjusted for the wavelength region of interest. Since higher orders are less efficiently reflected at large grazing angles, the combination of the prefilter and the three-reflection order sorter strongly attenuates high-order contamination, to as little as 0.25% of the total beam flux. (Past MSSTA calibration runs have been plagued by higher order contamination as large as 30%, so this was a substantial improvement.)

For reflectivity measurements, the optic was positioned at an 85° angle to the incident beam. (In practice, because the position and angle at which the beam reaches the surface of the optic is not fixed by the reflectometer, this involved positioning the detector to receive a beam directed deflected by 170° from the incident beam, which is as close to normal incidence as the reflectometer geometry allows, without having the detector block the beam. The position and tilt of the optic are then adjusted in order to maximize the signal, indicating the full beam is reaching the detector. There was a large "sweet spot" in this adjustment over which the signal was constant and maximum, suggesting that misalignment was not a problem in these measurements).

With the beam, optic and detector aligned, the angle of the grating was scanned to scan the wavelength of the monochromator over the bandpass of the optic. Three samples were taken at each wavelength step, with a 30 msec integration time, and averaged. The data acquisition system reported the detector signal and current in the synchrotron ring for each point. After the full wavelength scan, the optic was rotated in azimuth so that the beam found a new point on the optic; the alignment was re-optimized, and the wavelength scan repeated. On the Ritchey-Chrétien systems, re-optimization was trivial, as the angle of reflection was essentially unchanged by azimuthal rotation around the optical axis of the mirror. For the primaries, 6-12 surface points

were measured; for the secondaries, only one. The Herschelian mirrors are off-axis, and thus lacked the symmetry that made sampling different points on the Ritchey-Chrétien mirrors so simple. Each different point on a Herschelian mirror required complete realignment of the optic and detector, and thus these mirrors were only sampled at 1-3 points each.

Before and after scanning the bandpass at all the points on an optic, several scans were taken to aid in calibrating the results. First a "direct beam" scan, with the optic pulled aside and the synchrotron beam directly incident on the detector, was taken, to establish the intensity of the beam itself as a function of wavelength. Then dark current in the detector (and the background light in the chamber) was measured by blocking the synchrotron beam and measuring the detector signal while the monochromator scanned (of course, the action of the monochromator was irrelevant while the beam was blocked). After the optic was moved into place, another dark current scan was taken in case the position of the optic changed the amount of background light that reached the detector. Table 2 summarizes the data acquired at the ALS for each mirror.

Central Wavelength	Optic Tested	Number of Points Measured	Number of Repeat Measurements	Number of Angles Measured
58	Herschelian	2	1	8
98	Herschelian	2	2	9
131	Herschelian	1	2	1
150	R.-C. Primary	6	2	1
171	R.-C. Primary	6	2	1
180	R.-C. Secondary	1	2	1
195	R.-C. Primary	12	3	1
211	R.-C. Primary	8	3	1
256	R.-C. Primary	12	2	1

Table 2. Summary of the measurements made at the ALS. Most optics were measured at different points on their surface (in order to estimate the uniformity of the multilayer bandpass), and measured repeatedly at the same point (to measure the repeatability of our calibration technique). Certain mirrors were also measured at a range of angles of incidence to test the validity of correcting for the measurement angle. For the two-mirror systems, only one mirror was measured (generally the primary), and the bandpass on the second mirror was assumed to be the same.

2.2.3 ANALYSIS OF THE MULTILAYER CALIBRATION DATA

The following quantities were measured for each mirror:

$$S_{(R/D)}(\lambda;\theta,\mathbf{x})$$
$$D_{(R/D)}$$
$$C_{(R/D)}(\lambda;\theta,\mathbf{x})$$

where S is the strength of the signal from the photodiode, measuring either the direct beam (S_D) or the beam reflected at angle θ from point $\mathbf{x}$ on the mirror surface (S_R); D is the strength of the dark current, measured before or after a given reflected or direct beam scan and averaged over wavelength (it can be attributed to thermal noise in the photodiode or background light in the experimental chamber); and C is the ring current at the time when each value of S was measured. The ring current determines the strength of the synchrotron beam; it decays over time as the electrons in the accelerator radiate away their kinetic energy (the electrons are dumped and a new packet is injected into the ring once a day). Ring current was used as an overall normalization factor for the beam strength at each sample point. Note that C is not actually dependent on λ, θ or $\mathbf{x}$; however, a different value of C is reported by the beamline data acquisition system simultaneously with each value of S, and the appropriate samples must be matched up. S and D have units of counts/sec, and must be adjusted for the gain of the photodiode.

Dividing the reflected intensity spectrum by the direct beam intensity spectrum effectively corrects for any λ dependence in the response of the photodiode or in the output of the synchrotron, and gives us the reflectivity of the multilayer:

(Equation 8)
$$R(\lambda,\theta,\mathbf{x}) = \frac{\left(S_R(\lambda,\theta,\mathbf{x}) - D_R\right) \Big/ C_R(\lambda,\theta,\mathbf{x})}{\left(S_D(\lambda) - D_D\right) \Big/ C_D(\lambda)}$$

Generally, θ was fixed at 85° during the measurements. Since the effective spacing (the induced phase shift) of the multilayer stack is $\sin(\theta)$ times the actual layer spacing, the measured results were converted to normal incidence (90°) reflectivities by multiplying the measurement wavelengths by $\sin(85°)$ (the validity of this correction procedure is discussed in section 2.2.5). Finally, the measurements at different points $\mathbf{x}$ on the mirror surface were cross-checked for consistency and averaged, producing an effective normal-incidence reflectivity $R_{eff}(\lambda)$:

$$R_{eff}(\lambda) = \left[R(\lambda \sin(85°), 85°, \mathbf{x}) \right]_{\mathbf{x}}$$

Except as noted below, all the sampled points were included in the average and weighted equally. The effect of sampling different points on the optic is discussed in section 2.2.4.

Figure 9 presents the calibrated reflectivities of the 9 MSSTA III EUV multilayer telescopes.
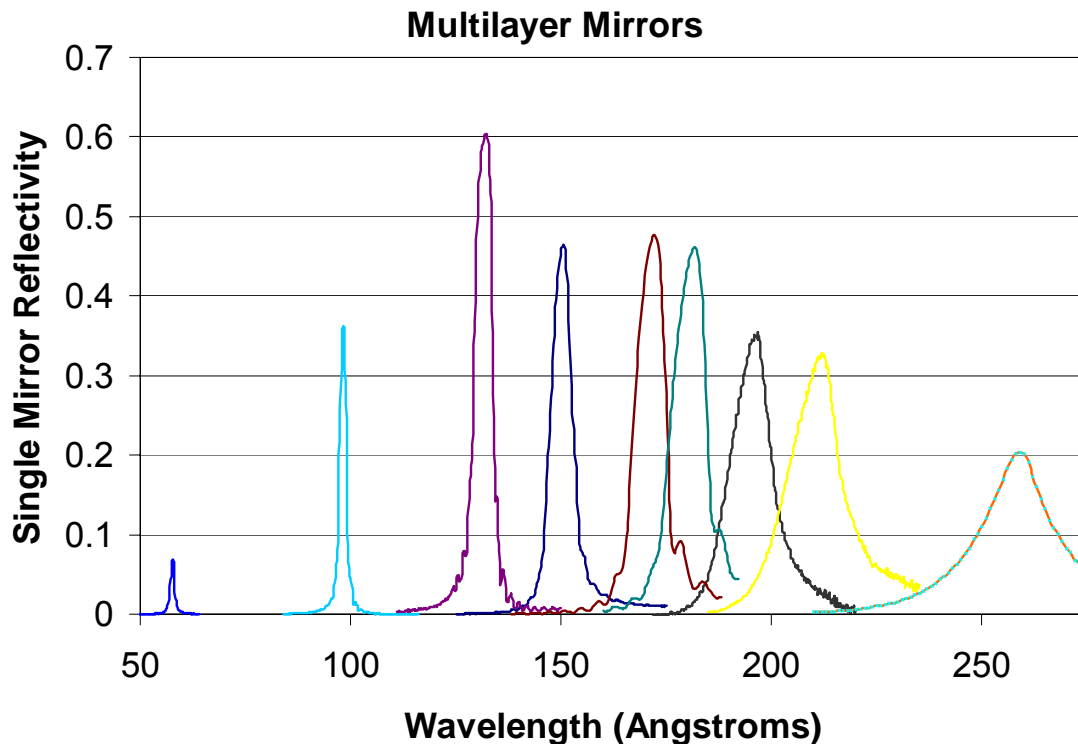
Figure 9. Reflectivity of the multilayer mirrors used in the MSSTA III EUV telescopes. Note that these are all single-mirror reflectivities; the efficiency of the two-mirror Ritchey-Chrétien systems is found by squaring the single-mirror bandpass.

46

2.2.4   NOISE AND ERROR

Because ALS beamline 6.3.2 is so well optimized for EUV multilayer reflectometry, we were able to obtain substantially more and better mirror data than has been available from previous MSSTA calibration efforts. In particular, by measuring each optic multiple times at different points, we are able to estimate the error in the final bandpass and identify the source of this uncertainty.

In the center of the synchrotron's wavelength range, the brightness of the beam is extremely high, resulting in smooth curves with an excellent signal-to-noise ratio (see, for example, the measurements of the 131 Å Herschelian in Figure 16). The beamline's output begins to drop off at wavelengths longer than ~200 Å, and is quite low above 250 Å, so the bandpass measurements of the longer-wavelength optics like the 211 Å and 256 Å Ritchey-Chrétiens (Figures 10 and 11) are noticeably noisy. However, photon statistics are not the largest error source for any of the instrument bandpasses.

There are two significant sources of systematic error in the measured reflectivity curves. The first is measurement error introduced by our experimental procedure. Because each reflectivity curve requires four synchrotron scans to produce (signal and dark current scans for the direct and reflected beams; Equation 8), any uncontrolled variation that affects one of these scans but not the others will throw off the resulting reflectivity. In particular, the dark current measurements showed some tendency to drift with time as the diode's temperature varied.

In order to estimate the effect of this systematic measurement error, we sampled the same point on each optic twice, using two completely separate sets of four synchrotron scans. The results are plotted in the upper panels of Figures 10 – 18. In most cases, the agreement was quite good, with differences of roughly the same order as the statistical noise (<1% at wavelengths up to 180 Å; ±1-5% at longer wavelengths).

The second major source of error is the fact that we only sample a few points on the optic; if the multilayer bandpass varies substantially over the surface, we can only construct an average

47

bandpass that may not represent the mirror's overall properties. The lower left panels of Figures 10 – 18 show the result of sampling different points on the optic (generally 6-12 points for the Ritchey-Chrétien primaries; only 1 or 2 for the Herschelians). Evidently, point-to-point variation over large optics is a factor; for the small Ritchey-Chrétien 171 Å mirror (Figure 14), there is very little deviation in the bandpass at different points, but the 5" primary on the 150 Å Ritchey-Chrétien (Figure 15) shows substantial variation that dominates the uncertainty in the average bandpass. (As discussed in section 2.6.2, this uncertainty complicates the interpretation of the 150 Å telescope's images.)

The results and estimated errors of the MSSTA III EUV mirror bandpass measurements are presented in Table 3.

| Wavelength of Measured Peak (Å)	Measured Peak Reflectivity (%)	FWHM (Å)	% Error at peak	RMS % Error Over Bandpass
58.0	9.2	0.8	5	7
98.6	36.2	1.9	2	15
132.5	60.4	4.8	*0*	*0*
151.2	46.5	6.0	7	24
172.7	47.7	8.3	1	4
182.5	46.1	9.5	*0*	*1*
197.6	37.5	12.0	11	17
212.8	32.9	14.0	10	16
260.0	20.4	18.3	20	25

Table 3. Results of the bandpass measurements of the MSSTA III multilayers. The error estimates are dominated by point-to-point variations in the reflectivity over the surface of the optic. Because the 131 Å and 180 Å telescopes were only measured at a single point, we cannot confidently estimate the error of these bandpasses.
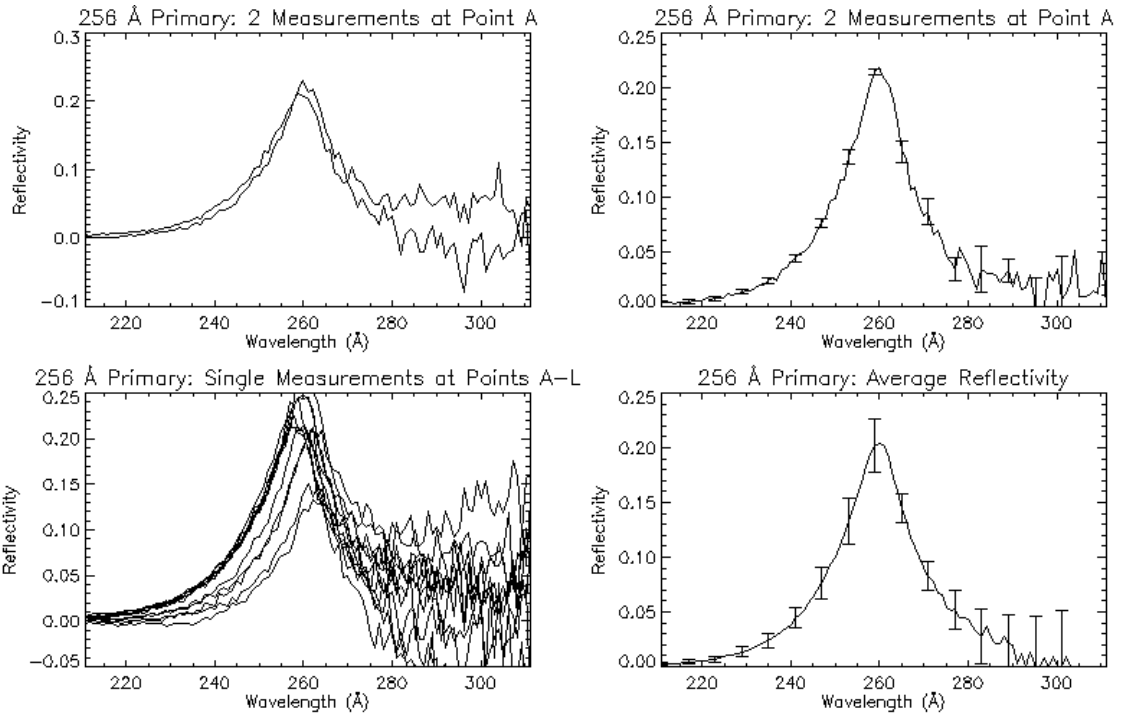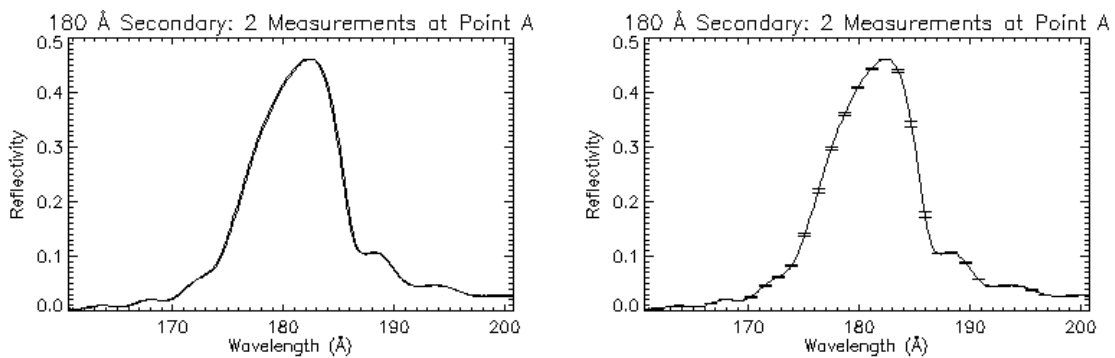
Figure 10. Measurements of the 256 Å Ritchey-Chrétien primary mirror. Wavelengths longer than 250 Å are outside the synchrotron's nominal range, so the throughput is low and the data is extremely noisy.
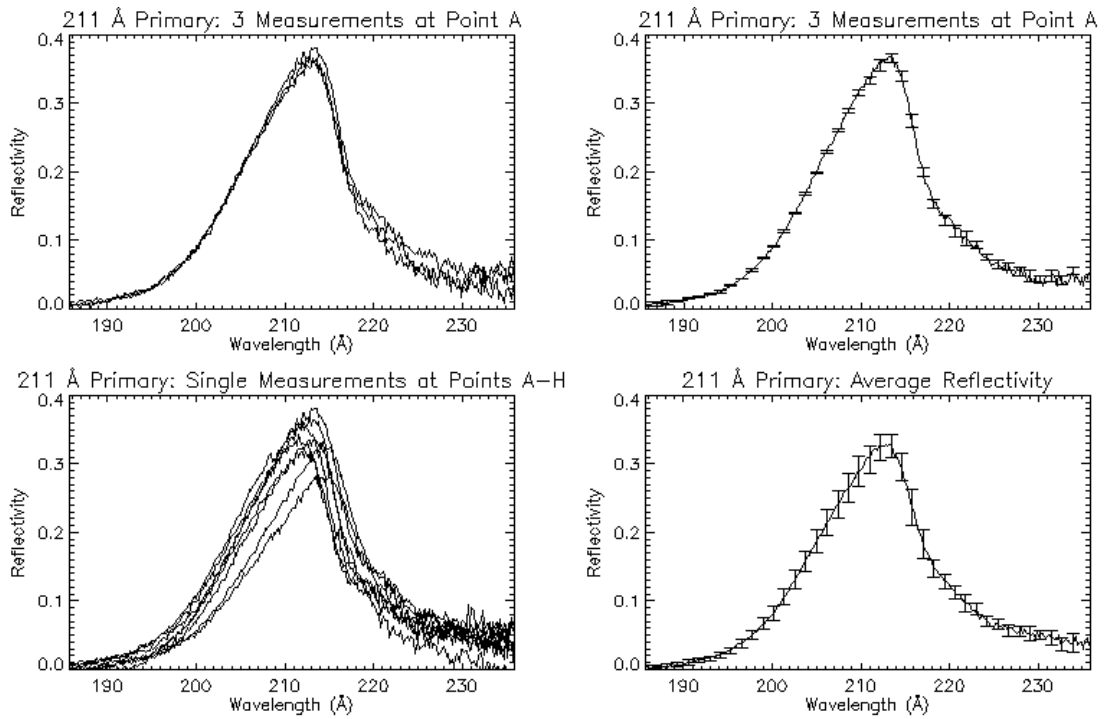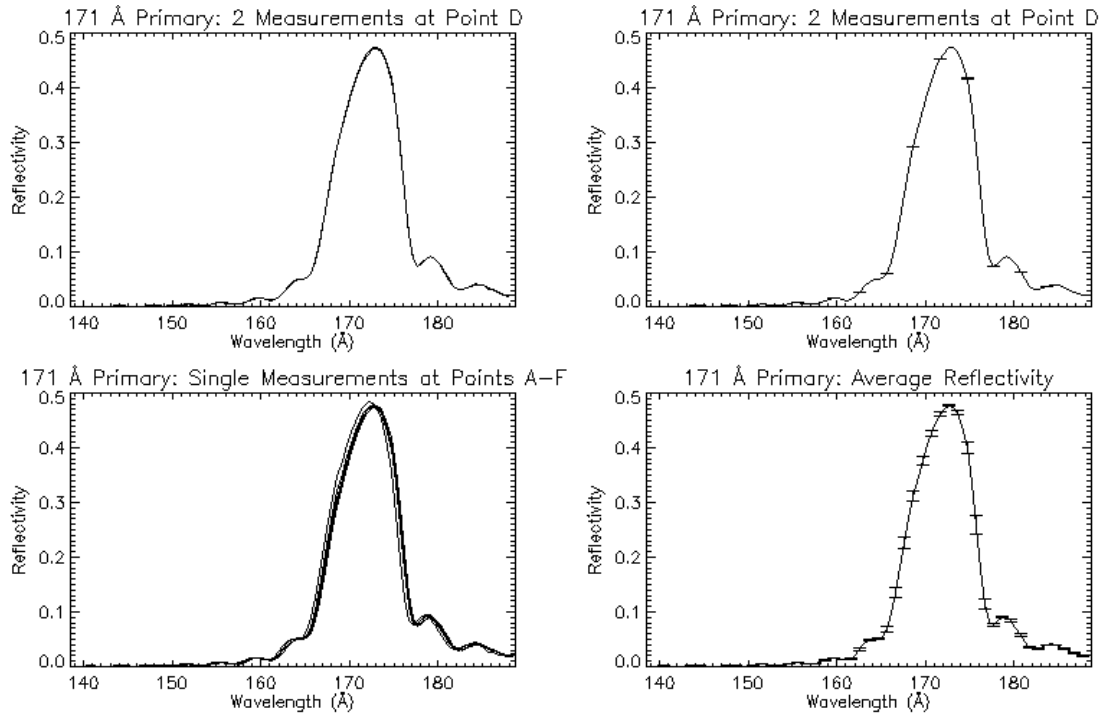

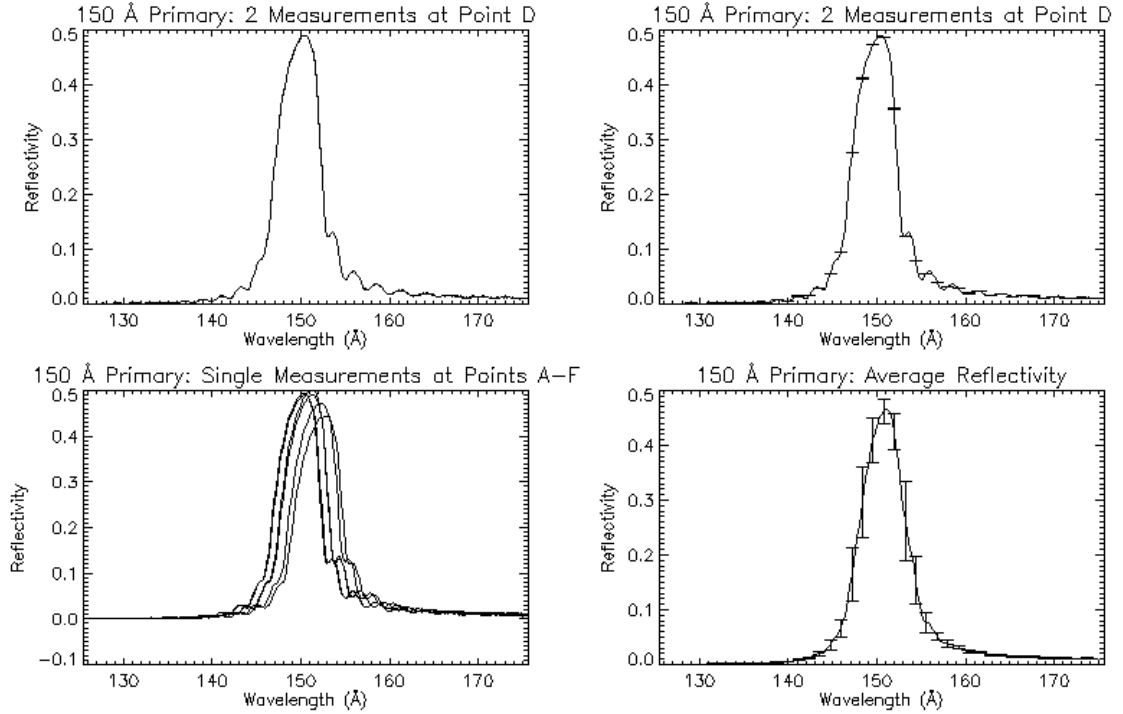**Figure 11.** Measurements of the 211 Å Ritchey-Chrétien primary.
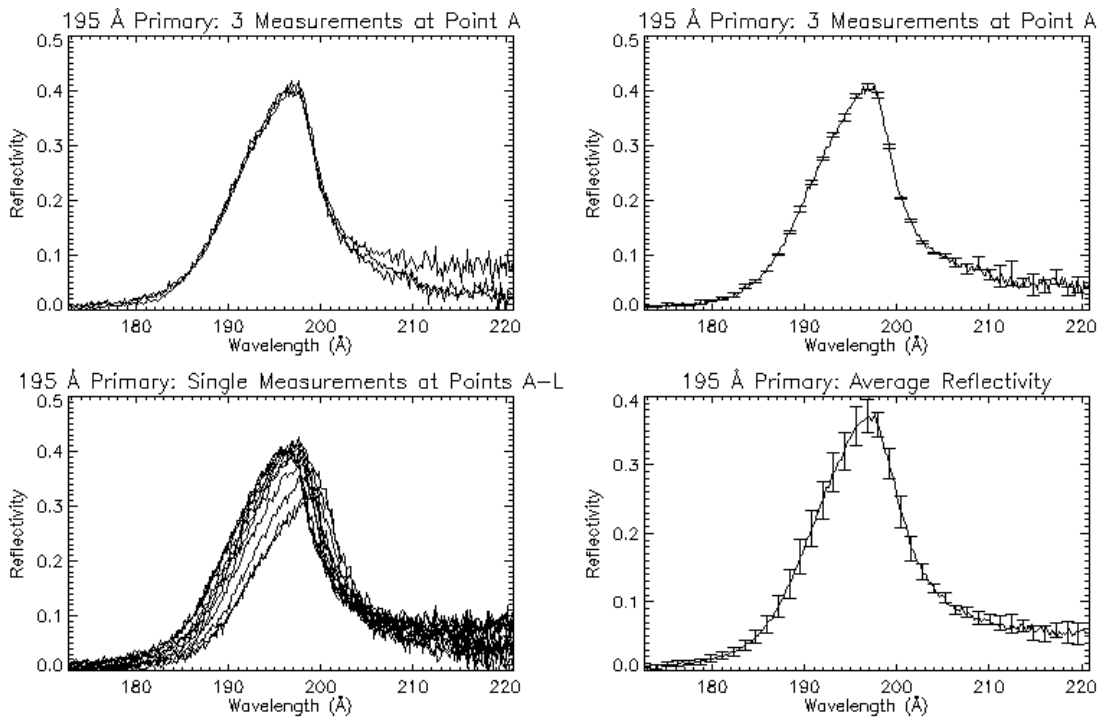
**Figure 12.** Measurements of the 195 Å Ritchey-Chrétien primary.

Figure **13.** Measurements of the 180 Å Ritchey-Chrétien secondary. Because of the secondary's small size, the mirror was only measured at one point.
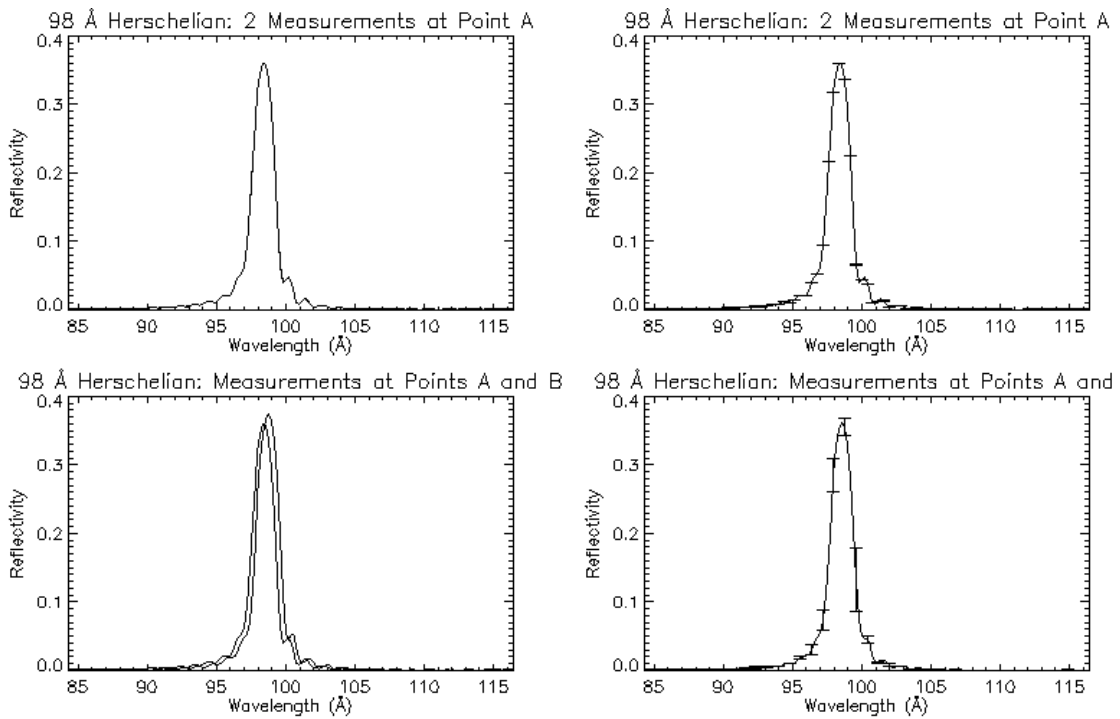
50

Figure 14. Measurements of the 171 Å Ritchey-Chrétien primary.

Figure 15. Measurements of the 150 Å Ritchey-Chrétien primary, showing substantial point-to-point variations over the optic.
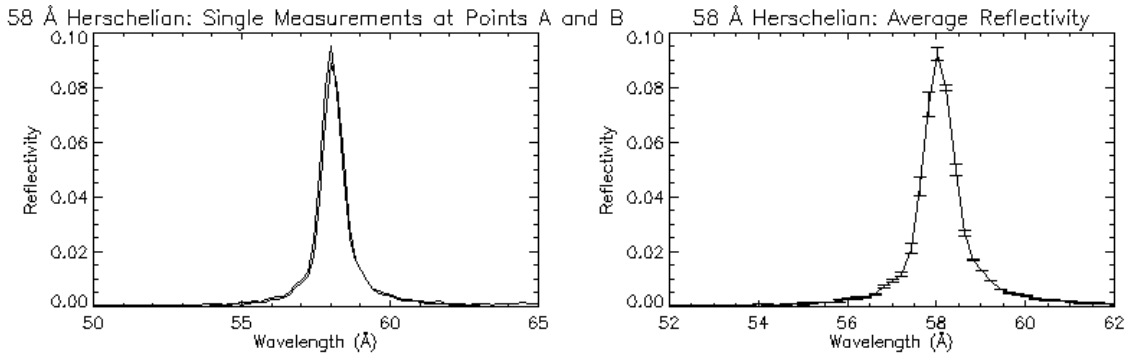
51
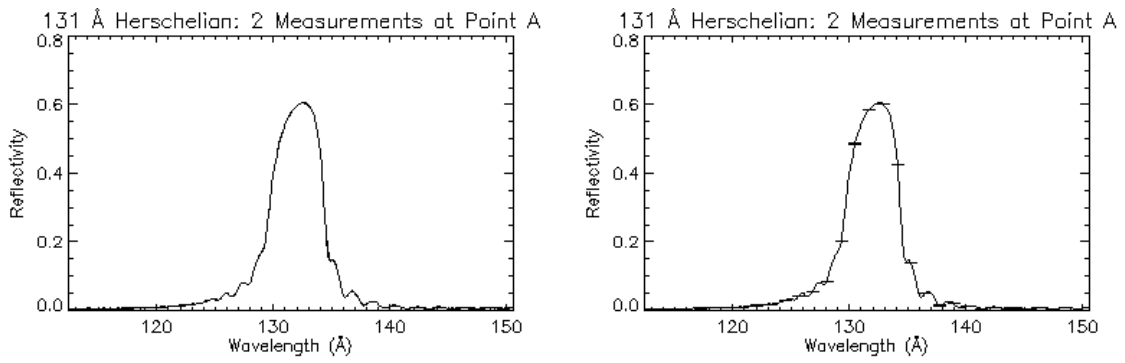
Figure 16. Measurements of the 131 Å Herschelian. The multilayer was only sampled at a single point.

Figure 17. Measurements of the 98 Å Herschelian.

52

Figure 18. Measurements of the 58 Å Herschelian. Repeat measurements at a single point were not taken.


2.2.5   ANGLE OF INCIDENCE VARIATION

In flight, the MSSTA III telescopes focus light by reflecting at angles that vary from 80.0° (for the farthest off-axis point on the 131 Å Herschelian) to 89.8° (for points near the center of the large Ritchey-Chrétien secondaries). Since the effective spacing of the multilayer stack is $\sin(\theta)$ times the actual layer spacing, this variation in angle of incidence, and the difference between the angle at which the multilayers were measured and at which they operate, will have a small but noticeable effect, of order $(\theta/90°)^2$, on the instrument's bandpass. The multilayer measurements have been corrected to give reflectivity at normal (90°) incidence (shifting the peak reflectivity to longer wavelengths).

In order to test the validity of this correction, we measured two of the Herschelian mirrors (the 98 Å and 58 Å Herschelians) at a range of angles, as noted in Table 2. The results are shown in Figure 20 and Figure 21. The bandpass shifts agree reasonably well with the $\sin(\theta)$ prediction (represented by the curve through the 87° data point). In the case of the 98 Å Herschelian, the total reflectivity is seen to decrease at shallower angles of incidence, evidently as a result of scattering or absorption within the multilayer. This effect was not compensated for in generating the instrument bandpass used for analysis.

It is possible to generate a bandpass that accurately accounts for the variation in angle of incidence over the surface of an optic and at the image plane (i.e. the fact that the edges of the on-axis Ritchey-Chrétien primary mirrors reflect incident light at a different angle than points near

the center). Figure 19 shows the effective bandpass of the 131 Å Herschelian telescope for a point at the center of the image plane. It is slightly broadened, and slightly shifted to lower wavelengths, by the fact that various rays are reflected at angles slightly less than normal. Because this effect is fairly subtle (especially for on-axis mirrors), and because the computation is complex and the result varies for every point in the image, this effect was ignored in our bandpasses, but in the case of the short-wavelength Herschelian mirrors (which feature narrow reflectivity curves and substantial angle-of-incidence variation) it can become significant.
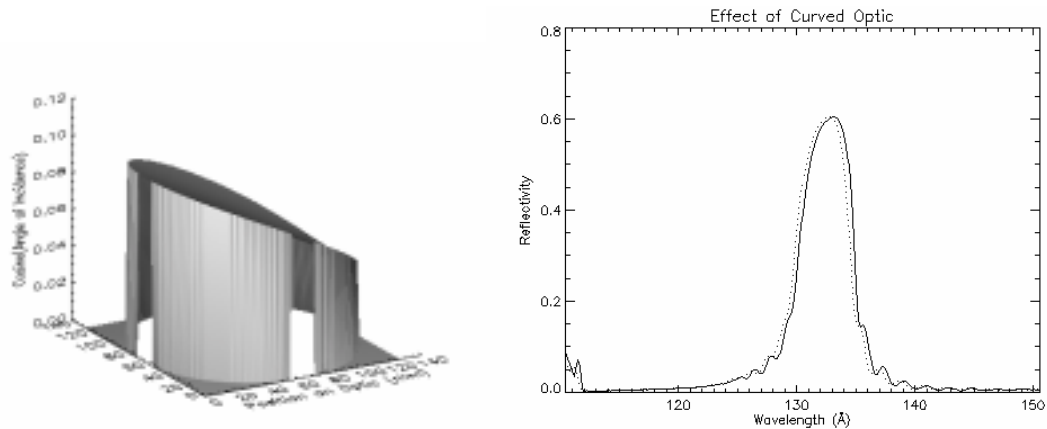
Figure 19. Because the effective bandpass of the multilayer depends on the angle of incidence of light, a curved optic behaves slightly differently than a flat optic at normal incidence. On the left, the cosine of the angle of incidence of rays destined for the center of the image plane of the MSSTA III large Herschelian telescope is shown; at right, the effect of this variation on the effective bandpass of the optic is plotted, showing a slight broadening and a slight shift to lower wavelengths. This subtle effect can become more dramatic with steeply curved optics or narrow, short-wavelength multilayer bandpasses.
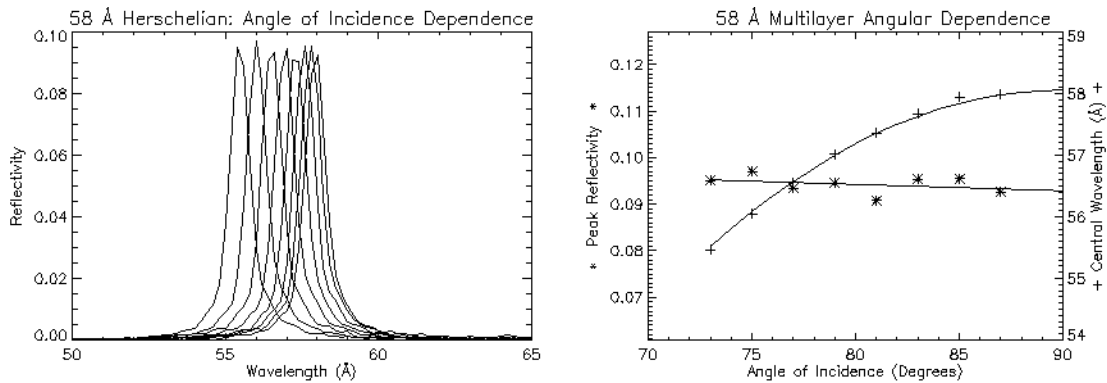
Figure 20. Varying the angle of incidence on the 58 Å Herschelian. The curves on the left show measurements taken at angles ranging from 73° to 87°. At right, it can be seen that the bandpass shifts to longer wavelengths with increasing angle of incidence, as predicted by simple geometry. The peak reflectivity is not affected noticeably by changing angle.

54
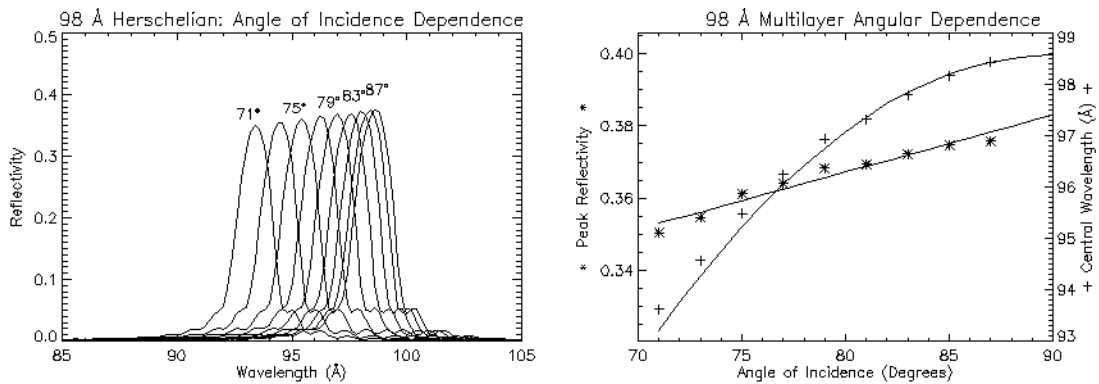
Figure 21. Varying the angle of incidence on the 98 Å Herschelian mirror. The bandpass shift matches the prediction reasonably well. There is a more significant decline in the peak reflectivity at shallower angles than what is seen with the 58 Å mirror, as the light path through the material lengthens. This seems to indicate that the peak reflectivity at 90° is ~38%, rather than the 36% we measured at 85°. This effect was not compensated for.
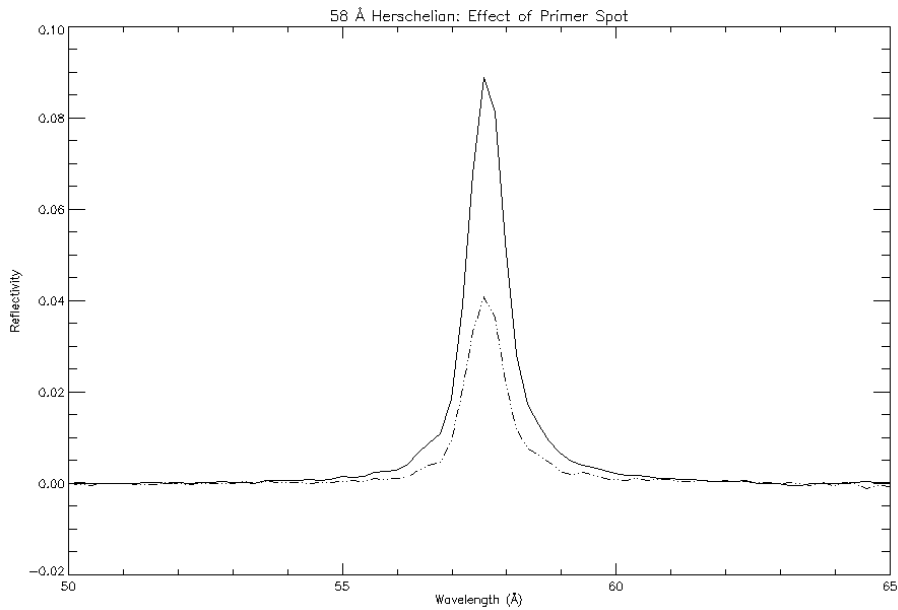
2.2.6   MIRROR POTTING

Holding the mirrors securely enough to maintain critical telescope alignment through the rocket launch, without exerting enough stress to deform the mirror surfaces and degrade their performance, is quite challenging. The Herschelian and Ritchey-Chrétien primary mirrors were mounted in aluminum cells as follows: the outside edge of the zerodur mirror blanks and the inside edge of the aluminum mirror cells were coated in primer. The mirrors were placed face-up on a set of standoffs. Then the aluminum mirror cells were lowered over them (the cells were designed to offer ~⅛" clearance all the way around the OD of the mirror). We then injected ~5 cc of Dow-Corning Silastic RTV through each of a series of 6-12 evenly-spaced cutouts in the mirror cell. The RTV formed pads around the mirror that bound the mirror to the cell; when cured, it is extremely strong, but (in principle) offers enough flexibility to allow the mirror to stabilize without being strained. A set of three aluminum détentes were attached to each mirror cell and overhung the front of the mirror, to prevent the mirror from flying loose in the payload in case it broke free from the RTV. These did not contact the mirror surface.

The Ritchey-Chrétien secondary mirrors were held in their cells less gently: a nylon retaining ring was inserted in the cell; then the mirror was lowered into place, and a pressure plate was attached

to the cell behind the mirror. Nylon-tipped set screws in the pressure plate pushed on the back of the secondary mirror, while the front of the mirror rested on the retaining ring. The small Ritchey-Chrétien secondaries (171 and 180 Å) were a particularly tight fit in their cells, and the performance of these telescopes suffered as a result.

During the application of the primer to the Herschelian mirrors, droplets of primer were inadvertently splashed on the front surface of the 58 Å, 98 Å and 131 Å telescopes. Gentle washing removed some of this contamination, but dried primer spots remained on these mirrors. They covered much less than 1% of the surface area of all of the affected mirrors. The effect of the primer on EUV reflectivity was measured (see Figure 22), but no further action was taken to account for these minor blemishes on the multilayers.

Figure 22. The surface of the 58 Å Herschelian was splattered with spots of primer during mirror potting. Shown here is the effect of the primer on the mirror reflectivity (a uniform decrease of ~60%); because of the small area covered by the primer, this effect was largely ignored.

56

2.3 Filters

2.3.1   INTRODUCTION

While the multilayer mirrors of the MSSTA telescopes are efficient, narrowband reflectors in the extreme ultraviolet, they are also ~50% reflective (via simple specular reflectivity) at visible and near-infrared wavelengths. Because the integrated solar blackbody irradiance at visible wavelengths can be eight or more orders of magnitude stronger than the flux from a single EUV emission line, filtering out the longer-wavelength solar radiation while allowing the EUV photons through the telescope is an important design challenge.

The MSSTA telescopes use a variety of thin metallic foils, composed of aluminum, zirconium, or niobium and mounted just in front of the focal plane of each telescope, to reject the visible light. The filters typically consist of a 1500-4500 Å thick metal film deposited on a mesh of nickel wires, spread over a 2" diameter frame. Such thin foils are extremely vulnerable to damage from differential pressure or heating, and require special precautions in their manufacture and use. These filters were manufactured by Luxel Corporation.

In addition to their primary function of blocking visible/IR light, the filters accomplish a number of secondary tasks, including:

- blocking photons from out-of-band EUV and FUV emission lines (particularly He II 304 Å), whose wavelengths are long enough that they experience some specular reflectivity from the multilayer mirrors;

- narrowing the EUV bandpass with carefully chosen absorption edges (particularly the 171 Å bandpass, where the absorption edge of the aluminum filter sharpens the high-energy cutoff of the bandpass);

- reducing higher-order contamination by EUV emission lines with wavelengths roughly half that of the line of interest.

These tasks must, of course, be accomplished while minimizing the attenuation of the target wavelength.

2.3.2 SINGLE VS. DOUBLE FILTERS

The primary failure mode of the thin-foil filters is the development of pinholes. Mechanical stress and heating by concentrated solar flux can produce thin spots or tiny punctures in the foil, and even microscopic holes in the filter can cause it to be out of specification. Because the filters are close to the focal plane, the effect of a small pinhole on the final image is localized; however, a large enough flaw could let in sufficient visible light to ruin an entire exposure (or even damage the detector).

In order to reduce the risk of total instrument failure from the formation of pinholes, the MSSTA I and TRACE missions used double filters – two focal plane filters, each slightly thinner than what would be required of a single filter. The rationale was that a pinhole that developed in one filter would be unlikely to coincide with a pinhole in the second filter, so no part of the detector would be exposed to completely unfiltered solar radiation. However, because the robustness of a filter is dependent on its thickness, double filtering has two important drawbacks: first, the two filters must be made more than half as thick as an optimized single filter, and thus the total thickness of the filter stack is greater than optimal, resulting in a reduction below optimal levels of the in-band flux; second, because each of the double filters is thinner than an optimized single filter, each is more vulnerable to damage from vibration or pressure differentials created during the rocket launch, and thus the risk of catastrophic filter failure is not necessarily decreased over

using a single filter. After consultation with Forbes Powell of Luxel, it was decided that single filters offered better overall stability and performance.

2.3.3   FILTER MATERIALS

Light is attenuated exponentially as it passes through any material; the transmission of light at wavelength λ in passing through a filter of material Z and thickness d can be written:

(Equation 9) $$T_Z(\lambda, d) = e^{-d\mu_Z(\lambda)}$$

where the function $\mu_Z(\lambda)$ describes the absorption spectrum of the material. Luxel Corporation has manufactured filters for a number of soft x-ray applications, and has compiled a large database of absorption coefficients for different materials from a variety of sources[(Henke, Gullikson et al. 1993), (Palik 1985; Palik 1991)]. These include "practical" visible light absorption coefficients, a single number for each material that can be used to generate conservative estimates of the visible light rejection of a filter of that material (Powell and Fox 1994).

Typically, materials used in filters have μ_z values around $10^{-2} - 10^{-3}$ Å^{-1} at visible wavelengths, and μ_z of a few 10^{-4} at EUV wavelengths, and thus can attenuate visible light by many order of magnitude without reducing EUV throughput by even a factor of ten. Of these materials, aluminum is preferred; it offers a very high relative attenuation of visible light, and has been used extensively, so that its mechanical robustness and ability to withstand the heat load of concentrated visible light are well known. Wherever possible, aluminum filters were used for the MSSTA telescopes. However, aluminum has two drawbacks:

- it has a sharp absorption edge at 170 Å, and EUV wavelengths shorter than this are strongly attenuated;

- it does not attenuate longer-wavelength EUV lines, particularly 304 Å He II.

Therefore, the MSSTA telescopes centered on lines below 170 Å cannot use aluminum filters, and those above 170 Å must supplement their aluminum filters with a thinner coating of some material that will attenuate the 304 Å flux.

Finding a material that strongly attenuates 304 Å while passing photons within the MSSTA bandpasses from 171 – 256 Å is challenging. Zirconium was chosen for the supplemental coating on the aluminum filters, for its relatively high absorption at 304 Å and its good stability. Pure zirconium filters were produced for the 150 Å, 131 Å, and 98 Å telescopes, which fall below the aluminum absorption edge. Because the 58 Å line falls below the absorption edge of zirconium, niobium was used to make a filter for the 58 Å Mg X telescope. Figure 23 shows the absorption spectra of the materials used for the MSSTA filters, along with the bandpasses of the MSSTA instruments.
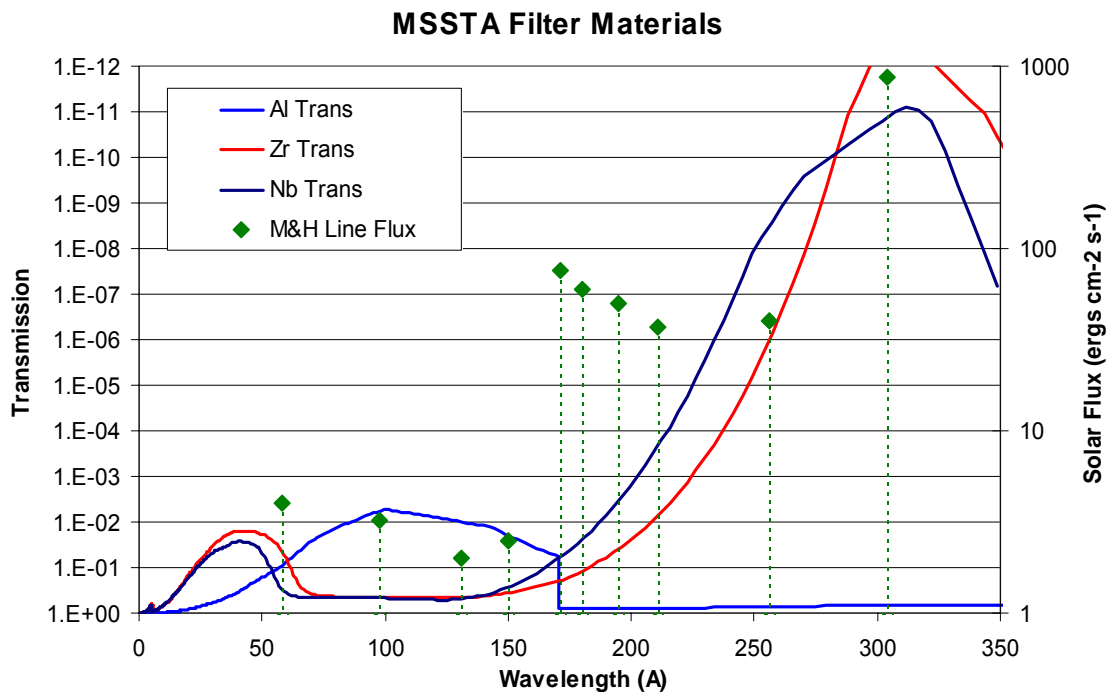
Figure 23. Absorption spectra of the materials used in the MSSTA III filters. The thickness of each material plotted here was chosen to achieve a visible-light attenuation of 10^{-12}. Aluminum is reliable and very effective at attenuating visible light while passing EUV; it was used wherever possible. Zirconium was used to supplement the aluminum filters to reject 304 Å light, and to filter three of the telescopes below the aluminum edge. Niobium was used to filter the 58 Å telescope, since Zr attenuates 58 Å. Superimposed on the filter spectra are the strengths of the central lines in the MSSTA bandpasses, and of the 304 Å line that can contaminate some multilayer images if not filtered.

60

2.3.4   ANALYTICAL METHOD FOR MSSTA FILTER DESIGN

Given the materials, designing the filters is a matter of optimizing the in-band transmission while satisfying constraints on the exclusion of out-of-band light. These constraints can be expressed as the filter's required relative density:

$$\text{(Equation 10)} \quad D_{Vis} = \log\left(\frac{T_{EUV}}{T_{Vis}}\right) = \log\left(\frac{\Phi_{EUV}}{\Phi_{Vis}}\right) + \log\left(\frac{R_{EUV}}{R_{Vis}}\right) + \log\left(\frac{f_{EUV}}{f_{Vis}}\right) - \log\left(\frac{\varepsilon_{EUV}}{\varepsilon_{Vis}}\right)$$

where T is the transmission of the filter, Φ is the total solar flux, R is the reflectivity of the multilayer mirror (squared for two-mirror systems), f is the relative efficiency of the film, and ε is the relative exposure desired in the final image. The *Vis* subscript denotes an effective value of the quantity in question at visible wavelengths, and can be thought of as an integral or average over visible wavelengths as appropriate. A similar expression can be written for D_{304}, the requirement that the filter exclude He II 304 Å radiation, by substituting 304 Å for visible light in the denominator of each factor.

Central λ	Flux in Central Line		Reflectivity		Film Response	Exposure Ratio	Relative Density	
	$\log\left(\frac{\Phi_{EUV}}{\Phi_{Vis}}\right)$	$\log\left(\frac{\Phi_{EUV}}{\Phi_{304}}\right)$	$\log\left(\frac{R_{EUV}}{R_{Vis}}\right)$	$\log\left(\frac{R_{EUV}}{R_{304}}\right)$	$\log\left(\frac{f_{EUV}}{f_{Vis}}\right)$	$\log\left(\frac{\varepsilon_{EUV}}{\varepsilon_{Vis/304}}\right)$	D_{Vis}	$D304$
58 Å	-8.5	-2.3	-1.7	0.3			-15.2	-4.0
98 Å	-8.7	-2.5	-0.3	1.7			-13.9	-2.7
131 Å	-8.8	-2.6	0.2	2.2			-13.7	-2.5
150 Å	-8.7	-2.5	-0.1	1.9			-13.7	-2.5
171 Å	-7.4	-1.2	0.0	2.0	-3	2	-12.5	-1.3
180 Å	-7.4	-1.2	-0.1	1.9			-12.4	-1.2
195 Å	-7.4	-1.2	-0.3	1.7			-12.8	-1.6
211 Å	-7.6	-1.4	-0.4	1.6			-12.9	-1.7
256 Å	-7.5	-1.3	-0.8	1.2			-13.3	-2.1

Table 4. Relative density specifications for the MSSTA III filters (see Equation 10). Note that the film response factor is only used to find visible light relative density.

We can deal with each of these factors in turn, as summarized in Table 4. The flux values for the EUV lines in the MSSTA bandpasses are drawn from Malinovsky and Heroux (Malinovsky and Heroux 1973); only the single strongest line in each bandpass is used, leading to conservative underestimates (by a factor of 2-3 in most cases) of the EUV flux. The 304 Å flux is from Judge *et al.* (Judge, McMullin et al. 1999). Reflectivity is the measured value for each multilayer for the EUV lines; visible light reflectivity is assumed to be ~50% from each multilayer, and 304 Å reflectivity is taken to be 5% (based on synchrotron measurements of the MSSTA II telescopes by Allen *et al.* (Allen, Willis et al. 1991)). Film response is treated in more detail later; for the purpose of this calculation we compared the exposure (in ergs/cm^2) required to produce a unit density above the fog (i.e. a spot that transmits 10% as much light as a clear portion of the film) at EUV and visible wavelengths. Hoover *et al.* (Hoover, Walker et al. 1990) found that ~100 ergs/cm^{-2} of EUV light are required, while Kodak (Dancy and Buckley 1987) found that T-Max 100, which has similar visible-light responsivity to XUV-100, reaches the specified density under only 0.1 ergs/cm^{-2} of exposure to visible light. Film response is not included in the 304 Å calculation.

The value of relative exposure ε indicates that the filters are designed to ensure that EUV light accounts for ~100 times as much exposure in the final image as visible light. In practice, the value is higher, as all the values used in Equation 10 are conservative and err on the side of excluding more out-of-band light (at the cost of reduced in-band throughput). Typical values of these factors are as follows:

$$\log\left(\frac{\Phi_{EUV}}{\Phi_{Vis}}\right) \sim -8;$$

$$\log\left(\frac{R_{EUV}}{R_{Vis}}\right) \sim 0;$$

$$\log\left(\frac{f_{EUV}}{f_{Vis}}\right) \sim -3$$

$$\log\left(\frac{\varepsilon_{EUV}}{\varepsilon_{Vis}}\right) = 2$$

Once D_{vis} and D_{304} have been specified for each filter, the thickness of the filters can be found. For the single-material filters (pure Zr on the 98, 131 and 150 Å telescopes, and pure Nb on the 58 Å telescope) this is a simple matter; substituting Equation 9 into Equation 10, we have

$$D_{Vis} = \log\left(\frac{T_{EUV}}{T_{Vis}}\right) = \log\left(\frac{e^{-d\mu(EUV)}}{e^{-d\mu(Vis)}}\right) = \log\left(e^{-d(\mu(EUV)-\mu(Vis))}\right)$$
$$= -d\ln(10)(\mu(EUV) - \mu(Vis))$$

The difference in the absorption coefficient μ [Å^{-1}] of the material in- and out-of-band is divided into the required relative density to give the required filter thickness in Å. The thicknesses required to achieve the necessary D_{vis} and D_{304} specifications are found, and the greater thickness is used (because Zr and Nb strongly reject 304 Å light, the visible light rejection limited the thickness of all the single-valued filters).

For the aluminum/zirconium filters used on all the telescopes centered at wavelengths over 170 Å, it is a slightly more complicated constrained optimization problem: the two parameters (Zr thickness and Al thickness) are varied to satisfy the two constraints (D_{vis} and D_{304}) while maximizing the in-band transmission. This problem can be solved numerically; the calculations were performed by Jordan Alexander of Luxel.

From a practical standpoint, filter thicknesses can be manufactured to within 10% error, and the specified relative densities are conservative and imprecise; therefore, they were rounded to produce target thicknesses for each filter. After manufacture, Luxel reports the thickness of each filter to a tolerance of ±50 Å. Using these values, and the known absorption coefficients of the materials, combined with the transmission of the 70 lpi nickel mesh supporting each filter (a geometrical factor ranging from 79.0% - 84.0%), we can calculate the predicted transmission of each filter as a function of wavelength in the EUV bandpass, as well as the relative density at 304 Å and to visible light.

The thickness and in-band transmission of the filter used on each of the MSSTA III telescopes are presented in Table 5. The bandpasses of these filters are presented in Figure 24.

Central Wavelength	Filter	Transmission at Central Wavelength
58 Å	4306 Å Nb	0.09
98 Å	3880 Å Zr	0.28
131 Å	3880 Å Zr	0.29
150 Å	4100 Å Zr	0.18
171 Å	1811 Å Al + 634 Å Zr	0.43
180 Å	1811 Å Al + 634 Å Zr	0.40
195 Å	2050 Å Al + 718 Å Zr	0.31
211 Å	2050 Å Al + 718 Å Zr	0.21
256 Å	2050 Å Al + 718 Å Zr	0.03

Table 5. Description of the filters used on the MSSTA III EUV telescopes.
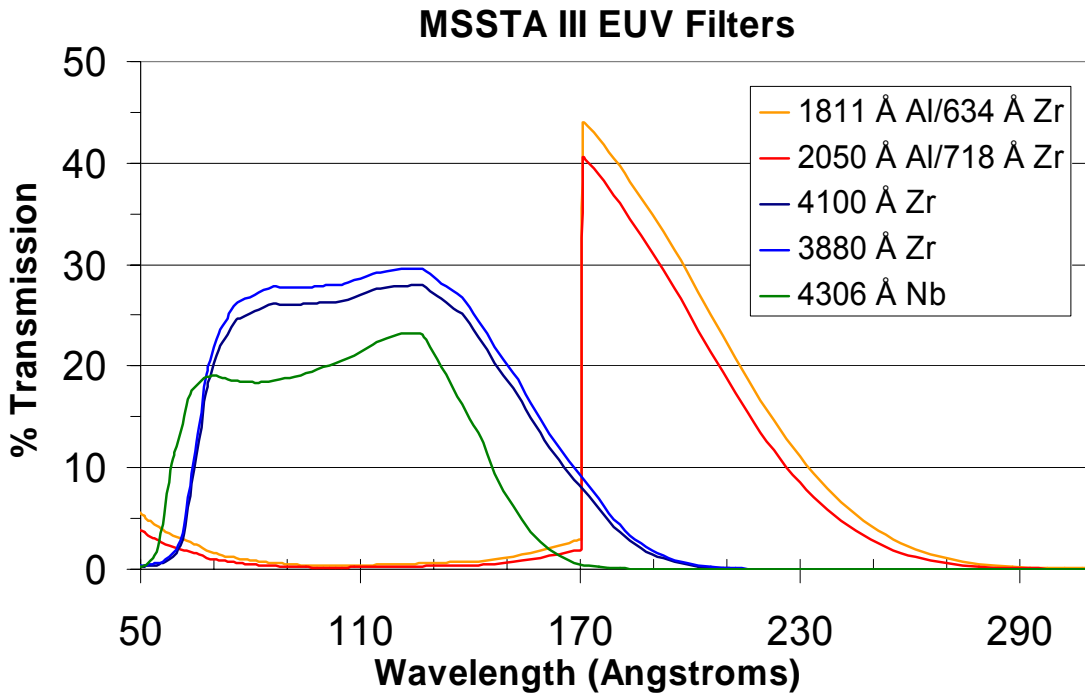
Figure 24. Transmission of the filters used on the MSSTA III. These are values calculated based on the material properties measured by Henke *et al.*, and are the values that were used to generate the temperature kernels for the MSSTA telescopes.

2.3.5   CALIBRATION OF EUV FILTERS

Unlike the multilayer mirrors, the filters were not measured at a synchrotron source to verify their in-band transmission characteristics prior to flight. While single-point transmission measurements are quite straightforward on ALS beamline 6.3.2, there were several reasons why the MSSTA III filters were not tested:

- The filters are extremely thin and delicate, and can be destroyed by any kind of rough handling (despite reasonable precautions, one backup filter was found to have developed pinholes, and, during the process of mounting the filters in the telescopes before flight, two flight filters were destroyed). Therefore, we wanted to minimize their exposure to damage.

- The integrity of the filter is a major variable in determining its performance; the presence of minute pinholes or thickness variations over the surface of an individual filter can be expected to affect its overall transmission more than deviation from quoted average thickness during production. Therefore, measuring a single filter at a single point would not be substantially more accurate than simply accepting the calculated values of the filter transmission. It would be necessary to measure the transmission of each filter over its whole area, which is impractical.

In generating the instrument bandpasses, we used the predicted filter transmission values presented in Figure 24 above.

The accuracy of these values can be compromised by deviations in average filter thickness from specified values (though Luxel gives a tolerance of ±50 Å, or about 2%, on the filter thickness after manufacture), oxidation or impurities in the filter materials, or the development of pinholes. We can estimate the accuracy of our filter transmission values by looking at the results of previous efforts to calibrate Luxel thin-foil filters.

The filters for the MSSTA I flight were measured at SSRL beamline 1-2 by Allen et al (Allen, Willis et al. 1991), 1-2 years after the flight. They found transmission values scattered widely around the predicted values (±50% RMS error). Similar results were obtained when Plummer et al. measured the filters for the MSSTA II flight (Plummer, DeForest et al. 1994). While these

large errors are discouraging, both sets of measurements were plagued by complications. In addition to the challenges mentioned above (the risk of damage to the filters, and the sensitivity of synchrotron measurements to pinholes or local variations in the filter thickness), the synchrotron beamline used was contaminated by up to 30% higher-order light, and the experimental chamber was not optimized for transmission measurements and had to be reconfigured in the middle of each run. Therefore, it is not unreasonable to suggest that the measured values are less trustworthy than the calculated values.

An elegant filter calibration was performed in flight by the TRACE instrument on its two Luxel-made thin-foil aluminum focal plane filters (Handy, Acton et al. 1999). By observing a given solar structure through both filters, then through only one, then the other, they were able to measure the average transmission over the TRACE multilayer bandpasses of each filter. The transmissions measured in this way at 171 Å and 195 Å agreed to ~8% with the predicted values. Based on this agreement, we conservatively estimate that the predicted filter transmission values used to generate the MSSTA III instrument bandpasses are accurate to 10%.

2.3.6   FILTER FAILURE

An issue that was not adequately addressed during the design of the MSSTA III filters was their ability to withstand the concentrated solar flux. Because of the success of past MSSTA flights using similar filters, and the experience of the Luxel Corporation in filter manufacture, a detailed analysis of the heat load deposited on the filters was not carried out prior to flight, despite the fact that neither Zr nor Nb had been used for solar observations before. This was a critical oversight, and proved quite costly: three of the filters were melted as soon as they were exposed to concentrated sunlight.

Table 6 shows the approximate heat load on each filter, and summarizes their performance in flight. The danger of using focal-plane filters placed <10 cm in front of the film, rather than entrance filters, is evident, as is the risk of using untested materials. Figure 25 shows one of the destroyed filters. The filter failure occurred almost instantaneously upon the payload acquiring

the sun; all the frames of film shot through damaged filters, including the first, very short exposures, are fully exposed and have roughly sun-sized holes burned through them.

Central Wavelength	Telescope Aperture and Design	Approx. Solar Flux Density at Filter (Solar Constants)	Filter Type	Result
58 Å	100mm f/15 Herschelian	27	Nb	Melted
98 Å	100mm f/15 Herschelian	27	Zr	Melted
131 Å	127mm f/8 Herschelian	95	Zr	Melted
150 Å	127mm f/28 Ritchey-Chrétien	4	Zr	OK
171 Å	63.5mm f/31 Ritchey-Chrétien	3	Al/Zr	OK
180 Å	63.5mm f/31 Ritchey-Chrétien	3	Al/Zr	OK
195 Å	127mm f/28 Ritchey-Chrétien	4	Al/Zr	OK
211 Å	127mm f/28 Ritchey-Chrétien	4	Al/Zr	OK
256 Å	127mm f/28 Ritchey-Chrétien	4	Al/Zr	OK

Table 6. Concentration of solar flux on the MSSTA III EUV filters, and the result
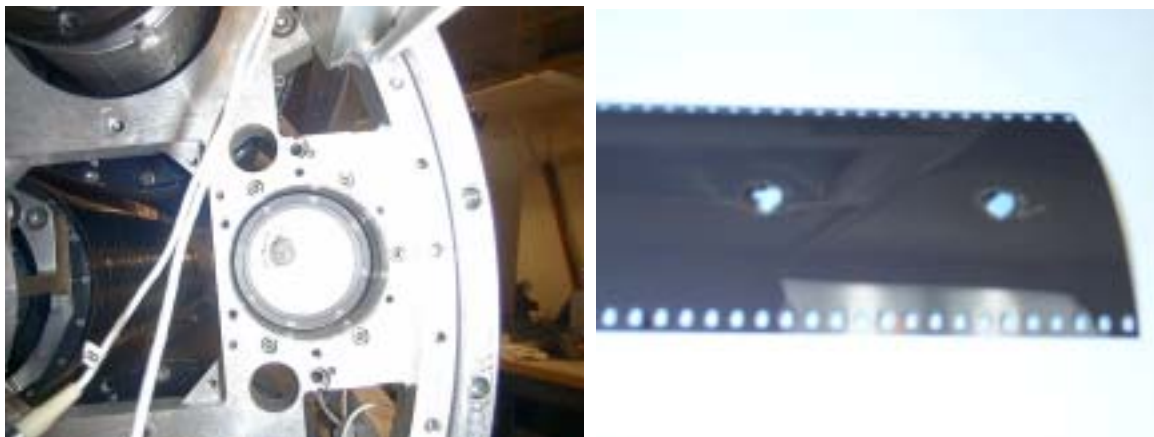
Figure 25. a) The 131 Å Zr filter after the flight; b) two frames of film from the 131 Å camera after the flight, showing very overexposed solar images

A few points are noteworthy:

- All of the relatively fast Herschelian telescopes (f/15 or faster) destroyed their filters, while none of the Ritchey-Chrétien telescopes (slower than f/25) did. However, the MSSTA has obtained EUV images with f/8 Herschelians in the past, using Al filters. Evidently, Al, with its superior reflectivity and thermal conductivity, is better able to handle the concentrated solar flux than Zr or Nb.

- While two of the pure Zr filters did fail rather spectacularly, the one on the much slower 150 Å Ritchey-Chrétien telescope performed well. Therefore, Zr has potential as a filter material, but must be used either as a prefilter or with a slow optic.

2.4 FUV optics

2.4.1 INTRODUCTION

Two of the 11 bandpasses studied by the MSSTA III – the 1216 Å Lyman α and 1550 Å C IV Ritchey-Chrétiens – lie in the wavelength regime generally referred to as far ultraviolet or FUV; the other nine are in the extreme ultraviolet (EUV). The distinction between EUV and FUV is important both in terms of how data are gathered in these regimes, and what they can tell us. The sun's FUV output is qualitatively and quantitatively quite different from both its EUV and its visible light output. While the solar EUV flux consists entirely of well-spaced emission lines from highly-ionized plasma at temperatures around 1,000,000 K, the solar FUV spectrum is characterized by numerous strong emission lines from neutral or barely-ionized atoms in the temperature range of 10,000 – 100,000 K. In addition to being much stronger than most EUV lines, these FUV lines are superimposed on continuum radiation from a variety of mechanisms, and therefore cannot be isolated without extremely narrowband (R ~ 1000) instruments. Table 7 describes some of the important observational and physical characteristics of the wavelength regimes explored by the MSSTA.

Like EUV, FUV is absorbed by the Earth's atmosphere, and must be observed from space. However, it behaves very differently in interactions with most materials. FUV photons are not energetic enough to penetrate the thin-foil filters or reflective multilayer stacks used by the MSSTA EUV telescopes, and thus imaging the sun in the FUV requires entirely different technologies. Fortunately, high-resolution FUV telescopes are a relatively well-developed technology; a number of techniques for constructing narrowband mirrors and filters in this regime have been proven effective, and have a longer history than the EUV telescopes that make up the bulk of the MSSTA payload (Foing, Bonnet et al. 1986).

	Visible	Far Ultraviolet (FUV)	Extreme Ultraviolet (EUV)	Soft X-Ray
Wavelength (Å)	3500-7500	1200-2000	50-300	1-50
Temperature of plasma responsible for solar emission	6000	10,000-100,000	100,000-5,000,000	5,000,000-30,000,000
"Layer" of the solar atmosphere where emitting plasma lies	Photosphere	Chromosphere/ Lower Transition Region	Upper Transition Region/Corona	Corona
Typical strength of emission lines (Log10, ergs cm-2 s-1 at the Earth's atmosphere)	N/A (continuum/ absorption lines)	-0.5	-2.0	-4.0
Typical strength of continuum (Log10, ergs cm-2 s-1 Å-1 at the Earth's atmosphere)	2.5	-1.5	-7.0	-6.5
Radiation can penetrate… Earth's atmosphere?	Yes	No	No	No
Radiation can penetrate… FUV filter substrate (4 mm MgF2)?	Yes	Yes	No	No
Radiation can penetrate… EUV thin-foil filter (2000 Å aluminum)?	No	No	Yes	Yes

Table 7. Comparison of the ultraviolet wavelength regimes of the solar spectrum. Various definitions for all of these regimes can be found; no effort has been made here to be comprehensive or authoritative, though the definitions given in this table are used throughout this work. Radiation between 300-1000 Å is also generally called EUV, but because it is not efficiently reflected by EUV multilayers or transmitted by thin-foil filters, from an experimental standpoint it constitutes a different wavelength regime from either the EUV or FUV as defined above.

The MSSTA I included a pair of FUV telescopes, their bandpasses centered on 1216 Å (H Ly α) and 1550 Å (C IV) emission lines. Narrowband FUV reflective filter coatings were applied to the same zerodur Ritchey-Chrétien mirror substrates, figured and flow-polished by Baker Consulting, that were used for the MSSTA I EUV telescopes (see section 2.1.2). These were supplemented by two transmission filters each, consisting of 2" diameter MgF_2 windows with narrowband FUV

metal-dielectric coatings deposited on the front face. Both the mirrors and filters were coated by Acton Research Corporation of Acton, Massachusetts.

For the MSSTA II, the 1550 Å telescope was re-flown, and another 1216 Å telescope with the same aperture but slightly shorter tube and faster mirrors was used. This short Ritchey-Chrétien Lyman α telescope used only one of the two 1216 Å filters, in order to allow faster exposure times.

The MSSTA III payload used the 1550 Å telescope and the short 1216 Å telescope (reconfigured to hold both transmission filters). Both sets of optics were originally fabricated in 1989 and had been flown successfully on previous MSSTA experiments. In February of 2001, we attempted to re-calibrate the FUV optics at beamline 8.1 at SSRL. However, this bending magnet beamline is designed for higher-energy radiation (10-200 eV, or ~60-1200 Å, according to its specifications). The beamline output in the FUV is quite low, and 50% or more of what flux there is consists of higher-order radiation. Efforts to attenuate the higher-order light with MgF_2 filters proved unsatisfactory, and eventually we abandoned the project and returned the optics to Acton research for measurement on their vacuum spectrophotometer system (Callahan and Flint 1999).

Because of the cost, risk and inconvenience of disassembling the FUV telescopes and sending their mirrors to Acton for measurement, we only had the transmission filters measured. For the mirrors, we have only the reflectivity measurement that was supplied in 1989 when the mirrors were originally coated for the MSSTA I flight. While the reflective coatings are somewhat soft and vulnerable to damage, there is no reason to believe that they should degrade spontaneously if kept in a clean environment and not exposed to energetic radiation for prolonged periods. The MSSTA FUV telescope mirrors are relatively old, but they have lived fairly sheltered lives; the surfaces have never been cleaned, and they were stored in shrink-wrap in between flights. Their only exposure to UV has come during flight (when the vacuum of space should have prevented them from accumulating contaminants). Therefore, the 1989 measurements should provide a reasonable estimate of the mirrors' performance. A summary of the calibration measurements used to generate the instrument bandpasses is provided in Table 8.

Optic	Peak Efficiency (%)	FWHM (Å)	Date Measured
1216 Å mirror coating	51	200	5/2/1989
1550 Å mirror coating	79	340	5/2/1989
1216 Å filter 1	8	50	4/18/2001
1216 Å filter 2	15	120	4/18/2001
1550 Å filter 1	16	290	4/18/2001
1550 Å filter 2	16	240	4/18/2001
1550 Å filter 3	13	200	4/18/2001
1216 Å Composite Bandpass	0.26	50	
1550 Å Composite Bandpass	1.53	150	

Table 8. Summary of the efficiency (reflectivity or transmission) measurements of the MSSTA III FUV optics. The 1550 Å filter 3 was not used in flight. The narrowband reflective coatings on the two Ritchey-Chrétien mirrors of each telescope were last measured prior to the MSSTA I flight. It is possible that their FUV performance has degraded over time; this uncertainty dominates the error in the final composite bandpasses.

The efficiency of the mirrors and filters at visible wavelengths was not measured. However, Acton supplies typical reflectivity curves for the mirrors which show efficiency ranging from 2-10% across the visible portion of the spectrum. Alignment tests of the telescopes using visible light qualitatively confirm this estimate, as the mirrors produce only a faint, deep red image of a white-light target. The filter specifications include visible light transmission of 10^{-4}; this was not confirmed experimentally. If the coatings were damaged and pinholes formed, their visible light rejection could have been compromised. However, even allowing for some degradation, using the specified values for the mirrors and filters gives a visible light relative density (see section 2.3.4) that is more than adequate to ensure that the image is free of white-light contamination.

The contribution of various types of radiation (primary emission line, FUV continuum, and visible light) to the image produced by the FUV telescopes is discussed in detail in section 2.6.3. The telescope bandpasses used for this analysis, based on the measurements taken by Acton research as described above, are presented in Figure 26.

FUV Telescope Bandpasses
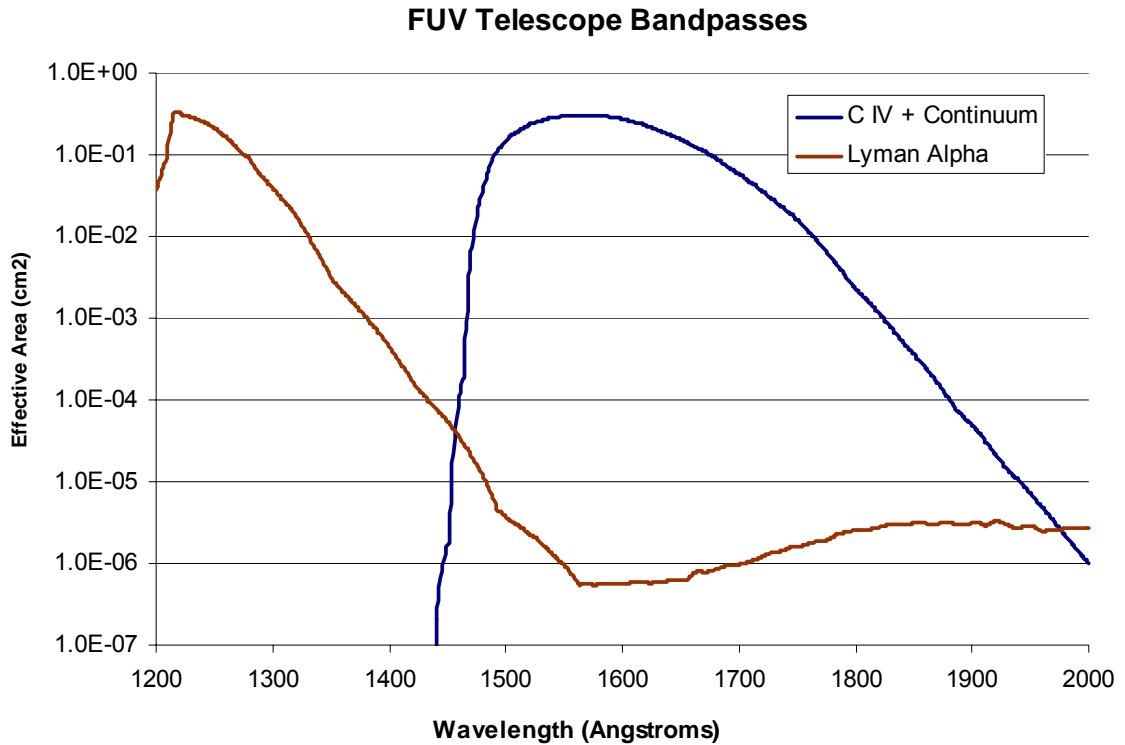
Figure 26. Effective area of the MSSTA III FUV telescopes (geometrical collecting area times efficiency of the two mirrors and two filters). Visible light rejection was not measured, but manufacturer's specifications on the mirrors and filters suggest that each telescope has a visible-light effective area less than 10^{-8} cm^2.

2.4.2 ERROR ESTIMATES

All mirror and filter calibrations were conducted by making a single measurement at a single point on the optic in question, so we do not have sufficient data to estimate the errors of those calibrations. However, measuring optics with a vacuum spectrophotometer is relatively straightforward and measurement error is generally quite small. Because of the less-stringent demands on surface smoothness and layer spacing, point-to-point variation on the optics is also

less likely to be an issue with FUV optics than with the EUV multilayers. The main uncertainty comes from the possibility of degradation in the mirror coatings since they were last measured. Based on the stability of the filter bandpasses over this same interval, we can estimate that the mirror bandpasses did not change by more than ~10%. Therefore, we can draw the following conclusions about the accuracy of the FUV mirror and filter calibration:

- For the purpose of deriving absolute fluxes from MSSTA III FUV images, the errors in the FUV mirror and filter calibration are small enough to be insignificant compared to the uncertainties involved in the energy calibration of the photographic film. Indeed, as discussed in section 2.5.3, the film was entirely uncalibrated at FUV wavelengths. Cross-calibration using known total irradiance values is possible; however, the error associated with fluences derived with this technique is entirely dominated by the uncertainty of the comparison, without any additional contribution from the mirror and filter efficiencies.

- For the purpose of estimating the contribution of various sources of solar emission to the final FUV image, the uncertainty in the shape of the bandpass derived from the mirror and filter measurements is sufficiently small that the conclusions drawn from the bandpass analysis in section 2.6.3 will be qualitatively correct.

2.5 Film

2.5.1   INTRODUCTION

The MSSTA III may represent the last time that photographic emulsions were used for a space-based astronomical imaging application. As such, it represents the end of an era of productive and exciting research. The emulsions it carried – XUV-100 and Spectroscopic 649, both manufactured by Kodak – are extremely advanced compared to the films used by early space missions, and offer superior sensitivity, spatial resolution, and exposure latitude. Only the availability of these films made it possible to fly 11 fully independent telescopes, each capable of imaging the solar disk and lower corona with arc-second scale resolution.

However, the end of the film era is welcome in many ways. CCDs now provide substantially better response to light across the x-ray and ultraviolet spectrum, and are much easier to characterize and use. Photometric calibration of the MSSTA III film required extensive experimental effort, and the uncertainties and complications resulting from the process remain the largest source of error in the interpretation of the MSSTA images. In this section, the film calibration is described, and the resulting errors are analyzed.

Photography in the EUV

Photographic film consists of a flexible backing covered with an emulsion in which silver halide grains are suspended (Figure 27). When these grains absorb sufficient energy from incident photons, they become "activated" (partially ionized). The development process then renders the activated grains to metallic silver, darkening the film. The optical density of an area of the developed film is proportional to the amount of light that reached that area (the time-integrated flux, or fluence: $\Phi = \int \phi \mathrm{d}t$, generally in ergs cm^{-2}).
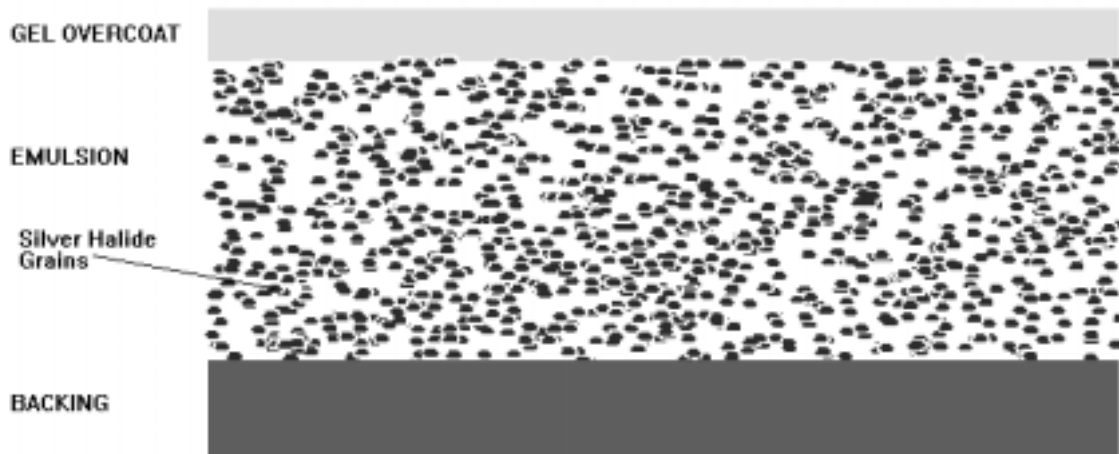
Figure 27. Photographic film consists of light-sensitive silver halide crystals embedded in an emulsion, protected by a gelatin overcoat.

Because the density on the negative is due to the pattern of discrete silver grains, there is a fundamental trade-off between spatial resolution and sensitivity to low light levels. Choosing a film requires making a compromise between very fast film with large grains and poor spatial resolution, or a slower film with finer imaging capabilities.

The basic description given above is sufficient to understand how conventional film operates in everyday use, but it glosses over a number of complications that become significant when the film is used as the detector for an EUV telescope:

- **Absorption in the Overcoat:** Over the emulsion is a gelatin coating which protects the emulsion from scratches and prevents it from drying out. The gel overcoat also tends to prevent UV photons from reaching the emulsion, which is why most films are insensitive to the wavelengths studied by the MSSTA III.

- **Drying/Sparking in Vacuum:** When transported through the camera in vacuum, the emulsion dries out rapidly despite the gel overcoat. The dry emulsion is susceptible to cracks

that appear as long lines across the negative, and to static discharge that partially exposes the film and produces a background fog.

- **Energetic Photons:** At visible wavelengths, each grain can absorb a large number of photons before becoming fully activated. Light is attenuated as it passes through the emulsion, and the film acts like an energy detector. However, when the incident photons are energetic enough to fully activate a grain individually, the film response is qualitatively different. It acts like a photon counter, and the signal is dominated by scattering statistics. The EUV wavelengths studied by the MSSTA III lie on the border of these two regimes.

An additional set of complications is raised by the fact that the intensity of the radiation reaching the film plane of the MSSTA telescopes is much lower than what conventional film is designed to image:

- **Reciprocity Failure:** Partially-activated silver halide grains can be spontaneously neutralized by electrons in the crystal if their activation is not quickly reinforced by more photons. Thus, at very low incident intensity levels, the activation process is highly inefficient. The reciprocity law, which holds that film density is determined simply by the total fluence, independent of the intensity (the rate at which that fluence is deposited), is not entirely valid under these conditions.

- **Harsh Developer:** The aggressive developing processes demanded by the low exposure values of the MSSTA images result in increased granularity on the negative, dramatically lowering the film's signal-to-noise ratio at small spatial scales.

These considerations dictate our choice of film and developing procedures. Previous MSSTA teams have conducted extensive studies on the suitability of various films for flight [(Hoover, Walker et al. 1991), (Hoover, Walker et al. 1991)], settling on two specialized emulsions from Kodak. XUV-100 is a tabular grain film similar to Kodak's consumer T-Max 100. It uses a specially-formulated overcoating that makes it orders of magnitude more sensitive to EUV light than conventional black-and-white film. Spectroscopic 649 (S-649), which was developed for

scientific applications, is an extremely high-resolution emulsion; it has a relatively thin coating that does not substantially reduce its efficiency in the EUV. Both films use a conductive ESTAR base that reduces static discharge under vacuum.

The properties of these films are summarized in Table 9. Alternative emulsions from Kodak and Agfa were studied, but none offered compelling advantages over these two. Both have been used in previous MSSTA flights, with good results.

Film	Resolution (lp/mm)	Visible speed (ASA)	Base
XUV-100	200	100	Conductive ESTAR
Spectroscopic 649	2000	0.002	Conductive ESTAR
Technical Pan	320	64	ESTAR-AH
SO-253	1250	1	ESTAR-AS

Table 9. Properties of the two photographic films used by the MSSTA, Kodak XUV-100 and Spectroscopic 649. Also included for comparison purposes is Kodak Technical Pan, a consumer film that is widely used for astronomical photography, and SO-253, the holographic film that was used for alignment testing.

The resolution listed in Table 9 for each emulsion is an approximate value based on MTF curves supplied by Kodak. Resolution is strongly affected by the developing process (and may depend on the wavelength of the exposing photons as well), and the harsh developers used by the MSSTA generally do not allow the emulsions to achieve the specified resolution. This effect is discussed further in section 2.5.4.

With scientific photography falling out of favor, the specialized emulsions used for high-resolution x-ray imaging are no longer manufactured. We were forced to rely on the remaining stock of XUV-100 and S-649 left over from the earlier MSSTA flights. These batches were originally produced in 1991; though they had been sealed and stored in a freezer since then, an overall increase in granularity and base fog density, and a decrease in sensitivity, should be expected as a result of this long storage.

The shortage of XUV-100 and S-649 was so severe that we became concerned we might not have enough for all the payload telescopes. To reduce the risk of running out of flight film, we refrained from using them for pre-flight resolution testing of the telescopes. Instead, a fine-grained holographic SO-253 film was used. Furthermore, we decided to use commercially-available Kodak Technical Pan emulsion on the 256 Å telescope, after that instrument was added to the payload, in order to save the specialized flight film for the other telescopes (this decision is described in more detail below).

Film Calibration

In order to conduct quantitative study using a MSSTA spectroheliograms, it is necessary to convert film density to physical units describing the absolute intensity of the radiation from the imaged plasma. This means performing experiments where the film is exposed with a known fluence at the wavelength of interest, then developed in a carefully-controlled process identical to the one used on the flight film. The resulting density is measured and a transfer function (fluence as a function of density) can be derived by inverting the results. Such experiments were performed prior to past MSSTA launches (Hoover, Walker et al. 1994).

However, despite the wealth of calibration data and the quality of the images obtained in these flights, the utility of the data has always been limited by uncertainty in the film calibration. The primary source of this uncertainty has been the inconsistent developing practice used on the flight film. For the first two flights, each camera carried a variety of different emulsions, spliced together in several places. The flight negatives were developed using a wide variety of processes, most of which were different from the ones used on the calibration film (and which, in the worst cases, were not even recorded, making it impossible to calibrate the process after the flight).

Using uncalibrated processes was deemed necessary because the ability of the telescopes to record high-contrast images was unproven; it was thought that employing a wide variety of processes would ensure at least some usable data. However, when the flight negatives were being reduced, it was discovered that the calibration was either entirely unknown, or was obviously

faulty (because it resulted in flux measurements that differed by orders of magnitude from accepted mean values) (Kankelborg 1996). Cross-calibrating the images with each other or with data from other instruments made some quantitative analysis possible [(Allen, Oluseyi et al. 1997), (Kankelborg, Walker et al. 1997)]. Still, reliance on cross-calibration defeats the purpose of the carefully measuring the optics, and undermines one of the primary goals of the MSSTA mission.

In order to avoid these inconsistencies, we decided that each MSSTA III telescope would carry only a single type of film, and that all film of a given type would be developed with the same process. Previous film measurements provided invaluable guidelines for choosing the appropriate film for each telescope, and the appropriate development process for each film. However, the film calibration work described in (Hoover, Walker et al. 1991) and elsewhere could not be completely relied upon. The degradation in the film response after eight years in a freezer had to be accounted for; also, some of the earlier calibration results were called into question when their application to flight images resulted in unphysical solar flux values. Finally, it is evident from MSSTA I and II flight film that the granularity of the XUV-100 in any of the tested development processes is substantially worse than the specified value of 200 lp/mm, and limits the telescope's image quality. This led to the conclusion that better data could be obtained by using a new, gentler process, or using the S-649 emulsion in place of the XUV-100. Therefore, in order to identify the optimal emulsion and process for each telescope, and to obtain accurate quantitative measurements from the resulting data, it was necessary to perform a new set of film calibration experiments.
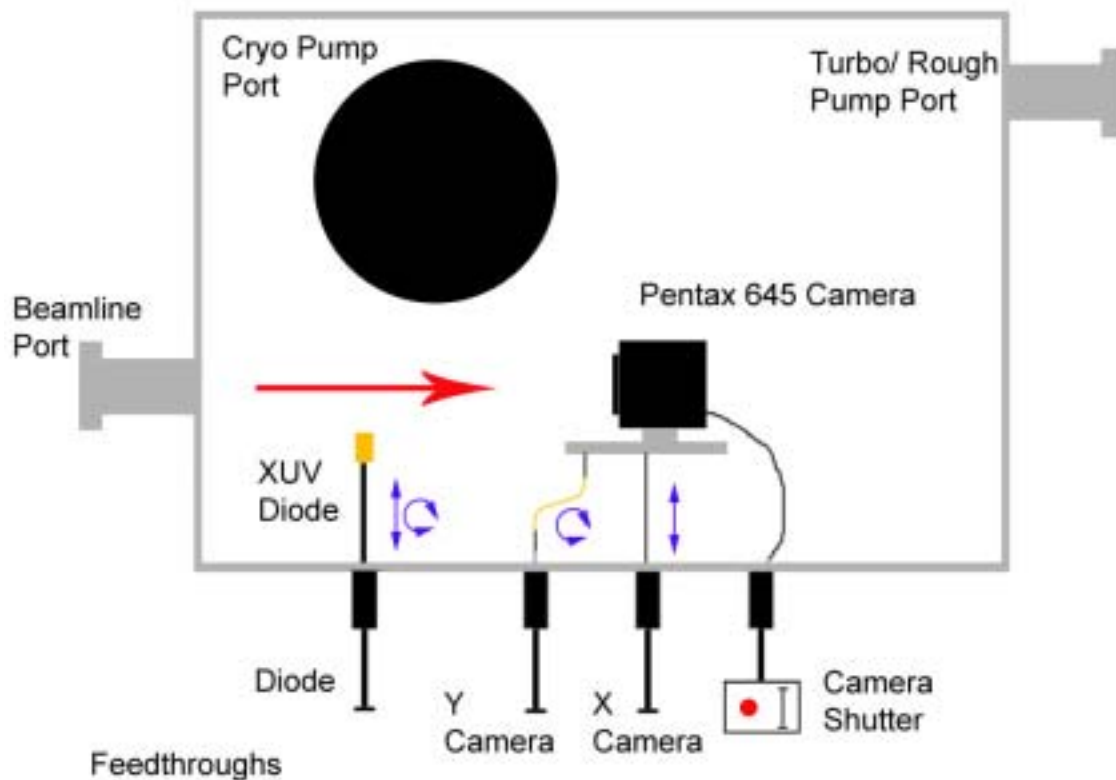
2.5.2   CALIBRATION MEASUREMENTS

The EUV film calibration experiments were performed between February 7 and March 20 of 2000 on Beamline 8-1 at the Stanford Synchrotron Radiation Laboratory (SSRL). This is a bending magnet beamline using a toroidal grating monochromator to deliver ultraviolet light between 10 – 200 eV (60 – 1200 Å) (Tirsell and Karpenko 1990). Because of the wide variety of experiments carried out on this beamline, there is no permanent experimental end station; instead, we supplied our own vacuum chamber, configured for testing the response of photographic emulsions.

The test chamber is shown schematically in Figure 28. It was designed to use the standard Pentax 645 cameras that are flown on the MSSTA. These cameras are fundamentally incompatible with the demands of a UHV beamline. While they were cleaned and lubricated with vacuum grease, they still contain countless virtual leaks and outgassing materials; indeed, the photographic emulsion itself outgases considerably. Despite the high-capacity cryopump attached to the chamber and the use of auxiliary turbopumps, pressure in the camera chamber never got below 10^{-5} torr, while the upstream segments of the beamline require pressure below 10^{-9} torr. SSRL supplied us with a differential pumping station (Warburton and Pianetta 1990) which helped support this pressure gradient. Still, the calibration measurements were fraught with difficulties stemming from the chamber and beamline vacuum systems. However, vacuum-related issues did not hamper the accuracy of the measurements, so these problems and their solutions will not be discussed here. The procedure used in the calibration measurements is summarized below.

The camera was loaded with a batch of 70mm film for testing, and the chamber was sealed and evacuated. Once the pressure dropped below 5×10^{-5} torr, the gate valve to the differential pump was opened, allowing the synchrotron beam into the chamber. With the monochromator set to pass 0-order (white) light, the beam was roughly aligned with the experimental apparatus. Then the monochromator was set for the desired EUV wavelength, and the appropriate order-suppressing pre-filter (generally aluminum on a nickel mesh for wavelengths > 171 Å; silicon or boron for shorter wavelengths) was inserted into the beamline.

The intensity of the EUV beam was measured using an absolutely-calibrated x-ray photodiode. The reading was corrected for dark current and background light by taking another reading with the beam shuttered. The photodiode was then pulled out of the path of the beam, allowing it to reach the camera.

Figure 28. Schematic top view of the experimental chamber used for film calibration measurements at SSRL.

The camera was operated through a set of vacuum feedthroughs that enabled us to position it in two axes perpendicular to the synchrotron beam. The shutter was controlled by an BNC feedthrough connected to a circuit that commanded exposures from 1/64 s to 4096 s. The camera's film advance mechanism was disabled via another feed-through, so that, by moving the camera in between exposures, were able to obtain up to nine exposures of different duration on a single negative before advancing the frame.

Generally, two frames (~18 exposures) would be taken at a given EUV wavelength, providing a sufficient variation in fluence to characterize the film's response at that wavelength. We then reinserted the photodiode to the beam path and took another calibrated measurement of the incident intensity. The average of the "before" and "after" intensity measurements was used in the analysis of the negatives. It would have been preferable to be able to sample the beam intensity simultaneously with exposing the film; unfortunately, no convenient mechanism for doing so was available. In general, the beam intensity varied by less than 5% between the before

and after measurements (primarily due to the exponential decay of the current in the synchrotron). This variation was ignored in the analysis.

After re-measuring the intensity, the monochromator was set to a new wavelength, and the "before" intensity of this wavelength was measured with the photodiode still in place. Then the diode was pulled aside and the exposure sequence was repeated. Up to 5 different wavelengths could be measured in this way on a single roll of film without breaking vacuum. Then chamber was vented, the film was removed from the camera and immediately developed in the SSRL darkroom.

A variety of chemical developers and development times were tested; however, we made an effort to hold all other parameters of the development process constant. Development was done in a JOBO film processor, which maintained the temperature of the negatives and all the chemistry at 20° C. It also agitated the negatives during development in order to ensure uniform processing. All negatives were fixed for 4-5 minutes using Kodak Rapid Film Fixer, rinsed with hypo-clearing agent, washed, and treated with Kodak photo-flo to prevent water spotting.

FILM	DEVELOPER	DEVELOPMENT TIME [minutes]	Number of Exposures at each Wavelength					
			58	98	150	173	193	211
Tech Pan	D-19	20	12					
Tech Pan	HC-110-1:9	8				14		
XUV-100	D-19	20				29		21
XUV-100	HC-110-1:9	15	9	18	18	18	17	
S-649	D-19	10	8	9	5	6	9	
S-649	Dektol	12	13	12	12	12	12	
S-649	HC-110-1:9	15	8	9	11	10	12	
S-649	HC-110-1:6	15		11	11	11	10	
S-649	HC-110-1:4	15	6	2	10	13	12	

Table 10. Films and processes calibrated at SSRL.

Table 10 lists the emulsions, development processes and wavelengths which were tested during this experiment. The data taken on Tech Pan were not analyzed in detail after our tests revealed a number of undesirable characteristics, including a tendency to fog heavily under vacuum. Qualitatively examining the negatives suggests that Tech Pan is slightly less sensitive than XUV-100 to EUV. Thus, it could be used as a backup to XUV-100, but is not the best choice for any of the MSSTA instruments.

Some of the choices concerning which films and developers to test turned out to be less than optimal. In particular, we emphasized testing of the S-649 film, at the expense of examining XUV-100's wavelength response more extensively. This proved to be a costly mistake when we determined that S-649 is unsuitable for use with the MSSTA telescopes at EUV wavelengths. Unfortunately, because the analysis of the measurements was performed after our synchrotron run had ended, we did not recognize this limitation in time to change our program. Furthermore, the challenges associated with getting a usable vacuum inside the experimental chamber consumed much of the time originally allocated to the experiment. Still, the data we did gather represents the best set of EUV measurements of high-resolution emulsions ever obtained.

We also attempted to use the beamline to test the film's response to FUV wavelengths studied by the MSSTA (1216 Å and 1550 Å). Unfortunately, the beamline's output in this regime is so low that higher order contamination completely dominates. Even when we attempted to exclude the higher orders by filtering the beam with MgF_2 windows, the flux of FUV photons was insufficient to expose the film or measure with the photodiode. We were unable to find an alternate FUV light source for film calibration. Therefore, the MSSTA FUV telescopes are essentially uncalibrated. It may be possible to cross-calibrate the images after flight, given accurate measurements of their bandpasses.

2.5.3   ANALYSIS OF CALIBRATION FILM

In general, photometric calibration of film aims to produce a "characteristic curve" such as the one shown in Figure 29. The characteristic curve gives film density, defined as defined as the Log_{10} of the transmission of the photographic negative, as a function of exposure (typically

measured in lux seconds). For a given type of film, this curve is sensitive to changes in the developing process, but certain qualitative features are common to the characteristic curves of most films. At low exposures, the film is unresponsive; there is a toe region where it "turns on" and begins to show the effect of increasing exposure, and a linear region over which density increases proportionally with exposure until the shoulder is reached and the film begins to saturate.

Once the characteristic curve has been measured, it can be inverted and modeled with a transfer function such as the one described by Green and McPeters (Green and Mcpeters 1975):

(Equation 11)
$$\Phi(D) = \Phi_0 \left\{ \frac{10^{(D-D_{min})} - 1}{1 - 10^{\beta(D-D_{max})}} \right\}^{\gamma}$$
[ergs cm^{-2}]

Here Φ is the fluence on an area of the film (in ergs cm^{-2}) and D is the density produced in that area. The best-fit parameters $\Phi_0, D_{min}, D_{max}, \gamma$ and β and can be found, and the transfer function is then applied to solar images whose density has been measured at each point. This procedure results in a calibrated solar image.
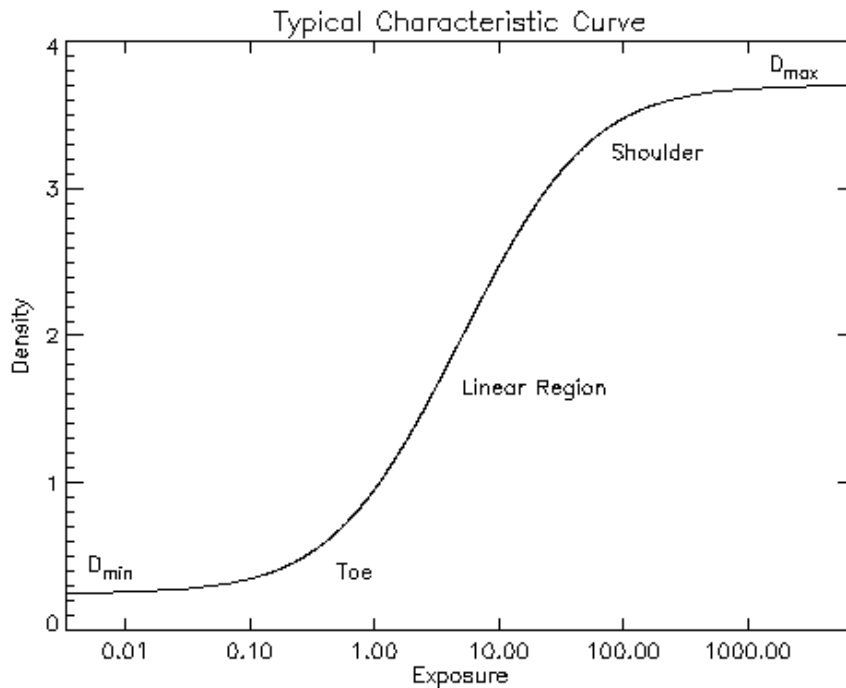
Figure 29. A typical characteristic curve describing the response of a given film and developing process.

Characteristic curves are generally provided by the film's manufacturer as a guideline for photographers. Indeed, Kodak has published curves for S-649 film (Dancy and Buckley 1987), though these measurements were made at visible light with development processes that are less extreme than those used for the MSSTA images, and thus are not usable by us. Previous solar rocket observatories, including the MSSTA, have measured and published characteristic curves for a variety of EUV films [(Hoover, Walker et al. 1994), (Golub, Nystrom et al. 1990)], and used their measurements to present calibrated data.

Unfortunately, constructing and interpreting characteristic curves is not as straightforward as it appears. Simply measuring a single point on the curve requires exposing an area of film to a reasonably uniform light of known intensity, so that the density in the area can be measured and plotted against the exposure. Calibration at EUV wavelengths requires illuminating the film with a synchrotron beam; the energetic beam generally cannot be shaped or diffused with conventional optics, and produces a spot that is highly non-uniform (see Figure 30). It is possible to measure the average density of the entire spot and plot this against the total energy contained in the beam. However, because the film is non-linear (particularly in the toe of its response curve), averaging the density in the spot is a rough approximation at best.
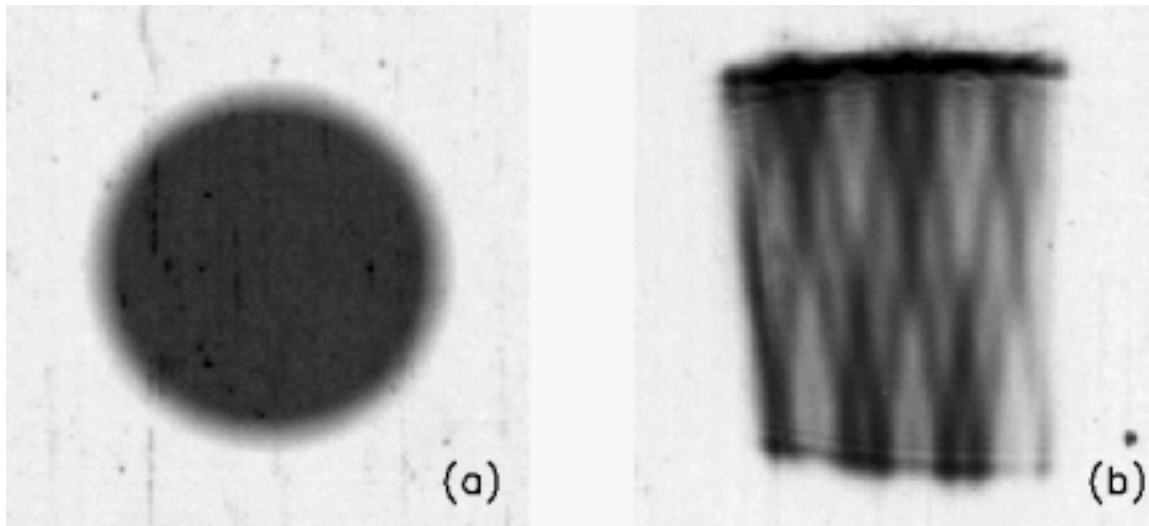
Figure 30. Generating a characteristic curve means exposing spots on the film with a known fluence and measuring the resulting density on the negative. At visible wavelengths (a), this is straightforward, as conventional optics can be used to smooth the beam cross-section and produce a uniform spot. However, at EUV wavelengths, the spot is produced by a synchrotron beam, and contains nonuniformities (especially the shadow of the order-suppressing filter) which are difficult to correct for (b). The spot in (a) is a synthetic image; b is a sample of actual data taken at SSRL.

An even more basic problem lies in the definition of film density. In order to apply a transfer function to a solar image, it is necessary to digitize the negative – that is, to generate an array of numbers $D(x, y)$ describing the density at each point on the negative. By convention, this is done with a scanning microdensitometer, which measures diffuse density at each point on the negative as shown in Figure 31. However, such systems are generally expensive and slow, and produce images with a lower spatial resolution and signal-to-noise ratio compared to conventional CCD-array-based film scanners. Film scanners, such as those used to digitize the MSSTA III negatives, assign pixel values to each point in the image by measuring a type of specular transmission (Figure 31). Converting scanner pixel values to diffuse density is not simply a matter of accounting for nonlinearities in the response of the scanner CCD; the scanner is measuring a fundamentally different quantity from diffuse density. The two measurements are strongly correlated, of course, but digitizing the same negative with a scanner and a microdensitometer (or even with two different scanners) and cross-correlating the results can produce considerable scatter, even if the signal-to-noise of each scan is quite high. Therefore, converting scanner pixel values to diffuse density before applying the transfer function effectively adds noise to the calibrated image.
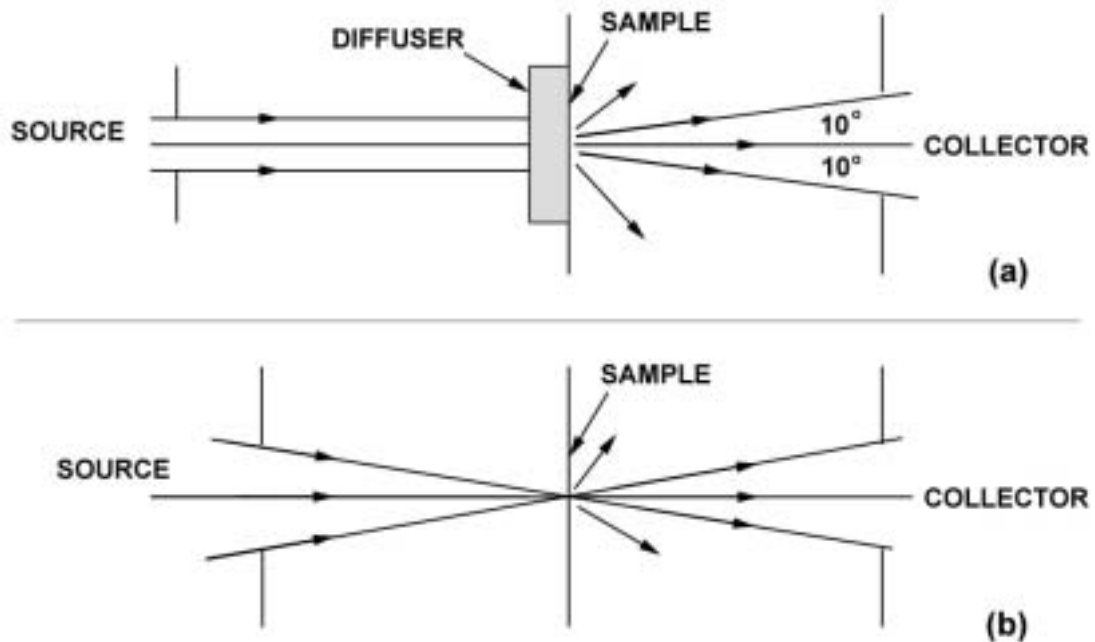
Figure 31. Density of a point in the image depends on how the negative is measured. Most calibration curves provide diffuse density, which must be measured as shown in (a). However, better image quality is obtained with a film scanner that measures some type of specular density, such as the one shown in (b). Adapted from (Dancy and Buckley 1987).

The solution is to implement a forward-fitting procedure that bypasses the step of converting a scanned spot image into a point on the diffuse density vs. fluence curve. In this procedure, a transfer function $\Phi(p)$ that converts pixel values to fluence is assumed. This function is then applied to all the pixels in a scanned image of a beam spot, and the resulting fluence values are summed to give the total energy deposited on the film in generating that spot. This energy can be compared with the known energy of the spot (determined from the photodiode measurements), and the parameters of the transfer function $\Phi(p)$ are varied to minimize the difference between the known and calculated energies of all the spots.

There are a few drawbacks to this approach, compared with the conventional technique of using the spots as points on a $D(\Phi)$ curve and then fitting to the inverted curve to find a transfer function $\Phi(D)$. The forward-fitting approach is considerably more computationally intensive, as the transfer function has to be applied to the entire digitized image at each iteration of the fit. It is also less intuitive; because the error at each point is determined after summing over thousands of pixels, it is not possible to say what effect changing the parameters will have on the error at a given point. Finally, the resulting transfer function will be specific to the scanner used in the calibration measurement, whereas diffuse density is a standardized quantity.

Nevertheless, the forward-fitting technique rests on fewer questionable assumptions than the conventional approach, and is more accurate and reliable. It is also easier to implement in the case where the same scanner is used for calibration and flight data. In the following section, the process is described in detail, and the final results of the film calibration are presented.

Fitting the Transfer Function

The calibration measurements taken at SSRL consist of a set of negatives exposed with images of the synchrotron beam. For a given type of film and development process f, a total of i spots were recorded at each of a number of different wavelengths λ. These spot images are digitized with a Umax PowerLook film scanner and saved as an array of pixel values. The photodiode readings taken before and after the exposure sequence are used to determine the intensity of the

88

synchrotron beam during the exposure. Thus, the data can be expressed as a pair of quantities describing each spot:

$p_{i,\lambda,f}(x,y)$ – image of the spot (pixel values at position [x,y] in the array)

$E_{i,\lambda,f}$ – the total energy that fell on the film to expose the spot image

The idea of the forward-fitting technique is to define a transfer function $\Phi_{\lambda,f}(p)$ and apply this to all the spot images to generate calibrated spot images $\Phi_{i,\lambda,f}$. The calibrated spot images are integrated over area to give

$$E'_{i,\lambda,f} = \int \Phi_{i,\lambda,f} \, \mathrm{d}x\mathrm{d}y \qquad \text{[ergs]}$$

the calculated total energy of the spot. The parameters of the transfer function are then varied to minimize the differences between the measured and calculated total energy values (E and E').

The first step is to define the basic form of the transfer function $\Phi(p)$. In addition to providing the ability to match the data, the function should reflect the underlying physics of the photographic process. Ideally, the affect of varying its parameters should be intuitively clear as well. The basic form of the Green and McPeters film model (Equation 11) can be adapted to give a pixel-to-fluence transfer function by realizing that density is related to the $-\log_{10}$ of the transmission of a point on the negative, and the pixel values are roughly proportional to transmission (and, therefore, high pixel values correspond to clear spots on the negative, or areas of relatively low fluence):

$$\Phi(p) = \Phi_0 \left\{ \frac{p_{max}/p - 1}{1 - \left(p_{min}/p\right)^{\beta}} \right\}^{\gamma} \qquad \text{[ergs cm}^{-2}\text{]}$$

It is generally best to take advantage of the linear region of the film's response; however, the MSSTA images are all recorded with the film operating around the toe of the curve (getting into the linear region would require either faster telescopes or faster film, both of which tend to decrease the spatial resolution of the images). Therefore, the parameters β (and p_{min}), which describe the shoulder of the characteristic curve, can be set to arbitrarily high (low) values, and the model becomes:

$$\text{(Equation 12)} \qquad\qquad \Phi(p) = \Phi_0 \left(\frac{p_{max}}{p} - 1 \right)^{\gamma} \qquad\qquad [\text{ergs cm}^{-2}]$$

Negative values of the quantity in parentheses are replaced with 0. This function is elegant and intuitive, and provides a reasonable fit to the data. The parameters are easily understood:

- p_{max} is the maximum pixel value, corresponding to the base fog density in unexposed areas of the film;

- γ is the exponent describing the contrast; and

- Φ_0 is the scale factor (specifically, the fluence that produces a pixel value of half the maximum).

Applying the transfer function to each spot image gives a calibrated spot image, which is integrated over area as described above to give a total energy value for the spot E_i'. The total energies in each spot derived from the film model are then compared to the known energies E_i as measured with the photodiode, and the fit error χ^2 is computed:

$$\chi^2 = \sum_i \left(\frac{E_i - E_i'}{E_i} \right)^2$$

The χ^2 value describes the goodness of the fit; lower values indicate that the model is accurately representing the film's behavior. The best model is obtained by varying the parameters p_{max}, Φ_0 and γ until the value of χ^2 is minimized. The calculation and optimization was performed in IDL, using the built-in AMOEBA function to minimize χ^2. (A more intuitive measure of the fit quality is the RMS error, which is obtained by dividing χ^2 by the number of spots and taking the square root.)

The set of best-fit parameters identified by the minimization routine should be subjected to a common-sense check to make sure they are self-consistent and physically reasonable. In particular, p_{max} should be a little less than the highest pixel values in the spot images (i.e. ~60,000), and the exponent γ should be ~1-2. It should be ensured that the optimization converges to the same parameter values from a range of starting points, that it is not driving one or more parameters up against a hard limit, and that the solution is stable to small variations in the best-fit parameters.

This process is repeated for each type of film and development process, and for each test wavelength used; in general, the set of best-fit parameters is different for different films at different photon energies. However, certain parameters should be consistent; for example, $p_{\max}$ for a given film and process should not be a function of incident wavelength. Finally, the residuals of the fit E_i'/E_i should be examined to see specifically where the model fails to reproduce the data. Agreement is most important at the low exposure values that are generally recorded during flight (even at the expense of greater errors on the longer exposures). If the residuals show any obvious systematic error, it is likely that the form of the transfer function is not flexible enough to reproduce the data, and it should be modified accordingly. The residuals also give an indication of the accuracy of the film calibration, which is a crucial component in the photometric calibration of the flight data.

**Wavelength Dependence and Accuracy of the Film Model**

The forward-fitting technique does not rely on producing a characteristic curve of density vs. fluence for a particular film and development process. However, it is useful to plot the data and results of the calibration in a form that looks like a characteristic curve. Such a plot, showing response of XUV-100 film developed in D-19 for 20 minutes vs. total energy deposited on the film in the form of 173 Å photons, is shown in Figure 32. The total energy in each exposure is shown on the x-axis. The y-axis is an artificial quantity related to the film density; for each spot, it is defined as

$$\text{Approximate Average Density } D^* = -\log_{10}\left(\frac{\text{average pixel value}}{2^{16}}\right)$$

Each digitized beam spot is plotted as a diamond; the red line shows the results of applying the best-fit film model to each spot image.

Note that the red line representing the model transfer function is not a smooth, straight curve. It is worth stressing that this plot is useful only as a rough diagnostic, and is not representative of how the data are actually analyzed. The model must look at each pixel in each spot image, and does

not simply give average density as a function of total energy. As described above, reducing the calibration data to such a curve is an unnecessary compromise and introduces considerable error into the transfer function. In particular, averaging the values of all the pixels in a spot image is not justified given the non-uniformity of the spot and the highly non-linear response of the film in the toe region.
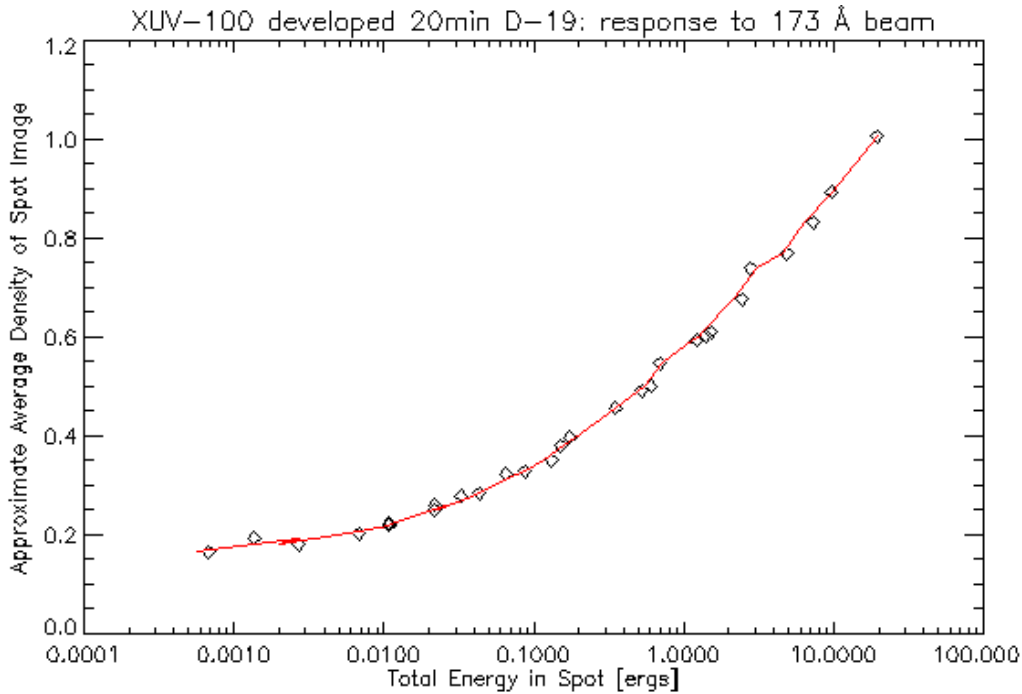
Figure 32. The calibration data for a given film type and development process can be plotted in the form of a characteristic curve. The generation of a characteristic curve is not an inherent part of the data reduction, and only approximately represents its results.

Still, plotting the data in this way does illustrate two important points. First, it is clear that we are indeed operating in the toe of the film's characteristic curve. The lowest-energy exposures are not sufficient to "turn on" the film at all, and most of the spots do not take advantage of the region of linear film response. Second, it appears that the model is doing a reasonable job of reproducing the data.
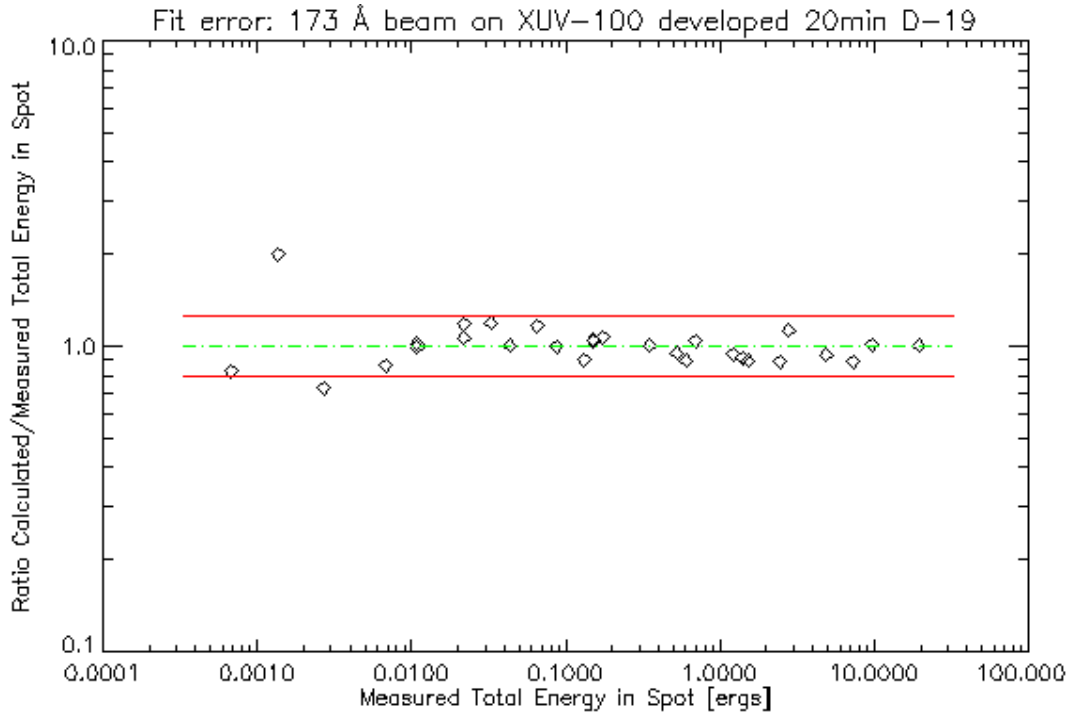
Figure 33. Ratio of total beam energy in each of the spots, calculated using the model (*Ei'*)and measured with the photodiode (*Ei*). The red lines indicate ± 20% error. Similar error plots were examined for each film type and development process studied at SSRL to ensure that the form of the film model was appropriate and to gauge the amount of scatter in the calibration data.

A better idea of the agreement between the model and the data can be obtained by plotting the residuals of the fit, E_i'/E_i vs. E_i, as shown in Figure 33. There is a slight suggestion of an inflection in the residuals around $E_i = 0.03$ ergs, which supports the finding of Kankelborg (Kankelborg 1996) that the Green and McPeters film model does not adequately capture the sharpness of the turn-on in the toe region. However, overall agreement is good, with an RMS error of 18.7% for the dataset shown. The error is worst at low exposures, where noise, in the form of cracks or opaque particle contaminants on or in the negative, is significant compared to the low-density spot image.

The model described in Equation 12 can consistently fit all the datasets with an error of less than ~25% if the fitting procedure is allowed to optimize each of the three model parameters separately for each different combination of film type, developing procedure and incident wavelength. However, so much flexibility is unphysical, and the model is successful mainly because the data is insufficient to constrain three parameters. A more useful model is obtained by

93

forcing the p_{max} parameter, which describes the base density of the film, to be a function of film type and development only.

Figure 34 shows all the datasets taken on XUV-100 film, developed for 15 minutes in a 1:9 dilution of Kodak HC-110. Each wavelength has been fit by optimizing γ and Φ_0, but all the models use the same value of p_{max}. The 173 Å and 193 Å datasets were similar enough that they could be fit with a single model. In Figure 35, the error for each of the datasets and best-fit functions is plotted. Here the suggestion that the model of Equation 12 is missing some of the details of the film response is strong: the errors show a consistent shape, and all of the models badly underestimate the fluence of the short-exposure spots. However, the general agreement shown in these figures is acceptable, at around ±20%. Better fits were obtained by using five-parameter empirical models, but the improvement was not sufficient to justify abandoning the elegance and physical basis of Equation 12.

It is encouraging that the film does not appear to distinguish between 173 Å and 193 Å photons. The wavelength dependence of the XUV-100 response seen in Figure 34 is consistent with the finding of Hoover et al. (Hoover, Walker et al. 1994) that the opacity of that film's thin gel overcoat begins to drop quickly at around 150 Å and below. The data show that the film's sensitivity continues to increase with decreasing wavelength, and is almost two orders of magnitude higher for 58 Å soft x-rays than for EUV light at 173 Å, and well into the linear regime for the short-wavelength exposures. Clearly, it will be necessary to use separate film models for each of the MSSTA bandpasses centered below 171 Å.
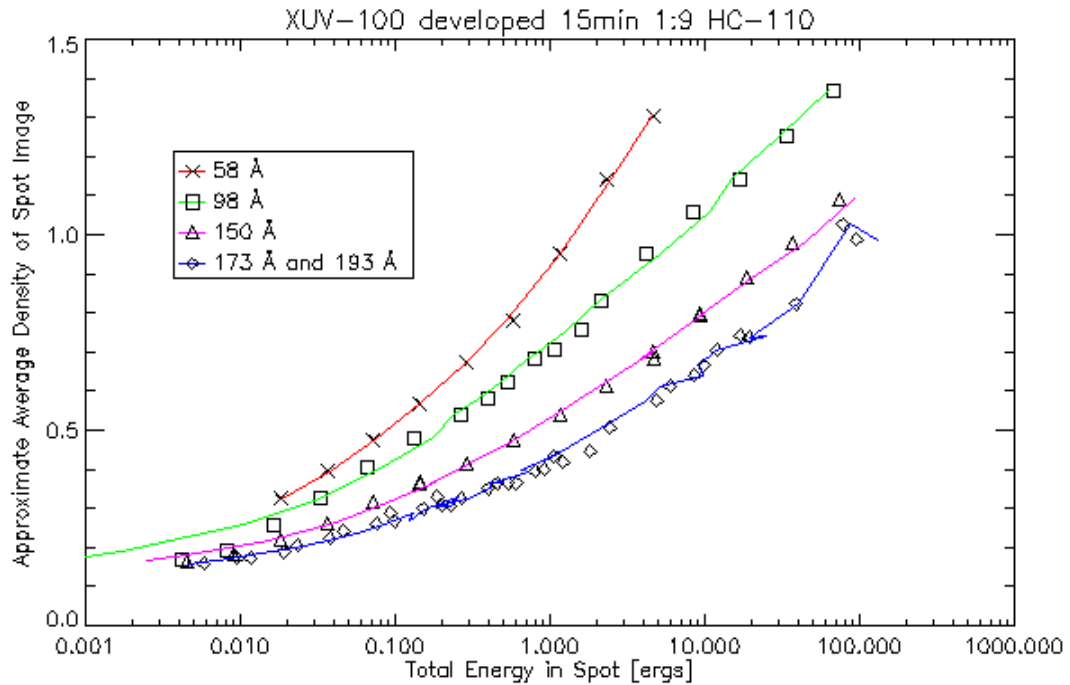
Figure 34. In general, XUV-100 film responds differently to different EUV wavelengths; here γ and E_0 have been chosen separately for each wavelength to give the best fit to the data. However, base density (p_{max}) is a function only of film type and development process, and is fixed for each dataset shown here. The 173 Å and 193 Å datasets overlie each other, and have been fit with a single model.
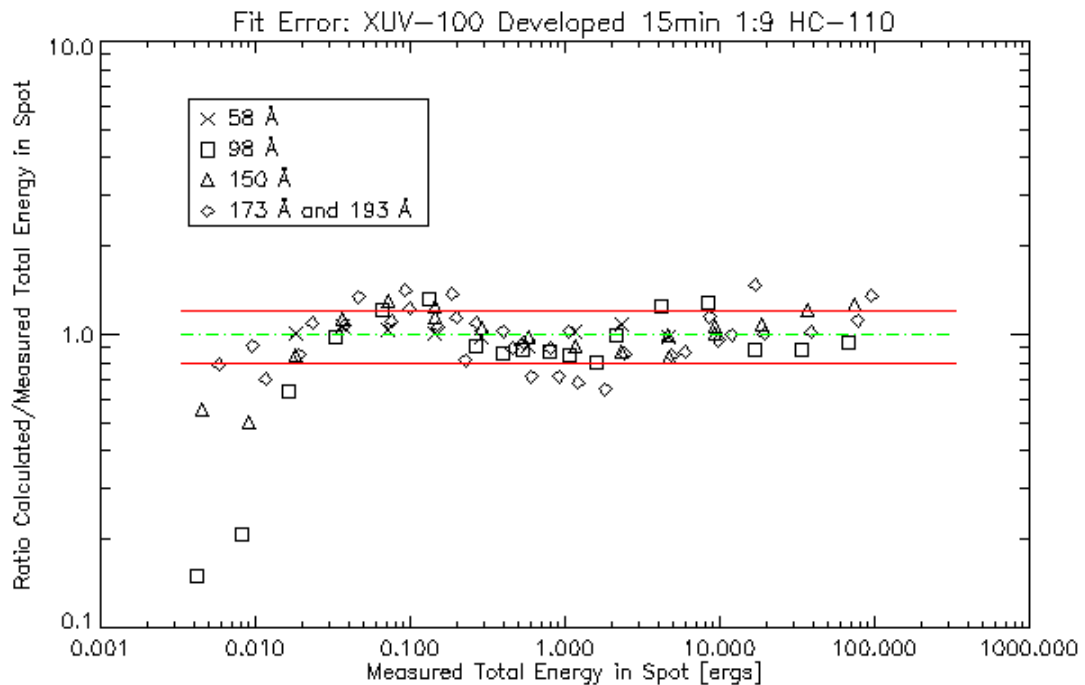

Figure 35. The discrepancy between measured energy and energy calculated from the film model for each of the spots plotted in Figure 34. There is clearly some structure in the error, indicating that the model does not capture all the subtleties of the film's behavior, particularly at low exposures.

Only a handful of other measurements were made at SSRL using XUV-100, as described in Table 10. These are shown in Figure 36 and Figure 37, with a single model being used to match both 173 Å and 211 Å. It is evident that a better fit could be obtained by modeling each wavelength separately; a model optimized for just the 173 Å data is shown in Figure 32 and Figure 33. In particular, it appears that the γ found in the combined model is too high for 173 Å and too low for 211 Å. However, the results are acceptable: the model agrees to an RMS error of ±33% over the full energy range studied, and the error is down to ±18% in the energy interval of .01 to 10 ergs, which is most relevant to the fluences delivered in flight by the MSSTA telescopes. These results confirm the idea of using a single model to describe the film's response to EUV wavelengths between 170 Å and 220 Å, but do not shed additional light on the sensitivity at shorter wavelengths.

The comparatively small amount of data collected at SSRL severely limits our knowledge of, and ability to account for, the wavelength dependence of the film's response. In addition to forcing us to use the same model for the film in different telescopes centered at different wavelengths, this limitation means we have no information about the effect of small differences in incident photon energy ($\lambda/\Delta\lambda \sim 30$), and must therefore make the assumption that the film does not substantially affect the shape of an individual telescope's bandpass. This assumption is particularly risky in the case of the 150 Å telescope, where knowledge of the bandpass is critical to our efforts to identify the source of the emission, and where the film data we do have suggests that the responsivity is undergoing a transition from one regime to another. Still, the mirror reflectivity is changing sharply enough that we will treat the film response as effectively flat over the bandpass when generating temperature kernels for each telescope.
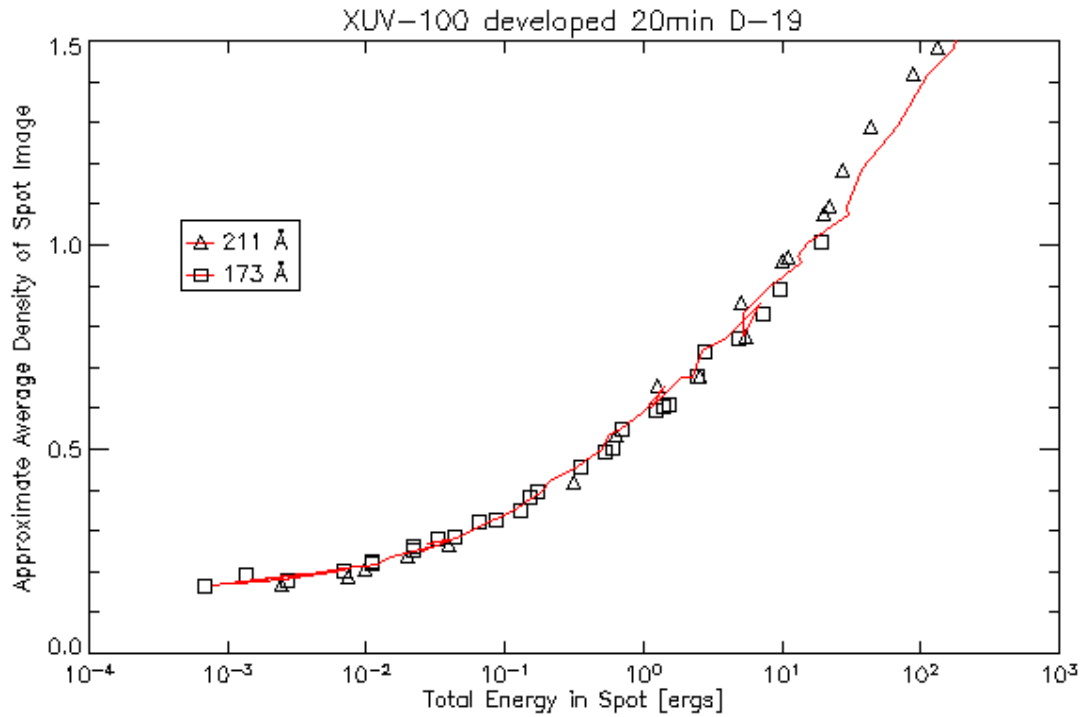
Figure 36. Only two wavelengths were used in studying the D-19 process on XUV-100. Their behavior was sufficiently similar that a single model was used to match both datasets.
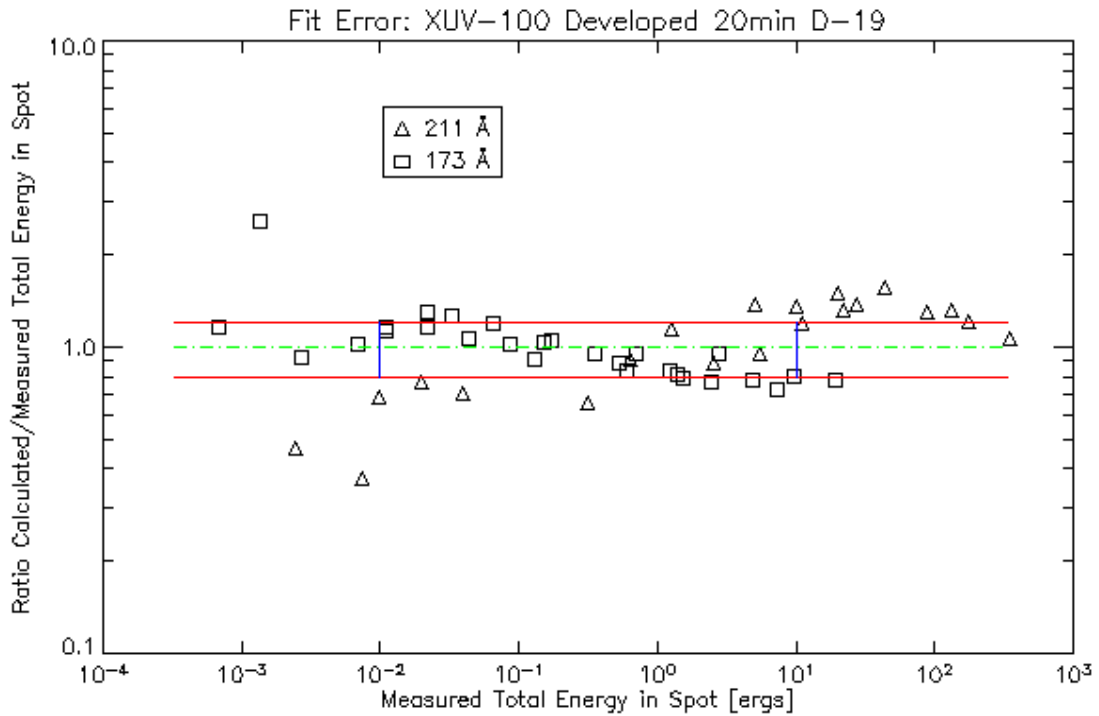

Figure 37. The model used for the two wavelengths is clearly a compromise, as the errors show an upward trend for the 211 Å and a downward trend for 173 Å. However, agreement is acceptable, particularly in the region bounded by the blue lines, which most closely reflects the exposure levels seen in flight.

The S-649 emulsion shows qualitatively different behavior when exposed at different wavelengths. The data taken on S-649 developed in D-19 are shown in Figure 38. (Note, once again, that the red curve describing the modeled energy of each spot is not smooth because the model is not a simple function of density vs. total energy, but must be applied to each pixel in each spot image.) Most of the spots represented on the plot were quite faint, and the data thus only shows the beginning of the toe of the characteristic curve. The model that is fit to all five wavelengths is therefore not terribly well constrained (except for p_{max}); however, it appears to match the data reasonably well. That it reproduces the film's behavior in the below-turn-on part of the characteristic curve is testimony to the fact that the thin, clear S-649 emulsion is much less noisy than is the crack-prone XUV-100.

Figure 39 reveals little wavelength dependence, with the exception of 193 Å, which appears to be following a much lower-γ curve than the model dictates once the exposure is sufficient to move it out of the toe regime. The data on 173 Å and 150 Å are insufficient to support any conclusions about whether the S-649's response changes at around 150 Å, as the XUV-100 appears to; however, it does appear that it responds equally well to 58 Å and 98 Å light. This may indicate that the small grains of S-649 are fully activated by individual photons at either of these wavelengths. Other data taken on S-649 using different developing processes lead to similar conclusions (and similar ambiguity about the film's response in the linear regime).

The model shown in Figure 39 agrees to ±20% or better with the data at each wavelength except 193 Å, where the agreement is only ±38% RMS. While it appears that the data are beginning to diverge from the model at higher fluence values, agreement in the range of total exposure anticipated during flight is generally good.
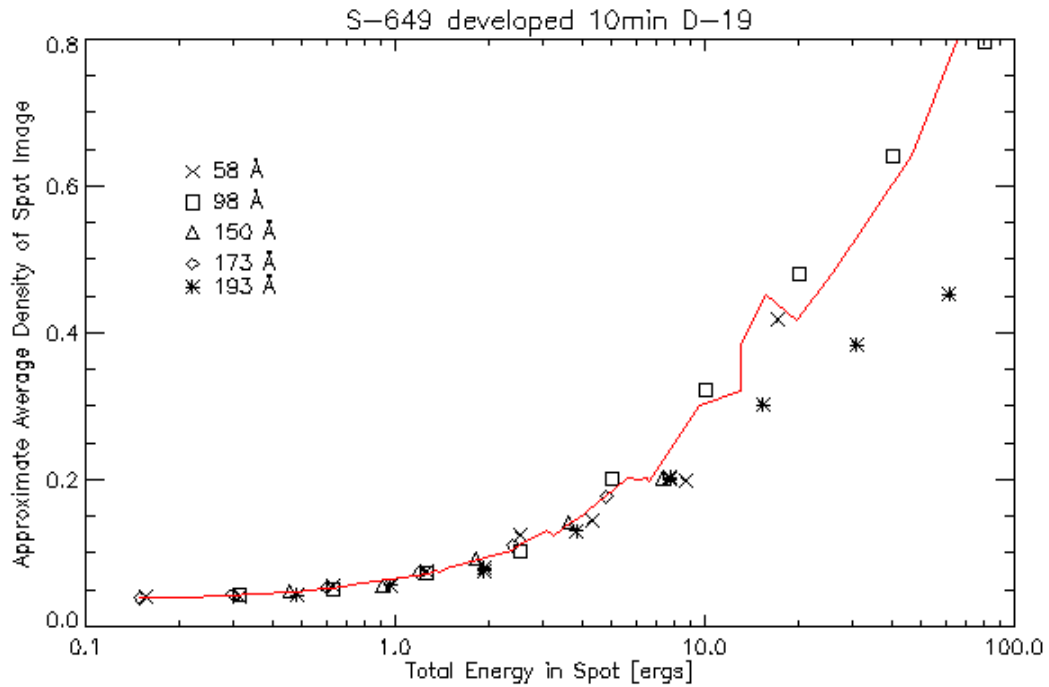
Figure 38. Five wavelengths exposed on S-649 film and fit with a single model. The EUV flux of the synchrotron beam was barely enough to get the film to respond, and most of the data is taken at energies below the point where the film response becomes linear. There is little evidence of wavelength dependence, except in the longer exposures on 193 Å.
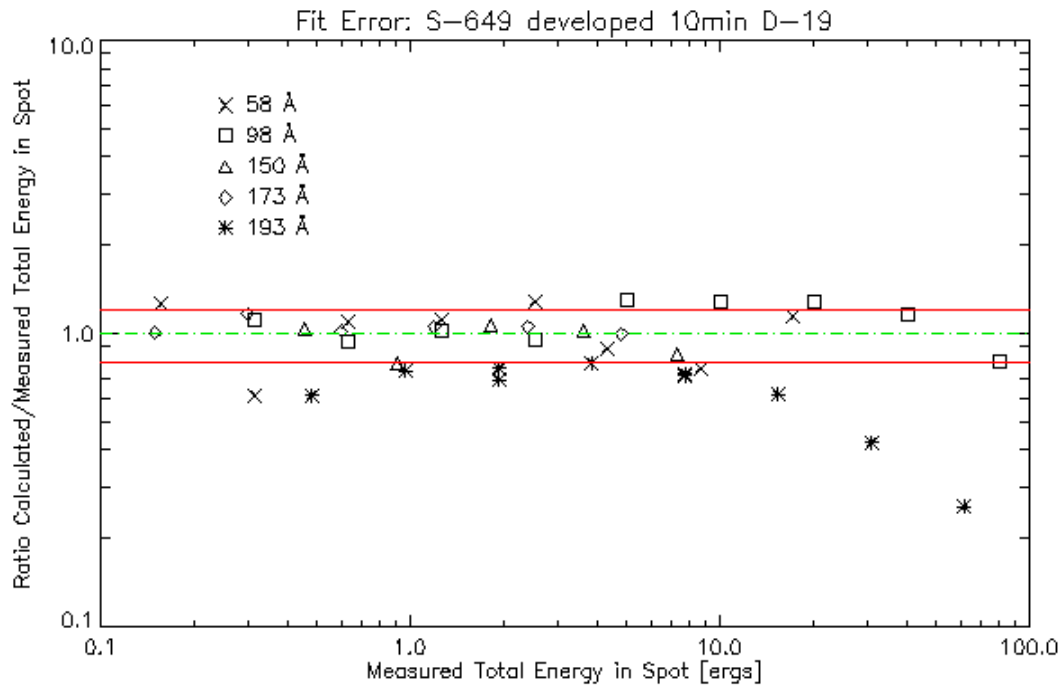
Figure 39. The model gives an RMS error <20% for all wavelengths other than 193 Å. Because the S-649 film is relatively resistant to cracking, signal-to-noise at low exposure values is better than what is seen with the XUV-100. The data appears to be diverging from the model in the long exposures.

In summary, applying the model transfer function of Equation 12 to the calibration film through the forward-fitting approach described above generally resulted in estimates of the total energy deposited on the film that were accurate to ±20%. This figure is not out of line with the target for photometric calibration accuracy of the MSSTA mission (which was ±25%), and is roughly comparable to the accuracy achieved in other phases of the calibration effort. However, a few caveats must be emphasized before accepting that the EUV flight film calibration is accurate to 20%:

- The accuracy of the transfer function has only been evaluated at relatively large spatial scales. The film spots that serve as data points in the plots above occupy as much space on the film as a 3 arc minute section of sun at the focal plane of the large Ritchey-Chrétien MSSTA telescopes. Measuring fluence at smaller spatial scales will result in considerably more scatter, and the calibration is almost completely unreliable at the scale of the film grain (where counting statistics dominate the transfer function).

- There appears to be a break in the characteristic curve of the XUV-100 that is not reproduced by the best-fit transfer function, indicating that the model is not capturing all the physics of the film's response. In general, the model works best over the middle of the fluence range expected from flight; at the higher and lower ends, it is less accurate.

- The data are insufficient to fully characterize the wavelength dependence of the film's response. On the XUV-100, we will use a single model to characterize the film's response to 171 Å, 180 Å, 195 Å and 211 Å; each of the shorter wavelengths will be fit separately. On the S-649, a single model must be used for all wavelengths. For both films, we will have to assume that the film response is essentially flat over the wavelength range of any given telescope's bandpass.

Selection of Film for Flight

With the above cautions in mind, we can use the optimized film models to examine each of the film types and processes studied at SSRL, and select the best combination for use with the flight EUV telescopes. The flight film will be required to provide high signal-to-noise ratio, a large dynamic range, and excellent spatial resolution at the wavelengths and flux levels expected during flight. Thus, the first step in selecting the best film and developer is to anticipate the flux levels each of the MSSTA telescopes will deliver at the film plane.

Doing so requires estimating the intensity of solar radiation over the telescope's bandpass, and folding that through the response of the telescope's mirrors and filters. The product of the predicted solar spectrum with the effective area function of each telescope is integrated over wavelength (and multiplied by the square of the telescope's focal length fl to convert steradians of emitting solar material to cm^2 on the film), giving expected flux at the film plane:

$$\phi = fl^2 \int I(\lambda) A_{Eff}(\lambda) \mathrm{d}\lambda \qquad \text{[ergs cm}^{-2}\text{ s}^{-1}\text{]}$$

For a given exposure time Δt, this results in a predicted fluence of

(Equation 13) $$\Phi = \int \phi \mathrm{d}t \approx \phi \cdot \Delta t \qquad \text{[ergs cm}^{-2}\text{]}$$

which can be compared with the film calibration results to determine how much contrast will be produced in each film type under consideration.

The effective area function for each telescope is determined by the geometry of the optical system and the results of the mirror and filter calibration:

(Equation 14) $$A_{Eff}(\lambda) = A_{Geom} \varepsilon_f(\lambda) \varepsilon_m^n(\lambda) \qquad \text{[cm}^2\text{]}$$

where ε_f is the transmission efficiency of the filter, ε_m is the reflection efficiency of the mirror, n is either 1 (for the single-reflection Herschelian telescopes) or 2 (for the double-reflection Ritchey-Chrétien telescopes), and A_{Geom} is the geometrical collecting area of the telescope,

$$A_{Geom} = \pi(d^2 - o^2) - A_{Spider}. \qquad \text{[cm}^2\text{]}$$

Here d is the aperture of the telescope and o is the diameter of the central obstruction; the effective area of the Ritchey-Chrétien telescopes is further reduced by the spider vanes.

The predicted intensity of the solar spectrum,

$$I(\lambda) \qquad\qquad [\text{ergs cm}^{-2} \text{ sterrad}^{-1} \text{ s}^{-1} \text{ Å}^{-1}]$$

is more difficult to calculate and less reliable. A synthetic spectrum can be generated by using the CHIANTI database and associated IDL routines (Dere, Landi et al. 1997). This process is described in more detail in section 1.3.2; it requires an input differential emission measure function DEM(T) that describes the thermodynamic state of the plasma. In order to examine the full range of intensities the MSSTA could hope to image, synthetic spectra were generated using the previously-measured DEMs of an active region and a coronal hole. The reliability of such calculations in this highly dynamic spectral regime has not been extensively tested; even using the best databases, a theoretical spectrum rests on so many assumptions that it should not be trusted to reproduce the actual solar output over an EUV bandpass with accuracy better than about a factor of 4.

Table 11 shows the predicted fluence on a part of the film imaging an active region and a coronal hole for each of the MSSTA III EUV telescopes. The full dynamic range of the payload is a daunting 5 orders of magnitude, which few films can handle without saturation or underexposure. However, it is clear that, at a minimum, the film should be able to produce a usable density above the base fog at an incident fluence of 0.1 ergs cm^{-2}, and that it not saturate at $\Phi = 100$ ergs cm^{-2}. Most of the images will be taken around the lower end of this fluence range; unfortunately, it is the minimum-fluence criterion that proves much harder to satisfy.

| Central λ	Predicted Solar Flux in Bandpass ($\lambda \pm 10$Å) [ergs cm-2 s-1 sr-1]		A_{Geom} [cm2]	Peak ε_m	Peak ε_f	Focal Length [cm]	Predicted Fluence on Film in 30-sec Exposure [ergs cm-2]	
[Å]	Active Region	Coronal Hole		[%]	[%]		Active Region	Coronal Hole
58	7514	15	314	9	19	150	1.21	0.002
98	1898	15	314	36.1	29.3	150	9.56	0.145
131	828	21	507	60.4	29.6	100	86.50	2.748
150	1620	15	412	46.5	28	350	1.92	0.021
171	20942	498	98	47.7	43.9	200	71.90	2.263
180	27190	492	98	46.1	43.9	200	48.53	0.369
195	31528	104	412	37.3	40.4	350	51.58	0.124
211	21816	46	412	32.9	33.8	350	18.63	0.034
256	11400	51	412	20.4	18.7	350	0.50	0.003

Table 11. Predicted fluence values for the MSSTA telescopes based on measurements of the instrument bandpasses and synthetic spectra calculated with CHIANTI. These predictions served as guidelines in the choice of film and development process. The 256 Å telescope was not added to the payload until after the film calibration experiments were performed.

The best-fit calibration models for each film and process (Equation 12) can be inverted to give the film's response (approximate average density, D^*) as a function of predicted incident fluence. Checking where the predicted fluences of Table 11 fall on the resulting curve is an easy way to estimate the suitability of a film process for observations with a given telescope. Figure 40 shows the inverted models for the XUV-100 calibration. The black curves show the film's response to EUV wavelengths in the 171-211 Å range with two tested development processes; the solid curve for D-19 demonstrates a notably higher sensitivity than is achieved with the HC-110. The solid black curve is linear through most of the fluence range expected from active regions. The green curves illustrate the effect of different wavelengths on the film's response; again, wavelength dependence was not measured on film developed with the D-19 process, but the data in HC-110 suggest that the film grows substantially more responsive at wavelengths of ~150 Å and below. All of the curves show that the film is essentially unresponsive to the very lowest coronal hole fluences anticipated from flight.

The situation is even worse when we examine the results of the S-649 calibration, shown in Figure 41. None of the development processes tested can make that film respond to the fluence levels delivered at coronal hole portions of the MSSTA telescopes' film planes. The S-649 is only suitable for observing the strongest active regions, and even in those cases it is generally not in the linear part of its characteristic curve. Of course, it has one advantage over XUV-100 that is not reflected in Figure 41: its base is much less noisy. Therefore, even though it produces little density in response to very low fluences, the signal-to-noise ratio it produces in its toe region is much better than what XUV-100 delivers. Still, the fact that it does not even begin to respond until the fluence reaches a few ergs cm^{-2} precludes its use with the MSSTA III EUV telescopes.
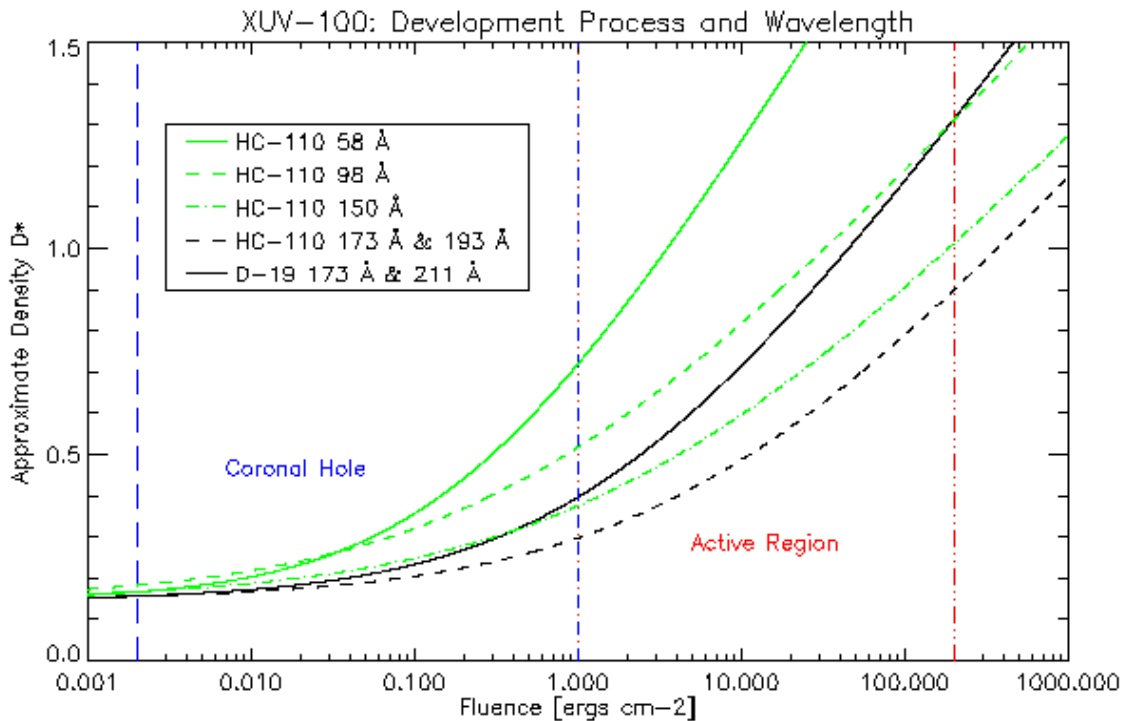
Figure 40. Inverted film models for the calibration of XUV-100. Developing with D-19 results in an enhanced response at wavelengths around 173 Å. Also, it is clear that the film's sensitivity improves at wavelengths below ~150 Å, although the wavelength effect was only measured on film developed in HC-110.
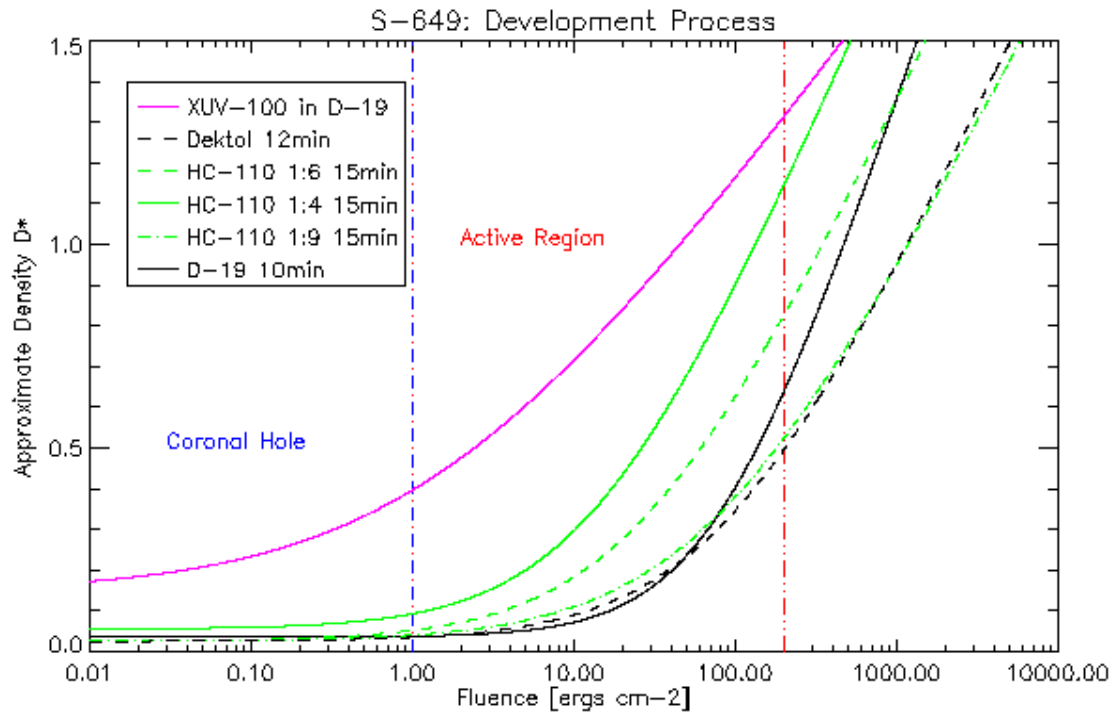
Figure 41. While its sensitivity is noticeably improved by using a concentrated developer, S-649 film (black and green curves) is substantially less responsive than XUV-100 (purple), regardless of the development process, and is unsuitable as a detector for the MSSTA III EUV telescopes. Note that whatever wavelength dependence the 649 film may possess is ignored by these models.

These results agree qualitatively with the observations of past MSSTA missions using XUV-100 and S-649. The S-649 film barely produces a noticeable amount of density when used in fast telescopes centered on strong, active-region lines. The XUV-100 images generally show a widespread (though noisy) low-density response in coronal holes, and strong, almost linear response to bright solar features.

Film in the FUV Telescopes

As described in Section 2.5.2, we were unable to perform any film calibration measurements at FUV wavelengths. Furthermore, the interaction of the various components of a photographic emulsion with FUV radiation is likely to be different enough from their interaction with either visible light or EUV that we cannot draw any quantitative conclusions about the films' FUV

response from our knowledge of their behavior in other regimes. Therefore, the FUV images are essentially uncalibrated.

Given this limitation, we decided to use S-649 film in the two FUV telescopes, centered at 1216 Å Lyman α and 1550 Å C IV. Its superior spatial resolution and noise characteristics, compared to XUV-100, are highly desirable, and, while we lacked detailed knowledge of its response characteristics, past MSSTA missions had proven that S-649 was sufficiently sensitive to record an image from the FUV Ritchey-Chrétien telescopes.

Conclusions

Because we were determined not to splice different films for use in the MSSTA III cameras, we concluded that only XUV-100 offered the necessary sensitivity at the lower end of the expected range of fluences to be produced by the MSSTA telescopes. Therefore, XUV-100 film was chosen as the optimum detector for all of the EUV instruments.

Abandoning the use of S-649 was a difficult decision, as it is in many ways a superior emulsion to XUV-100. Its stated resolution is ten times better, and our experience suggests that the advantage may be even more significant. It is also much less susceptible to cracking, and thus offers a better signal-to-noise ratio in those regimes where the incident fluence is sufficient to activate the film.

An attempt was made to improve the sensitivity of S-649 film by hypersensitization. The film was placed in a vacuum chamber, which was then backfilled with forming gas at a 3 p.s.i. gauge pressure and left for 24 hours. In principle, this process removes moisture from the emulsion and can render it orders of magnitude more sensitive, particularly in low-flux, long-duration exposures (Smith, Schrader et al. 1971). Identical set of exposures were taken on hypered and unhypered film, and developed in an identical process using 1:9 strength HC-110 developer. The results are shown in Figure 42. The hypered film does show a slightly higher density at all energies, but it is not clear that it is any more sensitive than the unhypered S-649; more likely, it is just slightly fogged. The turn-on point in the curve occurs at roughly the same energy. The

uninspiring results, and the difficulty and inconsistency of the hypersensitization process, convinced us to abandon this effort.
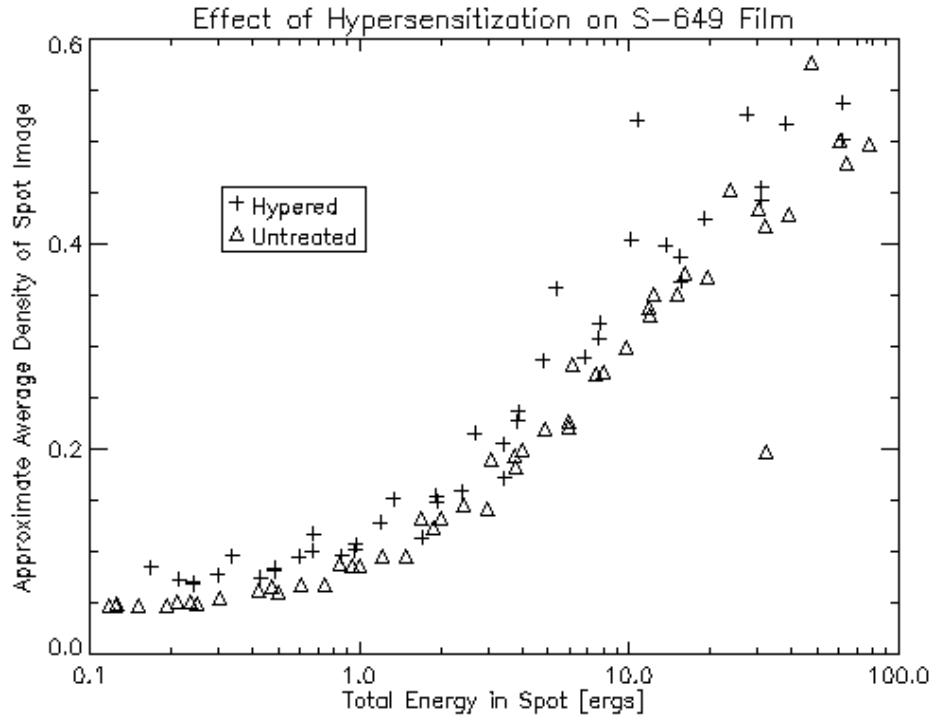
Figure 42. Gas hypersensitization of S-649 film produced a slight overall fogging of the film, with no noticeable change in its sensitivity.

Settling on XUV-100 also meant ignoring the bulk of the calibration data taken at SSRL, since we collected far more data on the response of S-649 than we did on the XUV-100. As a result, only two development processes were tested for XUV-100, and only one of these was examined over a the full range of the payload's wavelengths. However, what data we did gather (Figure 40) suggest that D-19 results in much better sensitivity than HC-110. It has also been used on previous MSSTA flight data, and is therefore more of a known quantity. Thus, D-19 was chosen as the developer for the flight film.

Finally, while the study of the effect of different development processes and wavelengths on EUV-sensitive emulsions is unlikely to be of interest, as film is no longer widely used for astronomical research, a brief examination of our SSRL data allows us to draw some preliminary conclusions about S-649 that bear reporting:

- Its response in the EUV turns on sharply and becomes essentially linear at fluences greater than about 10 ergs cm^{-2};

- In the EUV regime, it does not seem to differentiate based on the exact wavelength of the incident light;

- Using a concentrated developer can significantly enhance its sensitivity (at the expense of some unquantified loss of spatial resolution, though not nearly enough to make it comparable to XUV-100 in that regard);

- Changing development time has a slight effect on the film's responsivity; however, the degradation of spatial resolution as development time is lengthened can be large;

- In contrast to the findings of Hoover *et al.* (Hoover, Walker et al. 1994), Kodak Dektol developer does not produce much better sensitivity in S-649 than D-19 or HC-110 under similar temperature and development-time conditions.

As mentioned above, the one EUV telescope that did not employ XUV-100 was the 256 Å Ritchey-Chrétien, which used commercially-available Technical Pan film. This telescope was a last-minute addition to the payload, settled on after the film calibration experiments had been performed. Because it used a spare thin-foil filter which had not been optimized for 256 Å, its throughput was so low that we considered it marginal for obtaining high-quality data even with XUV-100. While we had very limited data on Tech Pan's EUV performance, it has been used for space-based coronal imaging in the past (Spiller, Barbee et al. 1994). We did not believe that using Tech Pan instead of XUV-100 would improve the quality of the 256 Å images, but felt that using it on this one telescope represented a low-risk, high-reward experiment.

2.5.4 APPLYING FILM CALIBRATION TO FLIGHT DATA

The decision to use XUV-100 and D-19 developer for all of the EUV telescopes meant that we were without calibration data for most of the wavelengths studied by the MSSTA payload. Furthermore, we did not have sufficient data to determine the ideal processing conditions given the choice of chemistry. The only D-19 process we tested called for 20 minutes in the developer at 21° C. This is a rather extreme push process; standard T-Max 100 film is rarely developed for

more than 2-3 minutes. While we do not have reliable data to support this conclusion, there are hints in the literature [(Mouchel 1966), (Dancy and Buckley 1987)] and in our SSRL results that lengthening the development time eventually reaches a point of diminishing returns in terms of contrast enhancement; however, the granularity continues to increase as the film is developed. We decided that cutting the development time for the flight film in half was unlikely to reduce the film's sensitivity by an unacceptable amount, and might offer a small but precious improvement in spatial resolution. Therefore, the flight film was developed in D-19 for 10 minutes.

We originally planned to return to SSRL after the flight in order to calibrate this new process at all of the relevant wavelengths. Unfortunately, the extremely limited supply of XUV-100, and the impossibility of obtaining new emulsion, along with the difficulty of working with the cameras on a UHV beamline, rendered further film calibration experiments impossible. Rather than deriving a new film model for the process used on the flight film, we were forced to use the film model fit to the data taken at SSRL at 173 Å and 211 Å on XUV-100 developed in D-19 for 20 minutes, and introduce a series of ad hoc corrections to account for the discrepancies between the flight and the calibration measurements.

Developing Time Correction

The calibration film was developed for 20 minutes, flight film for only 10 minutes. In order to make this correction, we took two identical sets of visible-light exposures at a range of incident fluences, developing one set in D-19 for 10 minutes and the other for 20 minutes. In order to conserve flight film, we used commercial T-Max 100 film for this cross-calibration experiment. The two sets of developed negatives were scanned, and compared on a pixel-to-pixel basis. A fourth-order polynomial function of the form

(Equation 15)
$$\log_{10}(p_2') = \sum_{i=0}^{4} a_i \left(\log_{10}(p_1)\right)^i$$

was fit to the data, with the parameters a_i chosen to minimize the differences between p_2, the pixel values on the negatives developed for 20 minutes, and p_2', the pixel values obtained by applying the transfer function to the raw pixel values in the corresponding part of the negative

developed for 10 minutes (p_1). The converted pixel values p_2' are then entered into the film model to produce a calibrated image.

This step is, of course, a less-than-ideal addition to the calibration process. The transfer function is purely empirical, and allows some scatter into the results. Furthermore, while the properties of T-Max 100 and XUV-100 are quite similar, the fact that we used something other than the flight film, and performed the experiment at visible, rather than EUV, wavelengths, means that the transfer function parameters may not even be the best for correcting the flight data. Nevertheless, the results, shown in Figure 43, indicate that the error introduced by this correction is manageable – the scatter is 20.2%. Much of this can be attributed to alignment errors between the 10-minute and 20-minute exposures; these negatives lacked details that could be used for co-registration, and point-to-point fluctuations in the opacity of the step wedge which was used for this experiment can therefore masquerade as errors in the development time conversion. At worst, half of the error (~10%) seen in Figure 43 is intrinsic to the conversion itself.
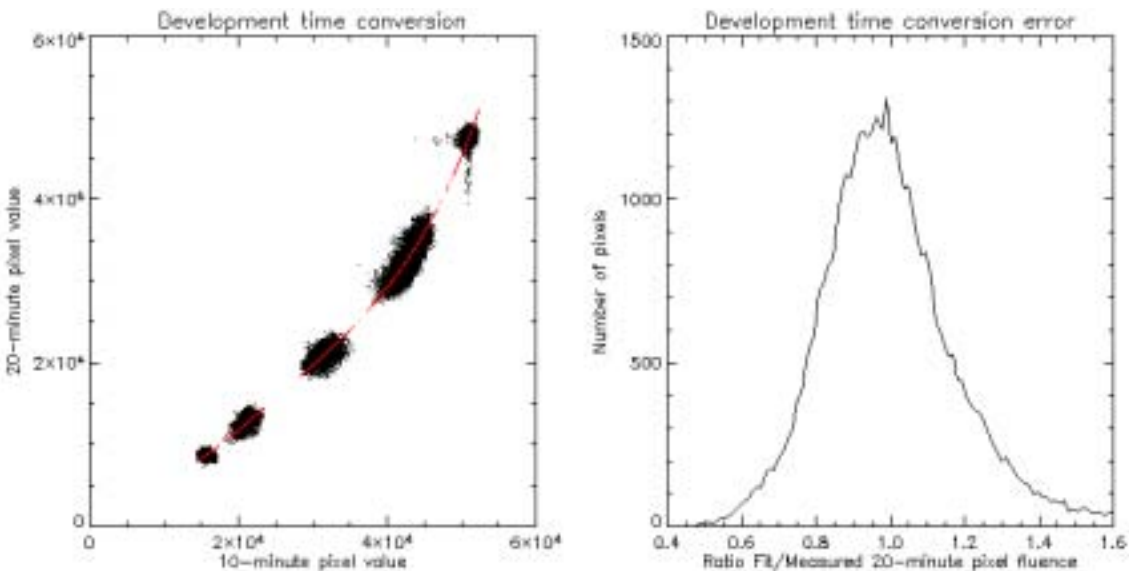
Figure 43. Calibration film was developed for 20 minutes, flight film for only 10 minutes; therefore, before the calibration can be applied, the flight film pixel values are modified to account for this discrepancy. A polynomial transfer function was optimized by comparing a density step strip, developed for 10 and 20 minutes (left). This correction results in an RMS error of about 20% in the extracted fluence values (right). Most of the scatter in these figures is due to imperfect alignment of the step wedge images used in the experiment.

Wavelength Correction

The parameters of the film model were optimized by examining the data taken at 173 Å and 211 Å. They are applicable for the MSSTA telescopes centered at 211 Å, 195 Å, 180 Å and 171 Å; however, our SSRL results indicate that the film response changes significantly at shorter wavelengths. This point was rendered largely moot by the failure of the 58 Å, 98 Å and 131 Å telescopes; however, for the 150 Å telescope, a further correction is applied.
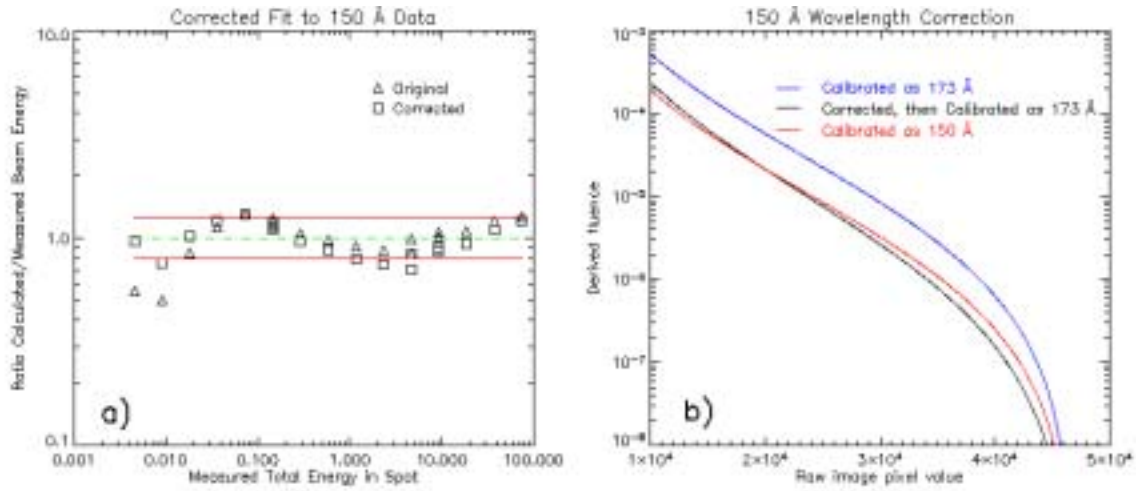
Figure 44. Because the D-19 process used in flight was not tested at different wavelengths, the film's increased response to 150 Å light was accounted for by applying a polynomial correction function to the pixel values in the 150 Å images before applying the film calibration. This additional step actually appears to improve the fit between the film model and the calibration data, as shown in a). In b), the shape of the correction function is shown for comparison with the direct calibration of 150 Å data.

The wavelength correction function is very similar in form to the development time correction (Equation 15); however, the polynomial is only third order, i.e.

(Equation 16)
$$\log_{10}(p_{173}') = \sum_{i=0}^{3} b_i \left(\log_{10}(p_{150})\right)^i$$

The parameters b_i were optimized by analyzing the calibration data taken at 150 Å and developed in HC-110 (shown in Figure 34). The pixel values from these spot images p_{150} were converted to the pixel values expected from the same fluence of 173 Å light using the polynomial above, and the resulting "effective 173 Å" pixel values p_{173}' were then converted to fluences (via the film

model, Equation 12) using the film calibration parameters derived from those 173 Å – 211 Å exposures that were developed in the same HC-110 process.

It is assumed that applying the same pixel transformation function to the 150 Å flight data, which was developed in D-19, and then using the film model derived from 173 Å calibration data developed in D-19, will result in correct fluence values. This technique necessarily reduces our confidence in the accuracy of the calibration of the 150 Å data. It requires that we assume that the wavelength response of the emulsion is independent of the developing process used, and thereby opens the door to unquantified systematic errors. However, as Figure 44a demonstrates, the extra step actually gives a slightly better fit to the 150 Å calibration data than simply applying the best film model directly. Thus, to the extent that we can estimate the error, there is no loss of accuracy from the correction.

Scanner Correction

A similar pixel-to-pixel transform allows us to account for the different scanners used on the flight negatives. Most of the images used in the analysis to follow, and all of the calibration data, were digitized on a Umax PowerLook III scanner. The linearity and repeatability of this scanner with flight film was extensively tested. However, it only offers a spatial resolution of ~1200 dpi; in order to take full advantage of the MSSTA telescopes' resolution, we had to use an Imacon Flextight Photo scanner, with a resolution of ~3200 dpi. The Imacon scanner introduced a number of large-scale spatial distortions into the data, so its scans were not used for most analysis. However, in those cases where digitizations with the Imacon scanner were used, the images must be processed by first applying a function of the form

$$p_u{}'(p_i) = j \times p_i{}^k + l$$

to convert the pixel values p_i reported by the Imacon scanner to pixel values comparable to those produced by the Umax scanner under a similar fluence p_u. The parameters j, k and l of this empirical correction function were determined by scanning the same set of flight film with each scanner. The Imacon scan was downsampled to match the lower-resolution Umax scan, and the two were compared pixel by pixel.

As noted in section 2.5.3, different scanners measure density differently, and thus a function mapping pixel values measured with one scanner to pixel values of the other can only ever be an approximation. The scatter in the pixel-to-pixel conversion suggests that images digitized with the Imacon scanner have an additional calibration uncertainty of ~10%. The error is undoubtedly higher when these images are not downsampled, so quantitative work with full-resolution Imacon scans must be approached with caution.

2.5.5 CONCLUSION

The goal of the film calibration effort was threefold: we wished to identify the best film and developing process for use in flight; we needed to characterize this process so that flight data could be reduced to physical units; and we needed to understand the error associated with the calibration process. Based on the results obtained at SSRL, we selected XUV-100, developed in D-19 for 10 minutes, for the EUV telescopes. While we did not test this combination at EUV wavelengths, we developed a two-step method to convert scanned negatives processed in this way to physical units, and can use our calibration experiments to estimate the accuracy of this conversion.

Final Calibration Function

Film calibration takes the form of a function $\Phi(p)$ that converts the pixel values p from a digitized flight negative to fluence delivered to that portion of the film. For flight data digitized with a Umax scanner, the calibration function is

(Equation 17)
$$\Phi(p) = \Phi_0 \left(\frac{p_{\max}}{10^{\sum_{i=0}^{4} a_i (\log_{10} p)^i}} - 1 \right)^{\gamma} \qquad [\text{ergs cm}^{-2}]$$

The parameters

$$\Phi_0 = 7.0 \times 10^{-6} \text{ ergs cm}^{-2}$$

$$p_{\text{max}} = 46932$$

$$\gamma = 1.85$$

were found by forward fitting to the synchrotron calibration data taken on XUV-100 and developed in D-19. The parameters

$$a_0 = 4274.1392$$

$$a_1 = -3897.6880$$

$$a_2 = 1333.0171$$

$$a_3 = -202.50629$$

$$a_4 = 11.533777$$

were found by comparing two sets of T-Max 100 negatives processed for 10 minutes and 20 minutes in D-19. In general, Φ_0 and γ are functions of wavelength; however, it was found that the values listed above provided acceptable agreement at EUV wavelengths between 171 and 211 Å. For the 150 Å images, the pixel values are subjected to a preliminary wavelength correction (Equation 16), with parameters
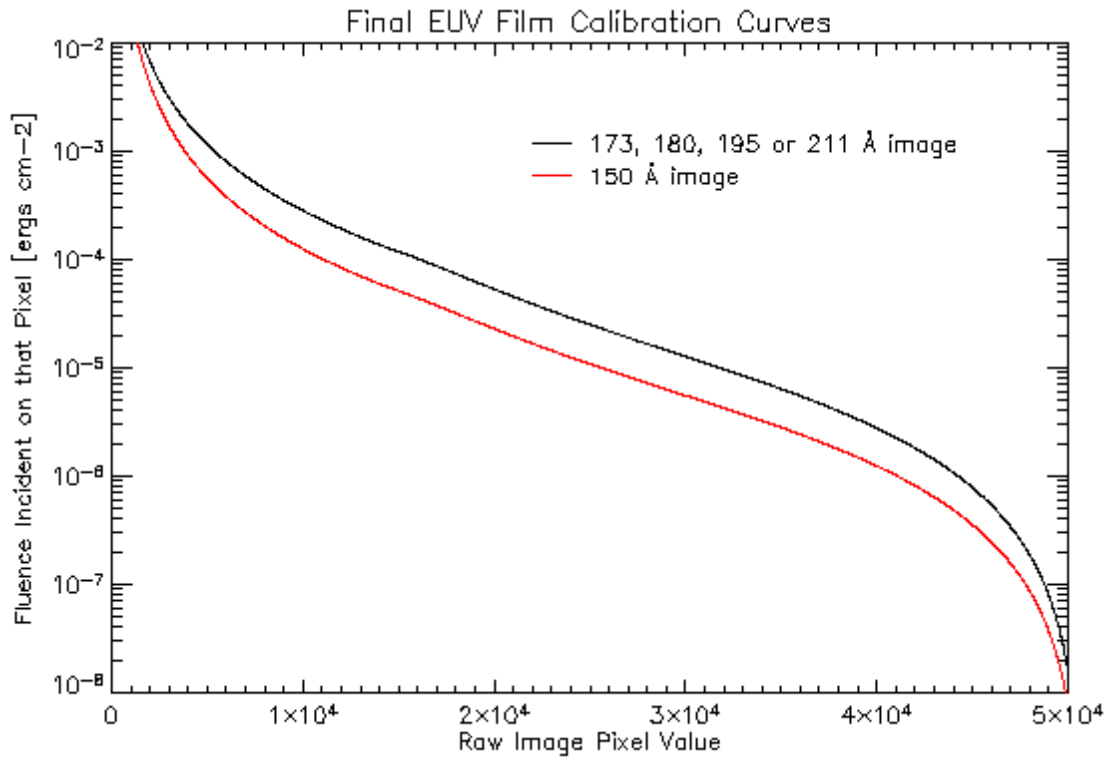
$$b_0 = -1.24427$$

$$b_1 = 1.59039$$

$$b_2 = -0.00853001$$

$$b_3 = -0.0130251$$

determined by analysis of synchrotron calibration data taken on XUV-100 and developed in HC-110. The calibration functions for 150 Å and other EUV wavelengths are plotted in Figure 45.

Figure 45. Complete pixel-to-fluence curves used to calibrate the MSSTA III EUV images. For most images, the active region pixel values lie in the linear part of the film's response (~25,000 – 40,000), while the quiet region pixels fall near the toe of the curve (~40,000 – 50,000).

Calibration Error

The film model (the parameters Φ_0, p_{max} and γ) reproduced the results of our synchrotron experiments with an accuracy of better than 20% RMS at all wavelengths. Correcting the film model for the development time discrepancy (with the parameters a_i) adds an additional (uncorrelated) error, whose magnitude we conservatively estimate at 10%. Thus, the measured uncertainty of fluence values obtained with the above function is ~22%.

However, estimating the accuracy of the calibration function when it is applied to flight film is complicated by a number of discrepancies between flight data and calibration measurements. Correcting for these discrepancies requires that we make certain assumptions about the film's behavior, specifically:

115

- That the effect of cutting the development time from 20 minutes to 10 minutes is the same for XUV-100 and for T-Max 100, and independent of exposure wavelength, since visible light T-Max was used to tune the development-time correction parameters;

- That the wavelength dependence of the emulsion's response is independent of the development process used, since the 150 Å to 173 Å correction was tuned using a different development process than what was used on the calibration and flight film;

- That the batch of XUV-100 emulsion's response characteristics did not change significantly between when the film was calibrated (March 2000) and the time of flight (April 2002);

- That the secondary conditions of the development process, such as chemical temperature, agitation, rinse water hardness, etc. were similar enough on flight film and calibration film that repeatability of the process was not affected.

Quantifying the uncertainty associated with these assumptions would have required an extensive, impractical effort. Therefore, we will proceed as though all of these assumptions are valid, though with the understanding that the unknown systematic errors on our data could be significant.

2.6 Summary

As noted in Section 1.3.3, the calibration of a narrowband EUV telescope does not result in a simple function converting data numbers to physical units of interest, such as coronal temperature. Calibration must proceed in two directions: the film/scanner assembly is measured to allow conversion from arbitrary pixel values to fluence at the focal plane, and the instrument is measured at its operating wavelength to produce a bandpass (effective area as a function of wavelength). In order to obtain a DEM or similar description of the state of the coronal plasma, the bandpass must be used to construct a temperature kernel.

In this section, I will present the temperature kernels generated from the MSSTA bandpass measurements described above. I will then discuss the errors in these temperature kernels, and in the film/scanner calibration. (The implications of these errors for our ability accurately diagnose the state of the corona are presented in Chapter 4).

For the FUV telescopes, the situation is slightly different. First, from a theoretical standpoint, the assumptions that underlie the construction of temperature kernels and DEMs are not generally valid. Furthermore, the calibration of our FUV instruments (and of the film at FUV wavelengths) is far less exhaustive than for our EUV telescopes. I will end this section with a discussion the utility and limitations of our 1216 Å and 1550 Å observations.

2.6.1 TEMPERATURE KERNELS

The process of generating temperature kernels from an EUV instrument bandpass is described in Section 1.3.3. It starts with the instrument bandpass, in the form of an effective area curve $A_{eff}(\lambda)$ based on measurements of the mirror and filter efficiency (see Equation 14). Figure 46 shows the effective area of the 9 MSSTA III EUV telescopes plotted over a model solar active region spectrum. Clearly, the large Herschelian telescope at 131 Å benefits from high-efficiency

multilayers, well-optimized filters and an unobstructed single-reflection system; it is four times more efficient at collecting photons in its bandpass than any of the large Ritchey-Chrétien telescopes. Also, note that the 256 Å Ritchey-Chrétien has an extremely small effective area, primarily due to absorption by the Zr in its visible light-suppression filter. (As described in section 2.3, the filters were designed to reject 304 Å light, and were not optimized for wavelengths longer than ~220 Å). In general, the more efficient telescopes (which also generally used faster focal ratios) were matched to the weaker lines.
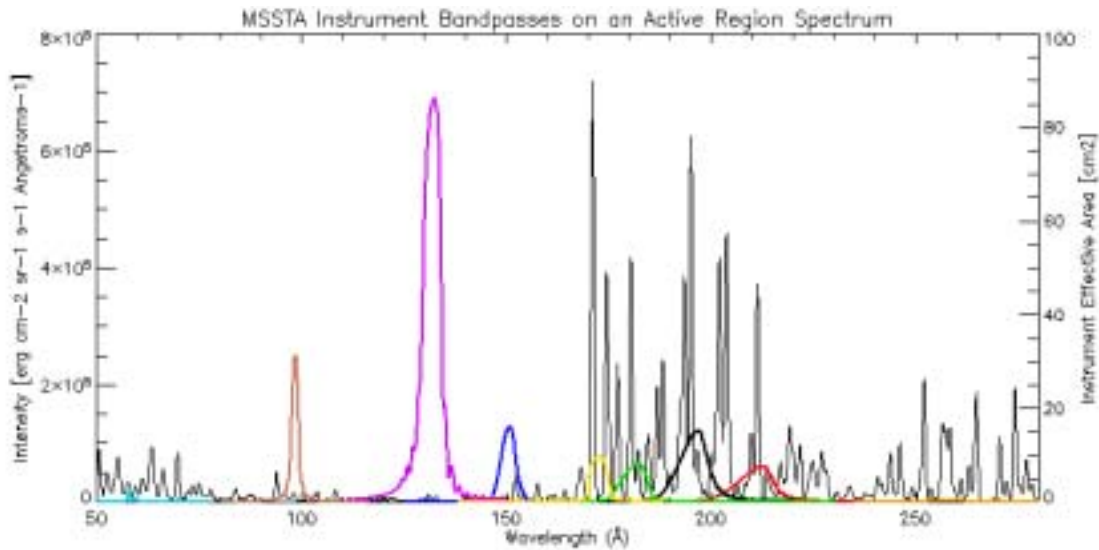
Figure 46. Effective area of the MSSTA III telescopes over a solar active region spectrum.

I then used CHIANTI to generate a list of emission lines from 40 – 300 Å. The contribution function G(T) of each line was calculated using the following assumptions:

- Constant pressure P = 1.0×10^{15} [K/n$_e$];

- Elemental abundances as specified by CHIANTI's "extended coronal abundances," which relies on the measurements of [(Feldman, Mandelbaum et al. 1992), (Landi, Feldman et al. 2002), (Grevesse and Sauval 1998)];

- Ionization equilibrium states of the elements as specified by CHIANTI's "Arnaud-Raymond_ext", which uses measurements from [(Arnaud and Rothenflug 1985), (Arnaud and Raymond 1992), (Landini and Fossi 1991)];

118

Then each instrument's temperature kernel was generated by summing all the contribution functions, weighted by the effective area of the telescope at the central wavelength of the emission line. Finally, the temperature kernel was divided by the square of the telescope's focal length:

$$K_i(T) = \sum_j G_j(T) \frac{A_{eff}^i(\lambda_j)}{fl_i^2} \qquad [\text{ergs cm}^{-2}\ \text{s}^{-1}\ \text{DEM}^{-1}]$$

Note once again that the units of the temperature kernel are the same as those of the line contribution functions; the telescope simply merges a number of lines, and measures the total flux at its focal plane rather than at its aperture.
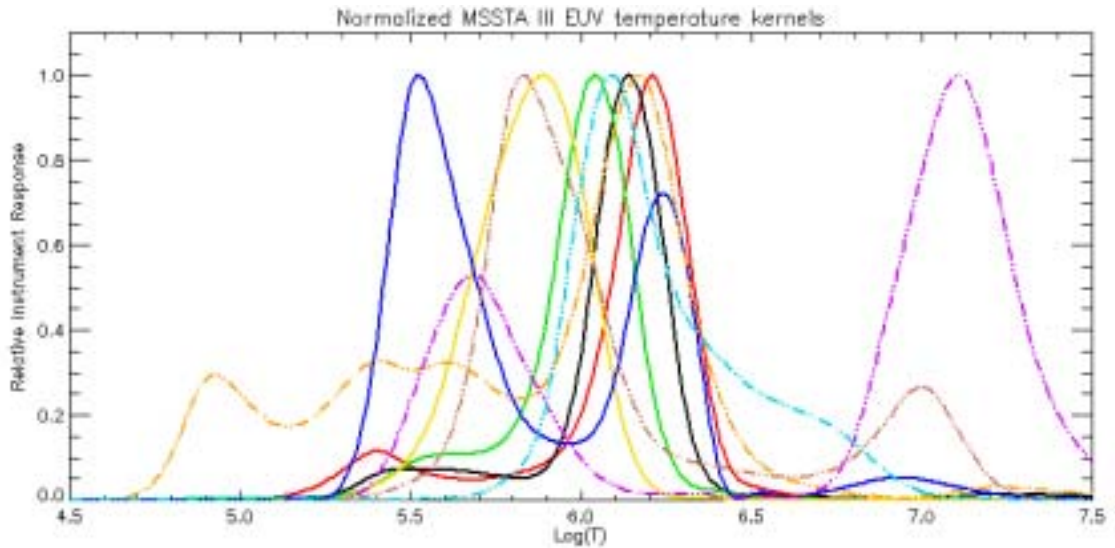
Figure 47. Normalized temperature kernels of the MSSTA III telescopes. The color assignments are those used in Figure 6.

The temperature kernels of the MSSTA III EUV telescopes are plotted in Figure 47. Note that, qualitatively, these are very similar to the predictions of Figure 6, illustrating the insensitivity of the general shape of the temperature kernel to the more subtle aspects of the bandpass curve. As long as the peak of the bandpass falls on the wavelength of a strong line, the telescope's temperature kernel will resemble that of the central line. The contributions from off-peak lines (which are weaker in intensity and less efficiently collected by the bandpass) are generally ten or more times smaller than those of the central line. Such contributions are hard to notice on a linear scale, but, because the DEM varies by orders of magnitude over the temperature range plotted,

they can become significant. Furthermore, it is necessary to look at the absolute (non-normalized) temperature kernels when doing any sort of quantitative analysis. Therefore, the most useful representation of the MSSTA III temperature kernels is that shown in Figure 48.
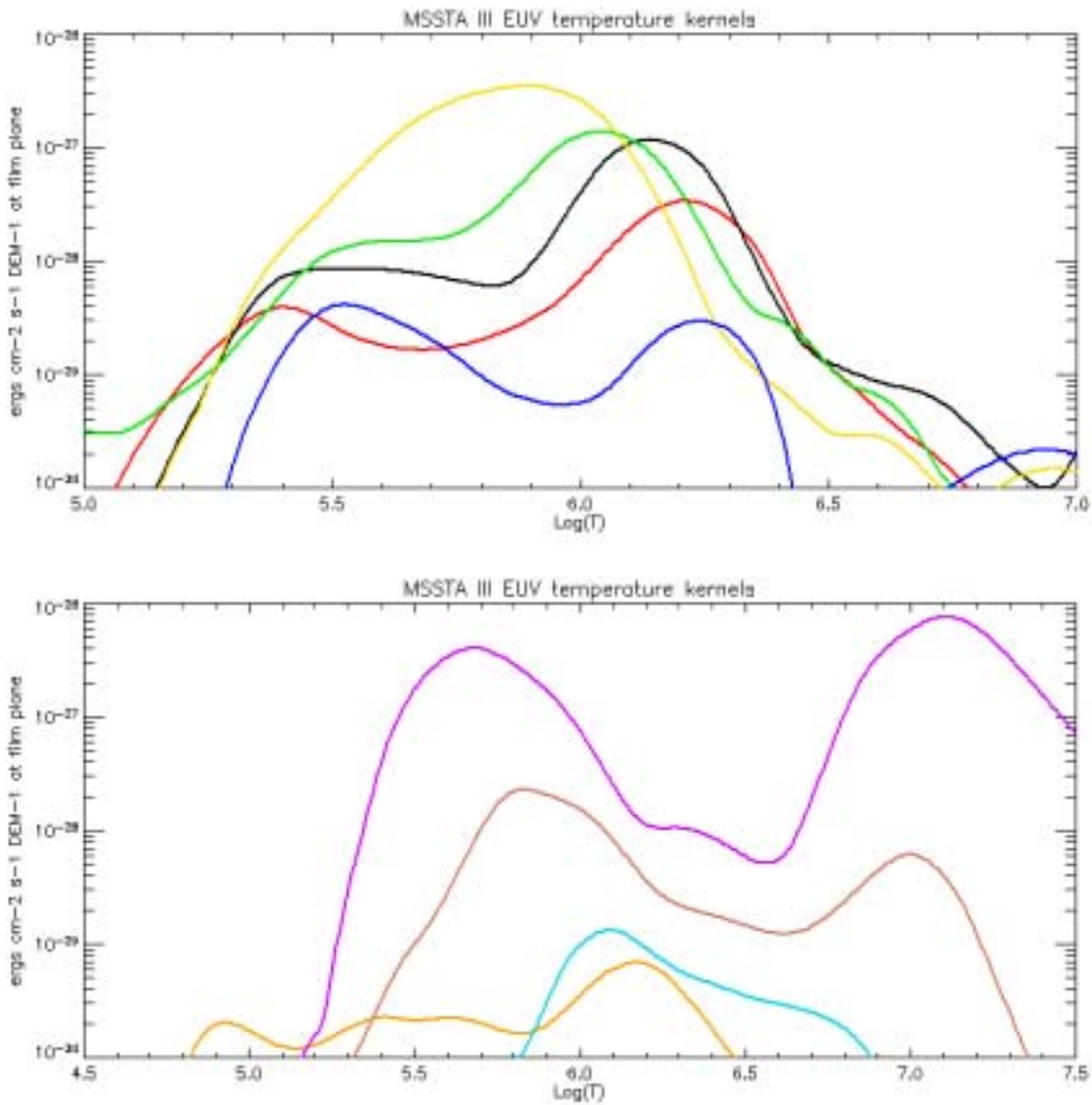
Figure 48. Absolute temperature kernels for the MSSTA III EUV telescopes. On top are the kernels for the 5 telescopes that successfully recorded images; below are the kernels of the four failed telescopes.

120

2.6.2 ERROR

There are substantial uncertainties in both the temperature kernel matrix $K_i(T)$ – a result of errors in mirror and filter bandpasses, as well as the errors and assumptions inherent in the atomic physics used to define the temperature response of a bandpass – and in the calibrated data (g_i) – arising from uncertain film calibration and, to a much lesser extent, photon statistics. Both contribute to error in the DEM derived from MSSTA observations. However, characterizing the errors in $K_i(T)$ and g_i is more than just a matter of putting limits on the reliability of the results of any analysis. The procedures described in section 4.1 for extracting a DEM are highly sensitive to noise, and require accurate characterization of the error associated with the inputs in order to guarantee that they work stably and produce sensible outputs. Therefore, it is essential that we have a clear understanding of what those errors are.

Effect of error on Temperature Kernels

Mapping the error bars on an instrument's bandpass to error bars on its temperature kernel is not a straightforward process. Errors that are essentially independent of wavelength – such as uncertainty in the filter transmission – are simply handled by assigning the same error to every point in the temperature kernel ($\Delta A_{eff}/A_{eff} = \Delta K/K$). However, the error bars on the mirror reflectivity measurements indicate uncertainty about the wavelength at which the efficiency peaks. The temperature kernel of a bandpass centered at, say, 150 Å looks quite different from one centered at 152 Å (cool O VI lines dominate in the first case, hot Ni XII/XIII lines in the second), and there is no easy way to decide which to use in the case of the MSSTA III EUV telescope, or even to draw meaningful error bars on the temperature kernel that is ultimately chosen.

Part of the problem lies in interpreting the error associated with the mirror calibration. Most of the uncertainty in the shape of the multilayer bandpasses comes from point-to-point variation of the bandpass over the surface of the large Ritchey-Chrétien primary mirrors. It is not clear that treating such measurements as repeat measurements (with individual errors) of a single quantity

121

is valid. If, as seems likely, each sample adequately represents the performance of some region of the mirror's surface, rather than each representing a random sample of a bandpass that varies constantly over the mirror, then the average of the samples is the true bandpass, and the error is actually fairly small. Furthermore, the secondary mirrors were generally not measured for the large Ritchey-Chrétien telescopes; because of their relatively small surface area, they are unlikely to show a similar variation.

We chose to model the effect of multilayer bandpass error on each instrument's temperature kernel in the following way: first, a range of different bandpasses, each fitting within the composite bandpass error bars, was generated. The temperature kernel of each possible bandpass was generated, and all these temperature kernels were compared to each other qualitatively. In every case except those of the 150 Å and 256 Å Ritchey-Chrétiens, the possible temperature kernels were all quite similar in shape. Either the shape of the bandpass was known well, with only overall magnitude errors expected (as was the case with the 131 Å and 58 Å telescopes), or the solar spectrum in the region was fairly clean and no strong contaminating lines were allowed in even as the bandpass was shifted (as with the 195 Å and 211 Å bandpasses), or both. They can be adequately modeled by treating the bandpass errors as though they were wavelength-independent.

The 150 Å and 256 Å kernels varied so widely when their bandpasses were moved around within the error bars that it is pointless to specify the error on their temperature kernels. It is necessary either to accept that the average bandpass captures the multilayer's point-to-point variation and represents the true performance of these instruments; or to decide that they are not useful for a temperature kernel analysis. Any results obtained from their images should be viewed with caution, and cross-checked if possible.

In those cases where the bandpass error can be treated as wavelength-independent, the error in the resulting temperature kernel is given by

$$\varepsilon_K = \sqrt{(n \times \varepsilon_m)^2 + (\varepsilon_f)^2 + (\varepsilon_t)^2}$$

where ε_m is the uncertainty in the mirror reflectivity at the center of the bandpass (taken from Table 3), n is the number of reflections, ε_f is the filter transmission uncertainty (set at 10%, per

section 2.3.5), and ε_t is the uncertainty associated with the theoretical parameters that go into the CHIANTI database, conservatively set at 10% based on the work (Judge, Hubeny et al. 1997). The resulting errors are listed in Table 12.

Central Wavelength [Angstroms]	% Error in Temperature Kernel	Effective % Error in Observation
58	15.0	26.6
98	14.3	26.2
131	14.1	26.2
150	20.5**	30.1
171	14.2	26.2
180	14.1	26.2
195	25.3	33.5
211	24.8	33.2
256	42.8**	48.1

Table 12. Error on the temperature kernels of the MSSTA III EUV telescopes. The 150 Å and 256 Å temperature kernels are highly suspect, as both are very sensitive to the shape of the bandpass and uncertainties in the mirror calibration are substantial. See the text, as well as the cautions on Table 3.

Absolute flux error

In all but two cases (the 150 Å and 256 Å telescopes), we have concluded that it is sufficient to treat the error on the temperature kernels as a single number, assignable to the overall normalization of the kernel. This error is indistinguishable from the error on the observations Δg_i. The observation error itself is almost entirely due to the uncertain film calibration, shown in section 2.5.5 to be 22%, after appropriate caveats are considered. Therefore, analysis of the MSSTA data can be dramatically simplified by combining all the errors into a single estimate for each telescope, pretending that the kernels are known with absolute certainty and that the only significant error is a composite Δg_i. These results are shown in the final column of Table 12. The following additional considerations, some of which have been previously raised, must be kept in mind:

- The shape of the multilayer bandpasses: Some of the telescopes were not measured enough times to identify point-to-point variations. Where such variations were found, they were

treated as scattered measurements of a single quantity, which may not be valid. Secondary mirrors were not measured, but should demonstrate less variation than primaries. The errors associated with the atomic physics should affect the shape of the bandpass, but are here treated as normalization errors. Similarly, relatively large uncertainty in the wings of the multilayer bandpasses has been ignored.

- Transmission of the filters: The filters were not measured experimentally. Transmission uncertainty was estimated conservatively at 10% based on previous work.

- Film calibration: A number of ad hoc fixes were applied to the film calibration, resting on some untested assumptions. These are listed in section 2.5.5.

- Atmospheric absorption: discussed in more detail in Section 3.3.1. Atmospheric absorption is substantial; the model used to correct for it contains some uncertainties, which can be compensated for but not entirely eliminated.

In summary, the MSSTA III EUV observations are calibrated to ~25-35%.

2.6.3 FUV TELESCOPES

Figure 26 shows the effective area of the two FUV telescopes on the MSSTA III. As described in section 0, these measurements are fairly accurate, although a large uncertainty exists around the stability of the mirror coating. However, our inability to calibrate the S-649 film at FUV wavelengths means that extracting absolute fluence measurements from their images will require that we cross-calibrate the telescopes with other, well-characterized instruments. Furthermore, at FUV wavelengths, good knowledge of the bandpass does not allow the creation of a temperature kernel. It does give us an opportunity to model the output of the FUV telescopes, and thereby determine how to analyze their images. If the images are found to be formed primarily by radiation from a single emission line, they can be cross-calibrated by normalizing the total flux in each image to spectral measurements.

We wish to characterize the response of these instruments to the typical FUV output of the solar atmosphere, in much the same way that Handy et al. characterized the TRACE 1216 Å and 1550 Å bandpasses [(Handy, Bruner et al. 1998), (Handy, Tarbell et al. 1999)]. To do so, we use a

synthetic full-disk solar FUV spectrum (based on the measurements of [(Rottman, Woods et al. 1993), (Curdt, Brekke et al. 2001)] and fold it through the bandpasses shown in Figure 26. The results are shown in Figure 49, which gives expected average flux at the film plane as a function of wavelength.

FUV Telescope Response
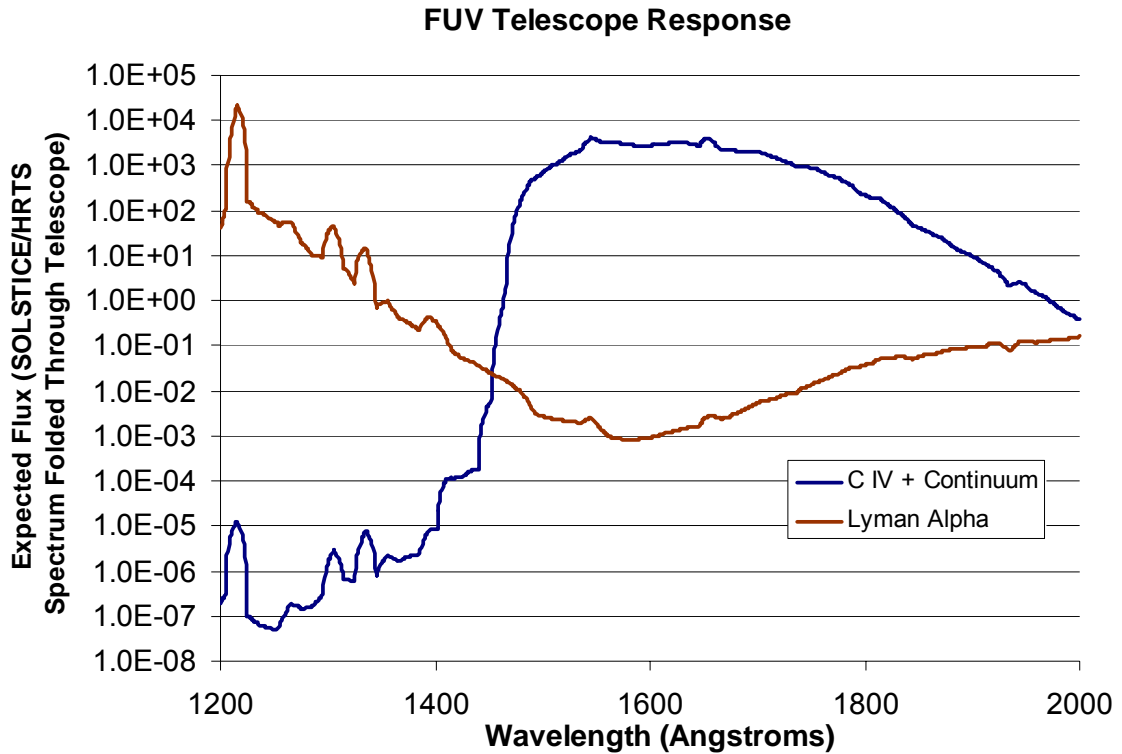
Figure 49. Response of the MSSTA III FUV telescopes showing the spectrum of expected flux at the film plane. The 1216 Å telescope shows a strong peak for Lyman α; in the 1550 Å telescope, the emission lines of C IV are barely visible above the FUV continuum.

The running integrals of the film-plane flux shown in Figure 50 show conclusively that the MSSTA III Lyman α telescope is quite pure spectrally. While these results are based on a full-disk-averaged SOLSTICE spectrum, and thus may be misleading when examining Lyman α-dark cell centers, it is clear that the MSSTA 1216 Å images can be interpreted as essentially uncontaminated maps of Lyman α emission. Contrast this with the running integral shown in (Handy, Tarbell et al. 1999), which indicates strong contamination by FUV continuum in TRACE's 1216 Å images. Their spectral purity makes an approximate cross-calibration of the MSSTA 1216 Å images simple to perform. The full-disk flux of the image can be normalized using the Lyman α line flux measured by SOLSTICE on the day of the MSSTA's flight. This

procedure requires some knowledge of the effect of atmospheric absorption on the MSSTA's throughput, and is discussed further in section 3.3.2.

FUV Telescopes Contribution
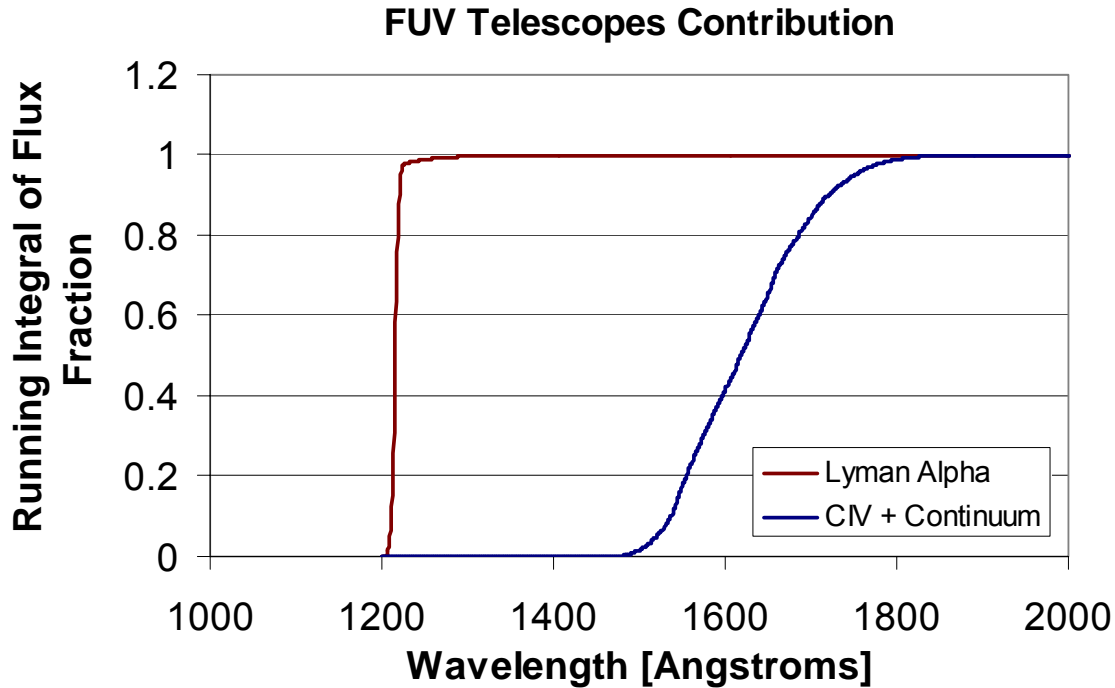
Figure 50. Running integral of the expected flux at the film plane shows that the 1216 Å telescope is completely dominated by Lyman α flux, while the 1550 Å telescope sees emission from a broad range of wavelengths from 1500-1700 Å.

On the other hand, the MSSTA's 1550 Å image is almost entirely FUV continuum, with only a barely-noticeable contribution from the strong C IV and Si II emission lines. Whereas TRACE can increase the contrast between C IV and continuum radiation by subtracting a continuum-only image, our 1550 bandpass is essentially uncalibratable (even cross-calibrating with TRACE's continuum images is unfeasible, as the two instruments have substantially different bandpasses and thus see different chunks of the continuum). Its images are extremely sharp (approximately 1 arc-second resolution), and thus may be useful for studying the morphology of the chromospheric network; but absolute flux measurements cannot be obtained or interpreted for this telescope.